Development of a Propulsion Rotor Performance Model for Ultra-Low Reynolds Number Flow ($Re < 10^5$)

Thesis

Presented in Partial Fulfillment of the Requirements for Graduation with Honors Research Distinction in the College of Engineering of The Ohio State University

By

Isaac Solomon Bensignor

Undergraduate Program in Aerospace Engineering

The Ohio State University

2021

Honors Undergraduate Research Thesis Committee:

Dr. James W. Gregory, Advisor

Dr. Brian Ritchie

Abstract

A Martian exploration vehicle capable of sustained flight could explore and gather data about large areas of interest from an aerial perspective. NASA has recognized this advantage and has sent Ingenuity — the first helicopter to ever fly in another planet's atmosphere – to Mars, which arrived in February 2021 and is scheduled to fly for the first time in April 2021. The next logical step in progression of vehicle development and testing would be to design and test a fixed-winged drone for Mars exploration. Proving a fixed-winged vehicle could sustain prolonged flight on Mars opens the door to many new avenues of atmospheric planetary exploration. However, flying in the Martian atmosphere – let alone anywhere outside of Earth – has never been attempted before.

Fundamental aerodynamic principles related to flight and performance must be reevaluated for Mars atmospheric conditions that have nearly 167x less pressure than Earth's atmospheric pressure at sea level. Reynolds number (Re) – an important aerodynamic characteristic indicative of the nature of the flow field structure and pattern – is the primary metric being examined in this project's analysis for its relationship and effect on propulsion rotor and flight performance. Existing literature has explored the possibility and development of such a propulsion technology, however, no existing public literature has used NASA Ames "Rotor Optimization for the Advancement of Mars

eXploration" (ROAMX) team's most recent ultra-low Reynolds number optimized rotor geometry.

A Blade Element Momentum Theory analysis code in MATLAB was developed and was verified for its efficacy and accuracy using a reputable external source. For the same rotor geometry and operation conditions, nearly the same outputs were produced compared to the external source's BEMT model. For the five plots used for comparison of model accuracy, the absolute average percent error difference was less than 7.77% at the worst, and 2.11% at best for the data compared.

A computational fluid dynamics analysis was performed with ANSYS Fluent on the 7% span location of a ROAMX rotor geometry for discerning 2D blade geometry performance metrics at a Re = 15,000 and Mach number = 0.22. The 7% span location produced relatively low performance coefficients. This was expected, as the 7% span location was optimized for structural rigidity and not aerodynamic performance. The maximum lift to drag ratio was 7.5 at four degrees blade pitch; the maximum lift coefficient was 0.038; and the airfoil appeared to reach the stall condition at eight degrees. Analysis of the 25, 50 and 75-100% blade geometries is expected to yield higher airfoil performance.

Dedication

To Richard Bensignor, Robin Sultan, Elina Bensignor,

and Danielle Bensignor

Acknowledgments

Dr. James Gregory and Dr. Matthew McCrink have my sincerest gratitude and appreciation for providing me guidance, mentorship, and support throughout this research project. Dr. Gregory's AERO 2200 introductory aerospace engineering class truly made me passionate for this field of study. His methodical and insightful teaching skills; his aptitude for educating; and the care he demonstrated for his students truly shed a bright light on how exemplary of a professor and engineer he is – the Mechanical and Aerospace Engineering Department is lucky to have such a qualified and kind person be serving as their Chair. Dr. McCrink is owed just as much of a "thank you" – I have learned troves of aerospace related knowledge, methodologies, and insight from him related to computational fluid dynamics, drone flight operation, research, modeling, and testing. I cannot express my appreciation enough for the care and patience both Dr. Gregory and Dr. McCrink have expressed while supporting my research interests and educational aspirations.

Additionally, a thank you is extended to Dr. Brian Ritchie for agreeing to serve on this URT's Defense Committee.

Moreover, I would like to thank Achal Singhal and Wenbo Zhu for their help troubleshooting some of the technical, analytical, and coding issues that arose through

this project. I appreciated their kindness, time, and willingness to help when I was in need.

I next owe a debt of gratitude to my family – Dad, Mom, Elina, and Danielle – for their love, support, and motivation for so many years. They have encouraged and pushed me to work towards aspirations and goals I didn't think I could reach. I could not ask for a more endearing and supporting network of people to cheer me on.

My experience as an undergraduate student at The Ohio State University has led me to meet many commendable, laudable, and meritorious educators and faculty members. The roles Dr. John Horack, Dr. Jen-Ping Chen, Dr. Ken Gordon and Dr. Mrinal Kumar were influential in my undergraduate experience, and I owe them a debt of gratitude for demonstrating and exemplifying the role of an ideal educator/faculty member.

I would also like to thank my internship mentors from NASA and the Air Force Research Laboratory for the skills cultivated and knowledge learned from each experience. Mr. Paul Bielski of NASA Johnson Space Center and 1st. Lt. Andrew J. Vogel of AFRL spent countless hours patiently helping me, teaching me, and letting me struggle when they knew I could solve the problem at hand with some intuition and out-of-the-box thinking. Thank you for being model mentors.

I owe a thank you to Mr. Witold Koning of the NASA Ames Aeromechanics Branch ROAMX team for dedicating many hours of his time to me discussing the current status of the ultra-low Reynolds, high Mach number flow domain with respect to rotor and airfoil performance.

Lastly, I owe a thank you to Jonathan Richmond. By random chance we sat down next to each other on the first day of AERO 2200 recitation and became lab partners. That small encounter led to a years-long friendship and pillar of support while making our way through the Aerospace Engineering curriculum. We spent countless late nights, long assignments, and attempts at understanding frustrating concepts together. Thank you for being a great friend and engineer.

Vita

June, 17, 2017	High School Graduation; Williston Park, NY, USA
June – August, 2019	Intern, Engineering Directorate, Simulations and Graphics Branch; NASA Johnson Space Center, Houston, Texas, USA
August - December 2019	Undergraduate Teaching Assistant, Department of Mechanical and Aerospace Engineering, The Ohio State University; Columbus, Ohio, USA
June – August 2020	Intern, Space Vehicles Directorate, Space Vehicles Research Branch; Air Force Research Laboratory, Kirtland Air Force Base, Albuquerque, New Mexico, USA

Field of Study

Major Field: Aerospace Engineering, Bachelor of Science

Table of Contents

List of Tables

List of Figures

Nomenclature, Acronyms, and Abbreviations

Symbol	Definition (and units when applicable)
ρ	Fluid density, $\frac{kg}{m^3}$
μ	Fluid viscosity, $\frac{N*s}{m^2}$
V, U, U_P, U_T, v_i	Velocity, $\frac{m}{s}$
Re	Reynolds Number, unitless
l	Length, meters
M	Mach Number, unitless
γ	Ratio of Specific Heats, unitless
R	Gas Constant, $\frac{J}{Kg*K}$; Radius, meters
T	Temperature, Kelvin; Thrust, Newtons
C_l	Coefficient of Lift, unitless
C_{l_α}	Lift Curve Slope, $\frac{1}{radians}$
C_d	Coefficient of Drag, unitless
C_{d_0}	Profile Coefficient of Drag, unitless
A	Area, m^2
w	Vena Contracta velocity, $\frac{m}{s}$
r_∞	Vena Contracta position, m

σ	Blade solidity, unitless
N_b	Number of blades comprising the rotor disk
c	Chord length, meters
$\dot{m}$	Mass flow rate, $\frac{kg}{s}$
Ω	Rotational rate, $\frac{rad}{s}$, RPM
C_p	Coefficient of Pressure, unitless; Coefficient of Power, unitless
C_{p_0}	Profile Coefficient of Power, unitless
$C_{p_{ideal}}$	Ideal Coefficient of Power, unitless
$C_{p_{induced}}$	Induced Coefficient of Power, unitless
P	Power, watts
k	Induced power factor coefficient, unitless
Q	Torque, $N * m$
C_Q	Coefficient of Torque, unitless
FM	Figure of Merit, unitless
y	Radial distance from rotational axis, meters, unitless
ϕ	Induced inflow angle, radians
α	Angle of attack, radians
θ	Blade Pitch Angle, radians
α_0	Blade Pitch angle for Zero Lift, radians
L	Lift, Newtons

D	Drag, Newtons
F_x	Resultant force, x-direction, Newtons
F_z	Resultant force, z-direction, Newtons
r	Non-dimensional radial position
λ	Induced Inflow, unitless
F	Prandtl's Loss Factor, unitless
f	Prandtl's Loss Factor Function Input, unitless
N	Number of radial elements
n	n^{th} radial discretization

Subscripts:

X_T	Tangential
X_P	Perpendicular
X_C	Climb
X_i	Induced, Ideal
X_0	Profile, far up field
X_∞	Vena-contracta demarcation

Mathematical Operators:

Δ	Numerical differential term
dX	Calculus differential term
$\sum$	Numerical Summation

Acronyms/Abbreviations:

BL	Boundary Layer
CFD	Computational Fluid Dynamics
DEP	Double Edged Plate
IRSEV	Interplanetary Robotic Surface Exploration Vehicle
JPL	NASA Jet Propulsion Laboratory
LSB	Laminar Separation Bubble
MH	Mars Helicopter
MHTD	Mars Helicopter Technology Demonstrator
MSH	Mars Science Helicopter
NASA	National Aeronautics and Space Administration
Re	Reynolds Number
ROAMX	Rotor Optimization for the Advancement of Mars Exploration
SLDA	Systems Level Design Approach
TS	Tollmien-Schlichting Waves
ULRE	Ultra-low Reynolds Number Flow
VTOL	Vertical take-off and landing

Chapter 1. Introduction

1.1 Project Motivation

The design and concept of interplanetary robotic surface exploration vehicles (IRSEVs) has not changed significantly since the 1970s. The current approach for exploring other planets is to send a single-unit system to perform science experiments there. The scope of today's IRSEVs are limited to just ground-based or aerial-based exploration vehicles. Each of these are uniquely posited towards specific goals and are limited by their mode of transportation. Ground-based vehicles move very slowly; NASA's 2012 Curiosity rover and 2020 Perseverance rover have top speeds on hard, flat ground of 0.0894 MPH (NASA, 2019a; NASA, 2019b) and 0.0939 MPH (NASA, n.d.), respectively. Over the course of the nine years Curiosity has been on Mars, it has only traversed a distance of 15.44 miles (NASA, n.d.) Aerial exploration vehicles, like the planned "Dragonfly" mission to Titan, will have an expected capacity of flying 13 miles per charge (WennersHerron, 2019). The difference in rates of transportation are staggering. It should be noted that the atmospheres of Mars and Titan are very different – the Martian atmosphere is only 0.36% as dense as Titan's atmosphere (Coustenis, n.d.) This stark difference in atmospheric density plays a significant role in developing a rotor propulsion system for Mars that would be able to sustain enough lift and thrust for an airborne vehicle that encounters ultra-low Reynolds number flow (ULRE).

An IRSEV capable of sustained flight would be able to explore and gather data about larger areas of interest from an aerial perspective. NASA has recognized this advantage and has sent Ingenuity — the first helicopter to ever fly in another planet's atmosphere – to Mars, which arrived in February 2021. The first flight of Ingenuity is scheduled for no earlier than the first week of April, 2021 (NASA-Mars, 2021). This event is historic in nature and can be regarded in the same magnitude of importance as the Wright Brother's first flight in 1903.

Ingenuity is a co-axial, two bladed rotorcraft that has an expected endurance of 90 seconds, a hover altitude of 10-15 feet, and range of nearly 1,000 feet (NASA Ingenuity, n.d.). Ingenuity's mission is purely proof-of-concept and is a technology demonstrator effort; the rotorcraft carries no scientific instruments. It is with great hope that the data from Ingenuity's first flights would be made publicly available such that this research project could be better informed from the results of true Martian flight and rotor aerodynamics.

The next logical step in progression of vehicle development and testing would be to design and develop a fixed-winged drone for Mars exploration. Proving such a vehicle could sustain prolonged flight time on Mars opens the door to many new avenues of atmospheric planetary exploration.

Figure 1: Picture of the Ingenuity helicopter. Reproduced from NASA Ingenuity (n.d.)

Moreover, NASA's interest in flight vehicle exploration of Mars extends beyond that of Ingenuity. NASA's Space Technology Mission Directorate has recently invested in a new research team within the NASA Ames Aeromechanics' Branch. ROAMX – "Rotor Optimization for the Advancement of Mars eXploration" – is a team of early career professionals who have been granted $2.5M to study this emerging field:

> "The ROAMX Project will significantly enhance rotorcraft capabilities on Mars, thereby enabling a vast expansion of science experiments and exploration of the surface and atmosphere of Mars. The work proposed will lead to an optimized rotor using novel unconventional airfoils and rotor blades for use in future-generation advanced Mars rotorcraft which significantly increase payload capacity, speed, and range. To accomplish these goals, the focus of this research

is to mature optimization of airfoils and blade geometries for advanced Mars rotorcraft and to experimentally validate and demonstrate rotor performance improvements" (Segall, n.d.).

ROAMX's work is related to ultra-low Reynolds number (ULRE) performance optimization and the effects it has on airfoils and rotor blades.

For some context, Re is defined as the ratio of inertial to viscous forces within a moving fluid. For high Re, the resulting flow field is turbulent in nature (i.e. chaotic, time variant); for low Re the flow field is laminar in nature (i.e. orderly, uniform, time-invariant). What's unique about Re is that if the flow conditions or test article size available is different than what is being designed for, the results would be valid as long as the Re is matched in both cases. Moreover, decreasing Re leads to a relative strength increase of viscous forces which resultingly dampen flow disturbances and delay laminar-turbulent flow transition over the airfoil. When assessing drone or rotor performance, Re is an important scaling factor that must be closely analyzed because of its ability to describe the nature of the surrounding flow field. ULRE, like that below 10^5 in magnitude, has been relatively unexplored with respect to efficient, advanced flight vehicles. Recent research has shown that in ULRE conditions thin, plate-like airfoils outperform traditional, cambered airfoils. This is because of the rapid degradation in performance due to laminar flow separation without reattachment cambered airfoils experience in ULRE. Existing literature has shown that for a thin, plate-like airfoils in ULRE conditions the fluid is laminar, sub-critical, uniform, prone to producing laminar separation bubbles, and can produce large leading edge vortices that affect airfoil

performance. The ULRE flow condition is a primary focus of this research project because of its significant effect on airfoil and rotor performance. The effect of ULRE on a propulsion rotor model and drone flight performance is a clear gap in the advanced aerodynamics fields repertoire of tools and knowledge – one that must be further researched if Martian fixed-wing drone flight is to be achieved.

1.2 Background Information

Below is a rudimentary calculation based on data gathered about Martian atmospheric conditions that demonstrate the Re range and magnitude being considered. This calculation assumes the vehicle in question is one meter in length, and that the vehicle flies as fast as the average speed of Martian winds. The speed (Air and Space, n.d.) is assumed to be 4.44 $\frac{m}{s}$, the density is 0.01308 $\frac{kg}{m^3}$, and the viscosity (Vyriotes, 2012) is $1.422*10^{-5}$ $\frac{N*s}{m^2}$.

$$Re = \frac{\rho * V * c}{\mu} = \frac{0.01308 * 4.44 * 1}{1.422 * 10^{-5}} = 4084$$

Small, light planes, like the Cessna 150, Bonanza V35B, or T-18 at 75% of their max cruising speed near sea level conditions on Earth experience Re as low as $4.8*10^6$ and as high as $9.1*10^6$ (Koffeman, 1992). This range of Re is considered normal for this class of flight vehicles. According to a NATO AGARD report from 1985 (Mueller and Reshotko, 1985), low Re flow vehicles are considered to have magnitudes of 10^5-10^6. Therefore, the range of Re being considered in this research project are 25-250 times

smaller in value compared to the lowest normal range of low Re flight vehicles, and 1200 – 2275 times smaller than small, light airplanes. Moreover, for a typical helicopter with a blade chord of 1.5 ft in length in Earth atmospheric flight, the Re encountered on the advancing blade is approximately $8.1*10^6$ (Helicopters & Aircrafts, n.d.). It is evident that the Re range this project focuses on is arguably in a new flow category of its own – ultra-low Reynolds numbers flow.

Many environmental conditions play a significant role in developing a propulsion rotor performance model. According to a report from Phys.org by Matthew Williams (2015) our Earth atmosphere is wholly different with respect to pressure, density, temperature, and weather compared to Mars:

> "Atmospheric pressure and temperatures are another way in which Earth and Mars are quite different…Mars' [atmosphere] is very thin by comparison, with pressure ranging from 0.4 – 0.87 kPa – which is equivalent to about 1% of Earth's at sea level.
>
> Earth's atmosphere is also primarily composed of nitrogen (78%) and oxygen (21%) with trace concentrations of water vapor, carbon dioxide, and other gaseous molecules. Mars' is composed of 96% carbon dioxide, 1.93% argon and 1.89% nitrogen along with traces of oxygen and water… there is [also] a considerable difference between the average surface temperature on Earth and Mars. On Earth, it is approximately 14°C, with plenty of variation due to geographical region, elevation, and time of year…Because of its thin atmosphere

> and its greater distance from the Sun, the surface temperature of Mars is much colder, averaging at -46 °C (-51 °F). However, because of its tilted axis and orbital eccentricity, Mars also experiences considerable variations in temperature. These can be seen in the form of a low temperature of -143 °C (-225.4 °F) during the winter at the poles, and a high of 35 °C (95 °F) during summer and midday at the equator.
>
> The atmosphere of Mars is also quite dusty, containing particulates that measure 1.5 micrometers in diameter…The planet also experiences dust storms, which can turn into what resembles small tornadoes. Larger dust storms occur when the dust is blown into the atmosphere and heats up from the Sun."

These Mars environmental parameters are astoundingly different then Earth's. These differences even yield approaching rotor flight mechanics in a whole new way compared to how they have been studied and employed on Earth.

1.3 Project Scope

The fields and topics associated with researching a project of this nature are very broad – controls, navigation, guidance, data collection, power draw and energy conservation, etc. There would be many experienced engineers needed to fully develop, test, and certify such a flight vehicle for Mars; such a team was put together for designing, building, launching and piloting NASA's Ingenuity.

However, this project will not attempt to produce a fully functioning prototype vehicle. The focus of this research project is solely on the analysis of the performance of a rotor in an analogous Martian climate.

Chapter 2. Examination of Published Literature

A collection of over 40 resources from both the academic and industry domains were identified of being of relevance in preparing and fortifying a sufficient understanding of the State-of-the-Field. A selection of these resources – those of the most importance – are discussed below. Resources that are discussed or referenced directly in this Thesis can be found in the Bibliography.

This section discusses sources related to the development of a rotorcraft propulsion model and that of optimized airfoils and rotors for ultra-low Reynolds number flow conditions. Moreover, the most recent publicly available data related to the development of Ingenuity and a second-generation Mars Science Helicopter are presented.

2.1 Examination of Rotorcraft, Rotor Disk, and Propulsion Rotor Performance Analysis Methods

Dr. J Gordon Leishman's (2017, pp. 1-167) textbook, *Principles of Helicopter Aerodynamics, Second Edition,* was the primary resource used for discerning the physical theory governing and phenomena present within the analysis field of rotorcraft. Leishman begins his presentation of material related to helicopter aerodynamics by discussing the

history of rotorcraft flight. By studying the early challenges and design hurdles overcome by 18th, 19th, and 20th century engineers and aerodynamicists, this research project became better informed with the development of basic rotorcraft technology as a function of its development timeline.

Leishman proceeds with presenting an analysis of the fundamentals of rotor aerodynamics. In doing so – with use of the physical conservation equations as the basis– Leishman presents a methodology for analyzing the performance of a hovering rotorcraft by use of the Momentum Theory Analysis. A methodology for discerning and realizing the flow local to a rotor help the reader understand the aerodynamic phenomena occurring.

Moreover, several topics and quantities used in rotorcraft analysis are presented. Most notably are the discussions of disk and power loading; the induced inflow ratio; introduction to performance coefficients (like that of thrust, torque, and power); comparing physical governing theory to real, measured performance; non-ideal effects on rotor performance; induced tip losses; and momentum theory analysis in axial flight. The reader may refer to Chapter 2 of Leishman's text for more insight on these topics and their derivation.

Chapter 3 of Leishman's text presents the topics, theory, and physics related to Blade Element Analysis. Blade Element Analysis in Hover and Axial Flight, along with the derivation of the Blade Element Momentum Theory are presented and rigorously discussed. Using Blade Element Theory (BET) and Blade Element Momentum Theory (BEMT) allows for analysis of the performance of a rotor blade without needing to

perform physical tests or experimentation.[1] Most notably, Leishman presents a numerical approximation methodology for the BEMT that is easily implementable in any software language. MATLAB is of particular use due to its efficiency in processing large arrays of data.

A derivation of the physical theory, relationships, equations, and performance variables described by Leishman can be found in Chapter 3.

Winarto (2004) also presents a methodology for implementing BEMT for computational analysis. Winarto states that BEMT is a useful tool for predicting the performance of an arbitrary rotor or propeller when sufficient information related to the blade geometry and operating conditions are given. Winarto further elaborates on the required inputs to a BEMT analysis code, including (but not limited to) the environmental conditions, the blade rotational speed, blade pitch, blade sectional geometry along the span, and the sectional airfoil performance characteristics.

An alternative methodology compared to Leishman's for a BEMT code is presented by Winarto. A BEMT analysis algorithm is described in words – it is incumbent upon the reader to become sufficiently knowledgeable with the topic before attempting to create a code version for analytical purposes. Moreover, Winarto presents a complex algorithmic methodology for a numerical solution to a transcendental equation that could be used in a BEMT code analysis. This research project did not attempt to

[1] It should be noted that many simplifying assumptions are used in these analyses in order to produce estimates of the expected performance. For example, due to some of the assumptions, it is well known that for BEMT, the power and the figure of merit produced by the model are underpredicted and overpredicted, respectively (Leishman, 2017, pp.148-149). It is incumbent upon the user of such a simplified model to realize the limitations and accuracy of the model.

implement such a model, but referenced the algorithm for BEMT code development benchmarking.

McCrink and Gregory (2015) published their findings on a propulsion model for small electric unmanned aerial systems. Using BEMT modeling, the low Re range was targeted as the crux of their analysis. The model they developed is based on BEMT for a propeller, and they included corrections for tip losses, Mach effects, three- dimensional flow components, and Reynolds number scaling. Their publication is particularly focused on estimating the scale effects that are not commonly analyzed in full scale BEMT applications for large propellers or rotors.

McCrink and Gregory (2015) elaborate on existing research related to the effect of Reynolds number on rotor performance. They noted that as Re was reduced, the propulsive overall efficiency decreased. They concluded from this that there were significant Re based effects occurring for small propellers that are not present in large, high power propellers. From this, it was determined that Re effects must be modeled with first-order importance for this low Re range. However, they state that no BEMT models for small scale propellers have substantially verified this claim. Although this Thesis' scope is not that of small scale propellers,[2] the Reynolds number encountered in the Martian atmospheric conditions being considered for the rotor propulsion model are within the low- to ultra-low range and McCrink and Gregory's conclusions are relevant.

[2] The only difference between a propeller and a rotor is that a propeller's pitch with respect to the oncoming flow is fixed. A rotor can change its geometric blade pitch at any point in its revolution.

Leishman suggests evaluating the 75% rotor span location for its respective Reynolds and Mach numbers and treating that location as an average index for the entire blade. McCrink and Gregory suggest using the 70% rotor span location, instead. Both Leishman and McCrink and Gregory claim that their respective radial span position can be evaluated as the approximate location of the average force acting on the blade. However, they note that sectional aerodynamics performance parameters must be evaluated for their respective Re and Mach number. Leishman's methodology supports the same criteria for evaluating individual 2D blade section performance data along the rotor span.

Moreover, McCrink and Gregory write that with increasing rotor RPM, the changes to local Reynolds number and tip Mach number change parabolically. McCrink and Gregory note that in their analysis, the Re that was used in the BEMT model prediction was the average Re number encountered during testing. McCrink and Gregory's BEMT model output closely correlates to their experimental results and existing results for the same test articles examined, thus concluding that their assumptions and model are valid.

2.2 Examination of the Effects of Low Reynolds Number Flow on Airfoil and Rotor Performance

Argus, Ament, and Koning (2020) remark on the substantial research performed on low Re airfoils. However, they state that little research has been extended to low and

ultra-low Re rotor performance analysis, thus confirming a need for further researching this Thesis' topic.

McCrink and Gregory (2015) discuss how the efficacy and accuracy of a BEMT model is dependent on the fidelity of the sectional airfoil performance parameters used at each blade element. The spanwise change in Re and Mach number is quite appreciable – especially for small scale blades – where viscous effects become significant. This notion is valid for that of a rotor in Martian atmospheric flight conditions, too, due to the similarity of the Re range.

An additional challenge of computationally analyzing the ULRE flow domain is that of obtaining accurate and of-high-enough fidelity 2D airfoil sectional data to be used in a BEMT analysis. A common computational resource that is used in both academia and industry for producing airfoil data at a given Re and Mach number is XFOIL (or similarly XFLR5 by Deperrois (2013)) by Mark Drela (2013). Argus, Ament, and Koning (2020) note that XFOIL is effective at modeling airfoil sectional performance data for Re > 20,000. Conversely, XFOIL is not of sufficient accuracy for modeling of airfoil performance below the aforementioned Re range. Drela's XFOIL uses first-order stability theory, which diverges from experimental results when Re is <10,000. The software's operator would need to manually implement a higher order modeling approach in attempting to mitigate the errors that accumulate. Koning, Romander, and Johnson (2019) make a similar conclusion about the accuracy of XFOIL results when evaluating flow conditions of Re <10,000.

A source of decreased performance for optimized low Re airfoils is the effect the boundary layer (BL) has on the local airfoil flow field . A turbulent BL that has small scale eddying motion and is chaotic in nature causes the flow momentum to transport from the freestream to the BL. This turbulent exchange of momentum results in an increased time averaged velocity and wall shear stress within the BL. When the BL has a larger velocity and momentum, a larger adverse pressure gradient can be overcome resulting in a flow that is less prone to separation (Argus, Ament and Koning, 2020).

Argus, Ament and Koning (2020) also describe the modeling XFOIL performs for boundary layer transition. Airfoils at low Re are sensitive to local flow conditions, including freestream turbulence, blade vibration, aeroelasticity, and surface roughness. However, XFOIL's transition model is based on natural transition using an e^N model. The e^N model is used to predict the transition location caused by linear growth instabilities. The most common type of transition inducing instability is that of Tollmien-Schlichting (TS) waves. These are sinusoidal waves of pressure and velocity which cause perturbations to the BL shape. XFOIL assumes TS waves are the dominant form of instability.

Argus, Ament and Koning (2020) conclude from their study that rotor blade performance is significantly affected by the e^N model and for which critical N (Ncrit) causes transition. Moreover, the lower Ncrit is, and the higher the Re, the earlier the transition to turbulence occurs (which helps keep the shear layer attached over the region of adverse pressure gradient.) They conclude with discussing how these models are

relevant to consider for micro air vehicles, small autonomous vehicles, and extraterrestrial flight vehicles.

Koning, Romander, and Johnson (2018) researched the effect of airfoil shape on performance with respect to chord based Reynolds numbers of $O(10^3\text{-}10^4)$. They found that at ULRE, cambered and flat plates could outperform conventional airfoils with respect to performance. However, they note that there is essentially no publicly available experimental ULRE data for cambered and flat plates due to the difficulty of experimenting in these conditions and measuring data accurately. Therefore, their analysis was performed computationally as an initial means of analyzing this flow situation.

Koning, Romander, and Johnson (2018) found that for increasingly sharp leading edges, the earlier the flow transition occurred for cambered plates. The trailing edge shape was found to be of no impact on the performance of cambered plates. They note that for plate airfoils, camber is usually of positive effect on performance due to the effectively reduced angle of attack between the leading edge and freestream. Moreover, the turbulence that is generated by a sharp leading edge airfoil, with a concave plate like geometry, helps aid in lift generation and aid in keeping the upper surface flow attached. Results from experimental analyses have shown that decreasing thickness of airfoils within this Re regime improves performance. Koning, Romander, and Johnson (2018) continue their analysis by discussing the effects of smooth airfoils on performance. When Re nears and crosses below $O(10^5)$, the performance of smooth airfoils significantly degrades. The degradation is related to the resulting BL shape as a function of Re. In the

low Re range, the BL can be entirely laminar up until the point of flow separation without initiating turbulent flow reattachment or on-body flow transition. The Re for which the flow is laminar and just begins to exhibit turbulence is called the critical Re. Re for where turbulent transition occurs prior to laminar separation or after reattachment is called supercritical.

Koning, Romander, and Johnson (2018) note that in the ULRE regime, the boundary layer is more prone to separating due to an adverse pressure gradient that increase as a function of lift coefficient. Moreover, early occurring separation in subcritical flow causes large coefficients of drag, which can be of an order of magnitude greater than that for the same airfoil in supercritical flow. Figure 2 denotes the relationship between chord based Re and minimum section drag coefficient for arbitrary smooth and flat airfoils. Figure 3 demonstrates the relationship between chord based Reynolds number and maximum section lift to drag ratio. [3]

[3] Interestingly, the Re range being considered by this project's analysis is similar to what insects – like the locust – encounter when in flight. The locust's wing length based Re is nearly the same magnitude of Re as a rotor on Mars would encounter, even though their relative sizes are very different and the locust has a corrugated like shape. Although the locust has a high minimum section drag coefficient at very low Reynolds number, the flapping nature of its wings creates a leading edge vortex that allow for substantially high lift coefficients and thus help it fly.

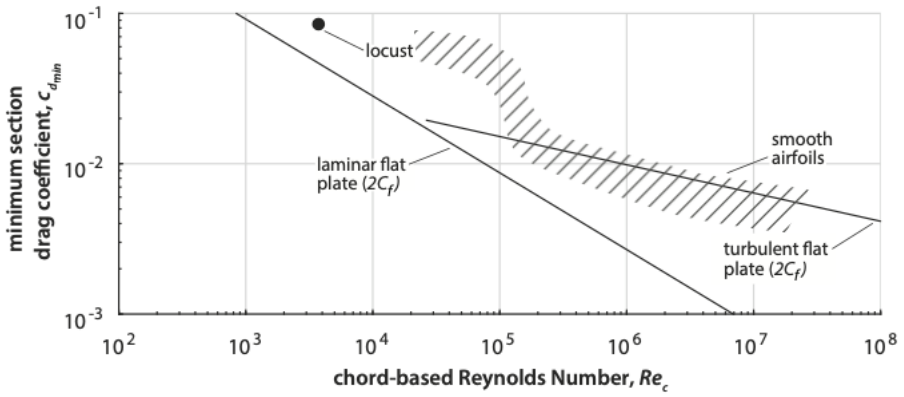

Figure 2: Cd_{min} vs. Re_{chord} for two different airfoil types. Reproduced from McMasters and Hendersen (1979)

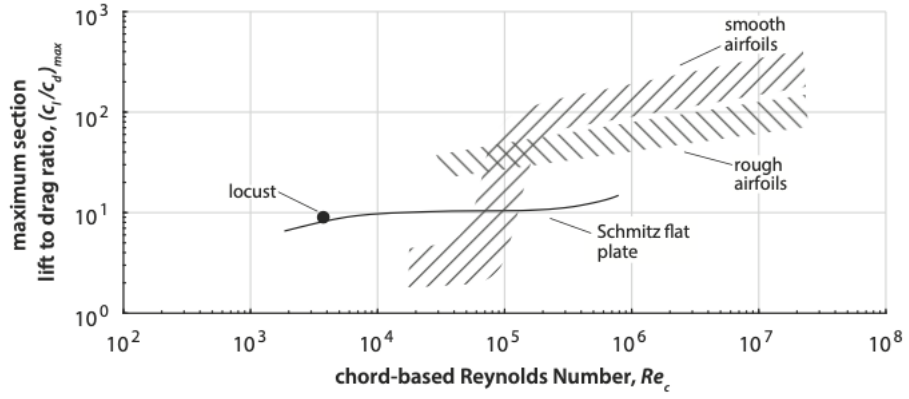

Figure 3: $(Cl/Cd)_{max}$ vs. RE_{chord} for two different airfoil types. Reproduced from McMasters and Hendersen (1979)

The boundary layer at low Reynolds number is thick, according to Koning, Romander, and Johnson (2018). Because of this, the effective camber of an airfoil is reduced and subsequently the obtainable lift coefficient is reduced, too. The rate at which the lift coefficient is negatively impacted by the ULRE flow is not equally proportional to that of the increase in drag coefficient. Thus, low lift to drag ratios for airfoils in the

subcritical state are a difficult airfoil design to work with when seeking efficient performance.

Within the boundary layer, the laminar separated shear layers are vulnerable to transition and can rapidly degrade into turbulent flow. The flow then becomes increasingly entrained and can lead to reattachment on the airfoil surface downstream. When this occurs, a laminar separation bubble (LSB) is formed. Within the LSB, the flow is recirculating at very low velocities and corresponds to a rather constant pressure distribution within the LSB. Periodic unsteadiness within the flow can cause the LSB to move along the airfoil's surface, too. The presence of a LSB at ULRE can strongly effect the airfoils expected performance, according to Koning, Romander, and Johnson (2018). If the LSB is formed near the leading edge, a leading edge vortex is formed and results in a considerable amount of flow to be induced in the radial direction along the blade span. Refer to Figure 4 for a depiction of a LSB with flow reattachment.

When analyzing this LSB flow situation two-dimensionally with a computational fluid dynamics (CFD) analysis, it is difficult to see a LSB form in the resulting velocity contour plots. This is because the 3D nature of spanwise flow cannot be captured effectively by a 2D analysis of an airfoil. Moreover, for sufficiently strong LSBs, leading edge vortices can be produced – but this only occurs in the laminar regime of ULRE (Koning, Romander, and Johnson, 2018).

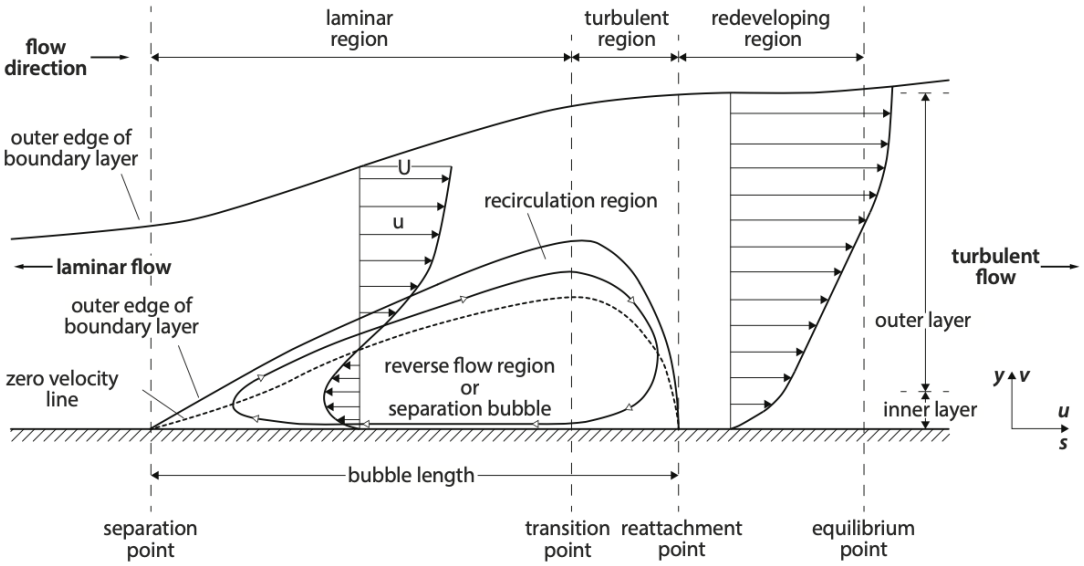

Figure 4: Elements of a steady, laminar separation bubble with turbulent reattachment. Reproduced from Carmichael (1981)

At Tohoku University in Sendai, Japan, Anyoji et al. (2010) experimentally analyzed a 5% thick flat plate and a NACA 0012-34 airfoil in ULRE, high Mach number subsonic flow (similar to that experienced by a Martian flight vehicle). They found that Mach number does not have a significant effect on flat plate performance in ULRE flow. However, Re has a significant effect on performance. For the NACA0012-34, both Mach number and Re had significant effects on performance. For this conventional airfoil shape, they found that there was a highly non-linear effect on performance due to a LSB. Moreover, for the 5% thick flat plate, compressibility of the flow was demonstrated to be of positive effect on stabilizing the separated shear layers and delaying transition to turbulence.

2.3 Examination of the State-of-the-Field with respect to Martian Flight Vehicles and their Design

The effects of low Reynolds number on rotor performance is of particular interest to NASA and has been a focus of study by the Jet Propulsion Laboratory (JPL) and the Ames Research Center in recent years.

The Martian atmosphere is 95% comprised of CO_2, with the remaining 5% being small amounts of other trace gases (Johnson et al., 2020). Table 1 demonstrates the vastly different atmospheric conditions between Earth and Mars and a comparison of Re and Mach for a representative situation. From Table 1 it is quite evident to deduce how significant the difference in density and temperature are on their impact of Re and sound speed. The effects of the low density and temperature exacerbate one another to create a situation that is practically unencountered during Earth based flight; ULRE and high Mach numbers as a result of low sound speed. Before efforts for developing a Martian flight vehicle begun, aerospace engineers hadn't attempted optimizing a flight vehicle for this situation because there has never been a need for one on Earth. Alas, human kind's desire to explore Mars via flight has brought us to tackle this very challenge.

Table 1: Mars/Earth Atmospheric Comparison. Reproduced from Johnson et al. (2020)

		Earth (N_2+O_2)	Mars (CO_2)
Density, ρ	kg/m^3	1.225	0.017
Temperature, T	C	15	–50
Viscosity, μ	Ns/m^2	0.0000175	0.0000113
Sound speed, a	m/s	340.3	233.1
Tip speed, V_{tip} (Mach number = 0.7)	m/s	238	163
Reynolds number, Re (Mach number = 0.5, chord = 0.1 m)		1,297,000	19,100

Johnson et al. (2020) remark on the fact that the low atmospheric density on Mars reduces the attainable lift per blade area that can be generated by a rotor. Additionally, the lower speed of sound on Mars reduces the maximum blade tip speed to be designed for before shocks degrade performance. Moreover, ULRE flow increases the drag coefficient and reduces the maximum lift coefficient of airfoils. As it is shown in Figure 5, the shape of optimized efficiency ULRE, high Mach number airfoils is drastically different than that of conventional, smoothed airfoils. To make the design conditions even more difficult to work with, Anyoji et al. (2010) note that the flow field is expected to have strong interactions between viscous and compressibility effects, too.

Koning, Romander, and Johnson (2019, 2020) wrote two reports that focused on ULRE efficient airfoils for a Martian rotor application that relied on an evolutionary algorithm and a genetic algorithm for airfoil geometry optimization.

Koning, Romander, and Johnson (2019) applied a genetic algorithm to a set of airfoil shapes for Martian atmospheric flight conditions in order to discern which

geometry/geometries were of best performance. The analysis performed showed that varying camber and thickness with a polygonal-like thin airfoil with sharp leading edges performed best for these ULRE flow conditions. The performance metric being optimized was lift-to-drag ratio. They further discuss how the aerodynamics of sharp leading edge, plate-like, cambered airfoils are essentially performance independent of Re. This is in stark contrast to conventional airfoils. Their finding is in concurrence with that of Anyoji et al. (2010) for flat plate performance with respect to Re. The performance increase for this aforementioned optimized airfoil geometry can be attributed to the fixing of the separation location on the airfoil due to the sharp leading edge (which is in contrast to conventional airfoils that have variable separation points).

Using the genetic algorithm, Koning, Romander, and Johnson (2019) found that a double edged plate (DEP) shaped airfoil in ULRE, high Mach flow conditions performed the best compared to a cambered plate, a conventional low Re optimized airfoil, and a triangular polygonal airfoil.

The flow condition optimized for were Re = 16,682 and M=0.52. The DEP had the highest resulting Cl/Cd ratio for this flow condition. Koning, Romander, and Johnson (2019) also noted that for all of the optimized airfoils analyzed, coherent vortices were shed, indicating that they contribute positively to the performance of the airfoils. Figure 5 defines the DEP airfoil geometry. Figure 6 shows the velocity magnitude contour of a DEP for Re = 16,682 and Mach = 0.52. Looking closely at the trailing edge of the DEP, it can be seen that the stream lines are curving and have changing velocity magnitude, indicating the presence of flow vortices.

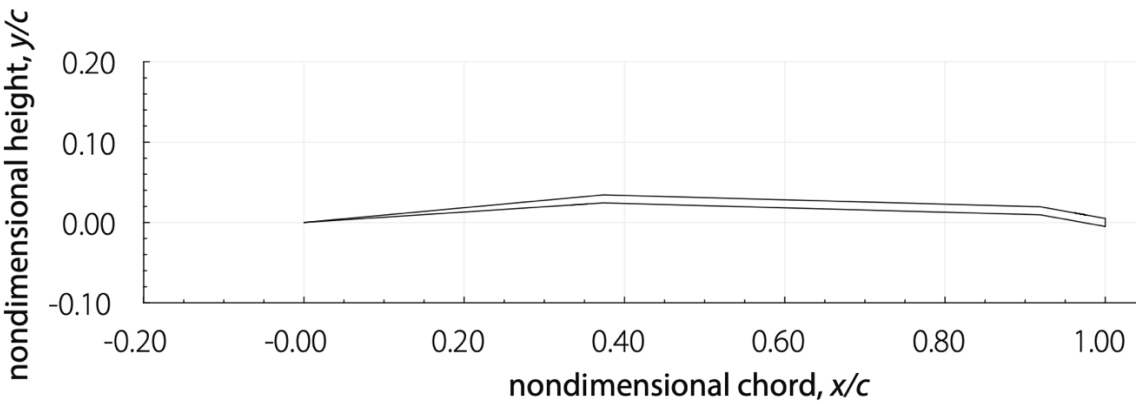

Figure 5: Optimized double edged plate for RE=16,682 and M=0.52. Reproduced from Koning, Romander, and Johnson (2019).

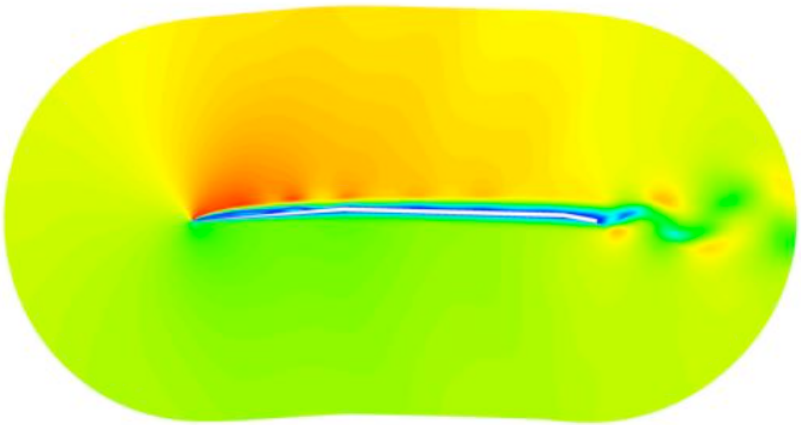

Figure 6: Velocity magnitude contour of a DEP airfoil evaluated at Re = 16,682 and M = 0.52. Reproduced from Koning, Romander, and Johnson (2019).

Using an evolutionary algorithm analysis, Koning, Romander, and Johnson (2020) note that for sharp leading edge airfoils, the shedding of coherent vortices can help reduce the separated shear layers and total flow separation from rapidly undergoing laminar-turbulent transition due to substantial entrainment of the upper-surface's

turbulent reattachment of the BL. They note that for the DEP airfoil configuration to be applied to that of a rotor, the 50-100% outboard section of the span can be thin like that shown in Figure 5. However, below 50% span and most notably nearest to the root hub, the thickness of the airfoil section would need to increase so that a spar of sufficient structural strength could be used for hub-blade integration.

In March 2020, a cohort of 16 scientists and engineers from NASA Ames, NASA JPL, and the University of Maryland collaborated on a publication of their findings related to the Mars Science Helicopter Conceptual Design (Johnson et al., 2020). This publication focuses on how a second generation Mars Science Helicopter (MSH) – one that include a suite of analysis sensors and science packages – would be designed for another aerial Mars mission. Ingenuity – the current helicopter on Mars – is solely a technology demonstrator vehicle; there are no science instruments on board. Ingenuity is also referred to as Mars Helicopter (MH) or Mars Helicopter Technology Demonstrator (MHTD).

The final design of the MSH has yet to be publicly published, however, two design options have been identified as being of highest consideration: 1) a 31kg hexacopter that could hover for 10 minutes or traverse 5km per charge carrying a 5kg payload or 2) a 25kg coaxial helicopter with similar expected performance (Johnson et al., 2020). A comparison of the size between the MSH co-axial helicopter, MHTD Ingenuity, and MSH hexacopter design are left, middle, and right, respectively in Figure 7.

Figure 7: Representative scale sizing comparison of the MSH co-axial (left) and MSH hexacopter (right) designs compared to MHTD Ingenuity (middle). Reproduced from Johnson et al. (2020).

Johnson et al. (2020) note the unique opportunity a Martian flight vehicle like this presents: performing science missions independently and/or in support of a rover mission. The MSH is being designed with the following capabilities in mind: mapping and stratigraphy of Martian terrain and slopes; polar science analysis; low latitude volatiles (like icy scarps); atmospheric science; and subsurface geophysics.

The work of Koning and his colleagues served as a basis for the information used in the design of the MSH's targeted rotor performance. Many airfoils and rotor configurations were analyzed for this MSH design (including conventional Low Re optimized airfoils, like the NACA 23012, the CLF5605, and a 5% thick cambered flat plate), however, Koning and colleagues' work related to the increased performance of the DEP was selected for use. For reference, Ingenuity's rotor planform and blade cross section are shown in Figure 8. Moreover, the total lift and drag coefficients for different Mach numbers for Ingenuity's rotors are shown in Figure 9.

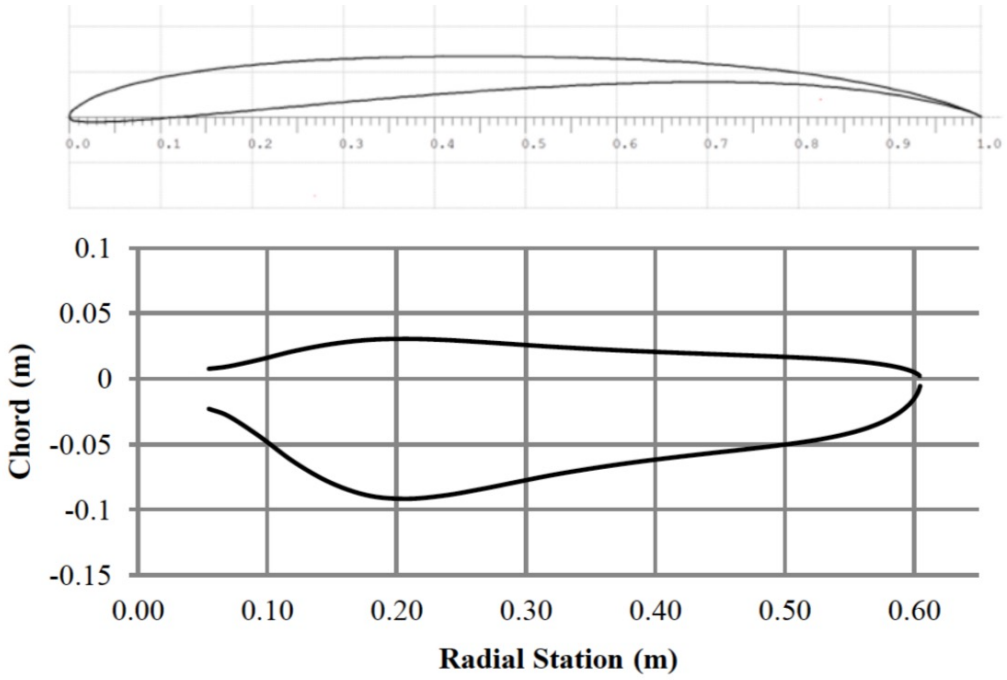

Figure 8: Ingenuity 2D blade geometry (top) and rotor planform (bottom). Reproduced from Johnson et al. (2020).

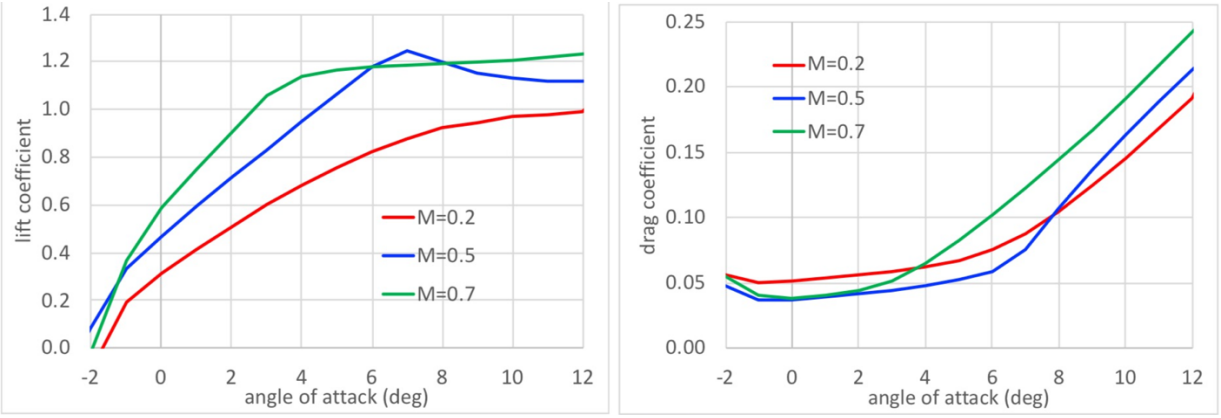

Figure 9: Ingenuity 2D blade geometry lift (left) and drag (right) coefficients as a function of geometric angle of attack for different Mach numbers. Reproduced from Johnson et al. (2020).

An experimental and computational analysis of Ingenuity's rotor blade performance has proven to have a high figure of merit – demonstrating good efficiency. Figure 10 shows the Ingenuity rotor C_T vs. FM for experimental JPL Space Simulator wind tunnel measurements and computational results using a free wake model with 2D look up tables.

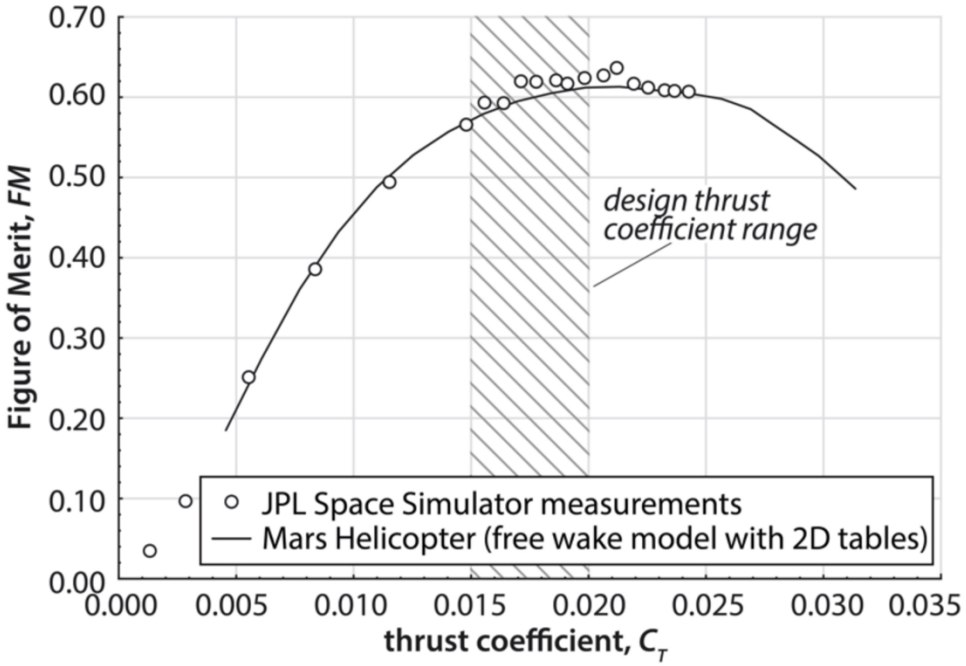

Figure 10: Experimental and computational data of hover figure of merit for the Mars Helicopter Ingenuity. Reproduced from Johnson et al. (2020).

The MSH's rotor planform and spanwise distribution of airfoil geometry have been selected by the NASA design team (Johnson et al., 2020). The airfoil geometry at four representative span locations are shown below in Figure 11- Figure 14. These airfoil geometries correspond to the 7, 25, 50 and 75-100 % span locations along the blade. Figure 15 and Figure 16 are the planforms of the blades for the co-axial and hexacopter

designs, respectively. The co-axial rotor blade has a 1.25m radius and a solidity of 0.155 and the hexacopter has a 0.64m radius with a solidity equaling 0.193.

Both design options use the same spanwise distribution of airfoil geometries like that aforementioned. Johnson et al. (2020) describe how a square tip was selected for its impact on the resulting tip vortices, which help increase performance during hover. Moreover, an optimum linear taper of $^{c_{tip}}/_{c_{root}} = 0.85$ was shown to help increase performance. Additionally, large amounts of negative blade twist was proven to be beneficial for hover and low speed rotor performance. The optimum linear twist for the MSH blade design was determined to be -18 degrees from root to tip. For the design requirements specified, a four bladed rotor is needed. The aspect ratio of the MSH hexacopter blade is 6.6 and the a single rotor disk area is 1.29 m^2.

This Thesis' analysis of an ULRE optimized rotor corresponds to that shown in Figure 11-Figure 14 and Figure 16.

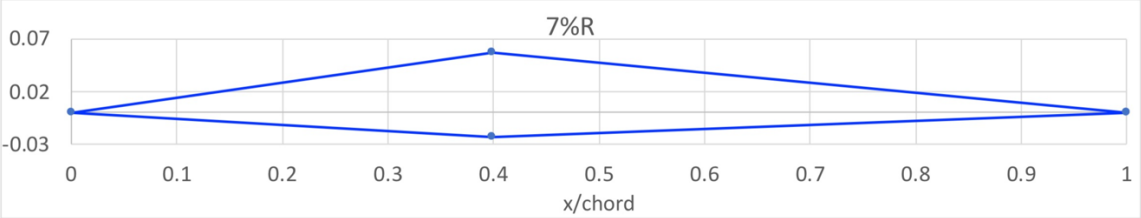

Figure 11: 7% span airfoil location geometry of the MSH rotor blade. Reproduced from Johnson et al. (2020).

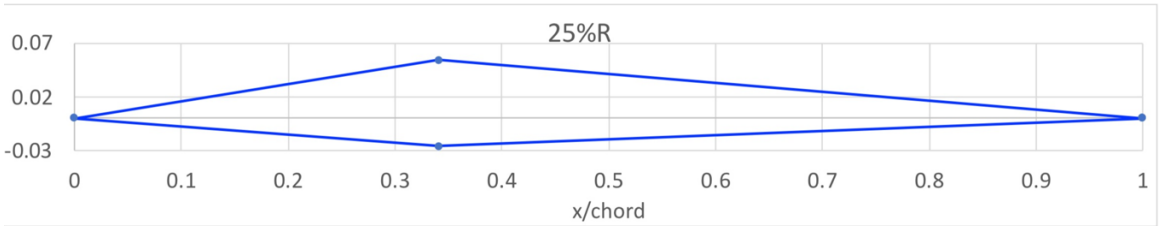

Figure 12: 25% span airfoil location geometry of the MSH rotor blade. Reproduced from Johnson et al. (2020).

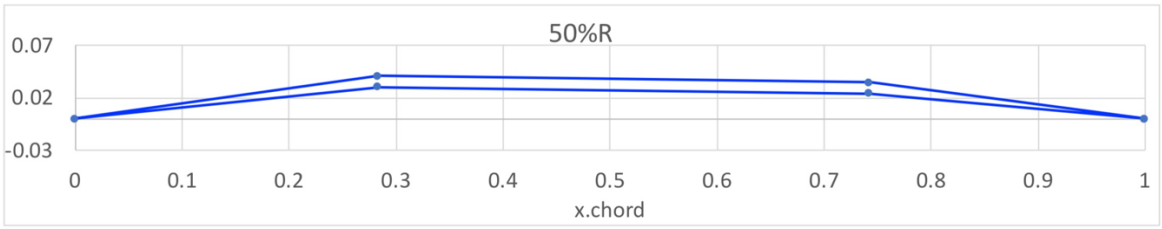

Figure 13: 50% span airfoil location geometry of the MSH rotor blade. Reproduced from Johnson et al. (2020).

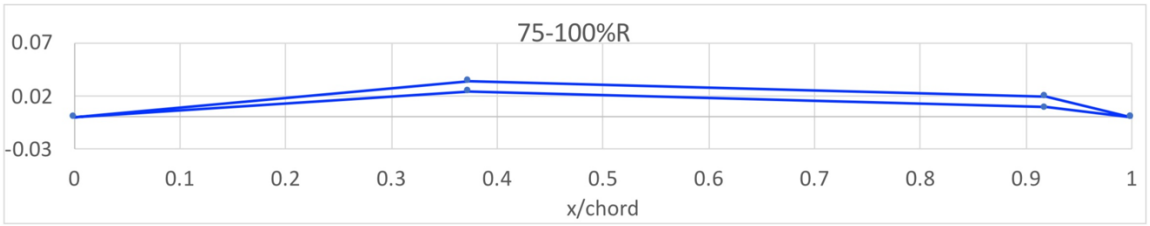

Figure 14: 75-100% span airfoil location geometry of the MSH rotor blade. Reproduced from Johnson et al. (2020).

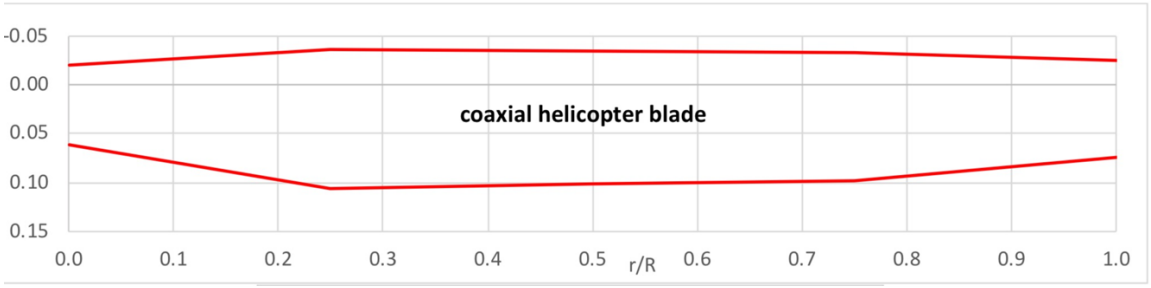

Figure 15: MSH rotor blade planform for the co-axial design. Reproduced from Johnson et al. (2020).

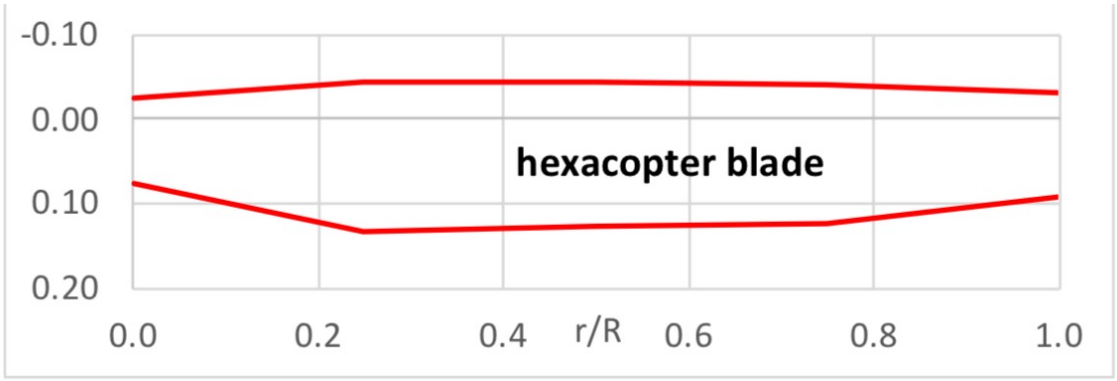

Figure 16: MSH rotor blade planform for the hexacopter design. Reproduced from Johnson et al. (2020).

Figure 17 shows an isometric view of the hexacopter blade. Linear lines connecting the aforementioned %-span location airfoil geometries are shown to demonstrate how the airfoils morph to form a solid blade.

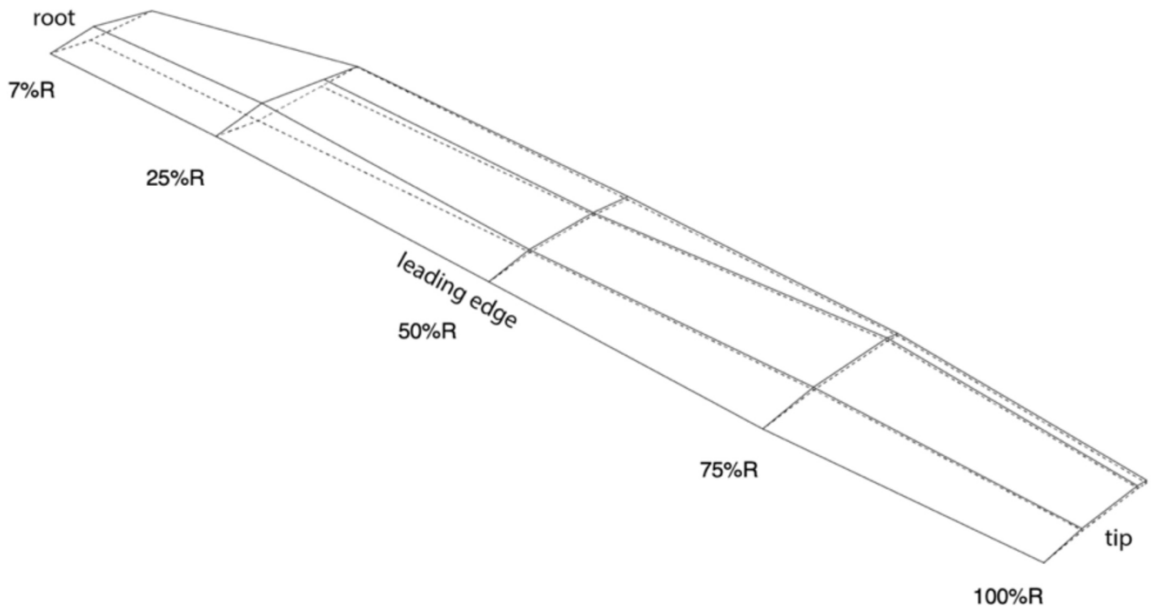

Figure 17: Isometric view of the MSH hexacopter blade design. Reproduced from Johnson et al. (2020).

Chapter 3. Fundamental Theories and Governing Equations

The Nomenclature, Acronyms, and Abbreviations Section denote all of the below variables used along with their units, if applicable.

3.1 General Equations Related to the Field of Aerodynamics

Equation (1) is the mathematical definition of Reynolds number – a dimensionless number that represents the ratio of inertial to viscous forces within a moving fluid over a given length scale. Reynolds number can be used to scale or match a flow situation when the environmental and aerodynamic conditions may not be completely reproduceable. Within the field of aerodynamics, Reynolds number is used in analysis as a similarity parameter. If the Reynolds Number is matched, then the flow field will behave the same way under varying conditions of density, velocity, length scale, and viscosity.

$$RE = \frac{\rho V l}{\mu} \tag{1}$$

Equation (2) is the mathematical definition of Mach number; a unitless number that represents the fraction or ratio of a given speed to the local speed of sound. Mach number is a function of the local velocity, ratio of specific heats, gas constant, and temperature. Mach number is also an important quantity used in aerospace engineering as a similarity parameter.

$$M = \frac{V}{\sqrt{\gamma R T}} \tag{2}$$

When a flow is outside of the incompressible flow regime (i.e. 0.3 < M < 1), then the effects of compressibility become significant and must be accounted for. Prandtl and Glaurt determined that the coefficients of lift and drag of an object could be scaled to properly reflect their correct magnitude when in this flow regime (J Gordon Leishman, 2017, pp. 150-151). Equations (3) and (4) demonstrate the Prandtl-Glaurt Mach Corrections performed on the two performance coefficients. The correction is a function of the coefficient's value at a defined value within the incompressible regime and the local Mach number.

$$C_l = \frac{C_l|_{M=0.1}}{\sqrt{1 - M^2}} \tag{3}$$

$$C_d = \frac{C_d|_{M=0.1}}{\sqrt{1 - M^2}} \tag{4}$$

3.2 General Equations Related to Helicopter Flight in the Hover Condition

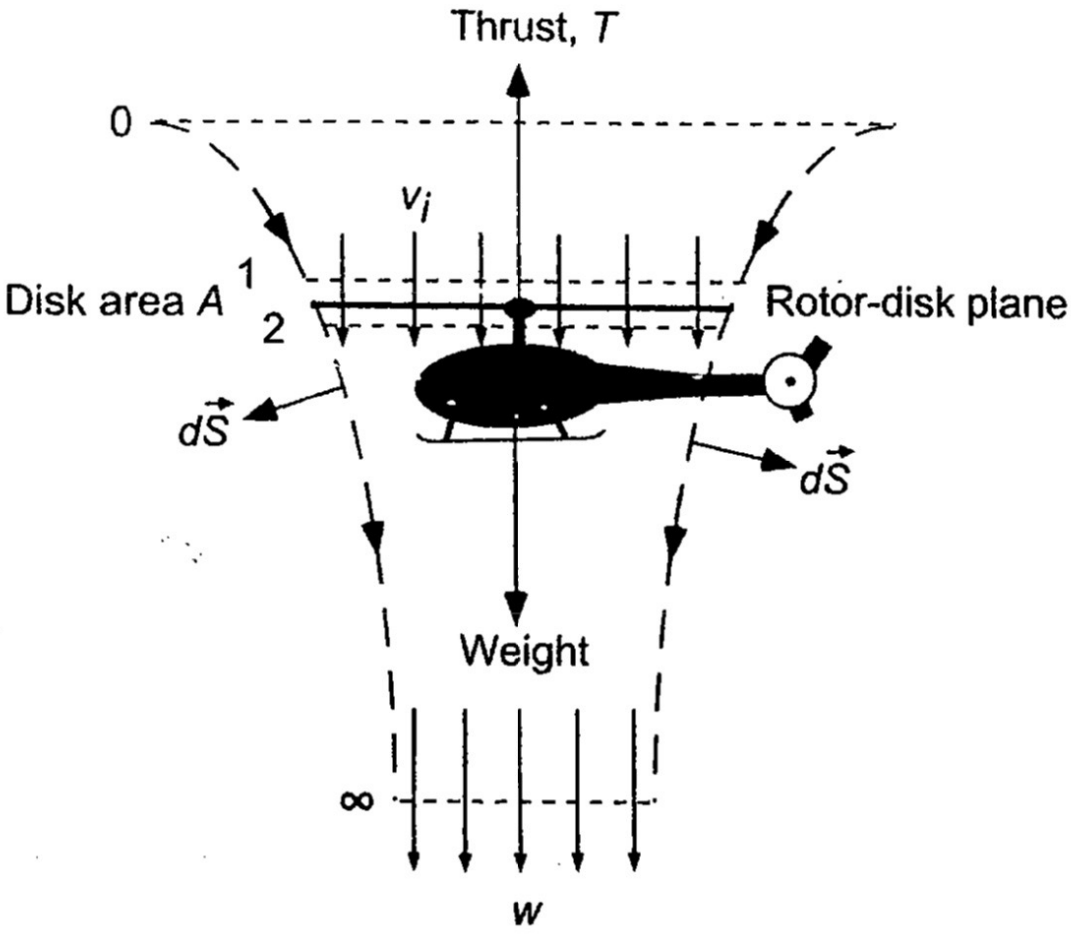

Figure 18: Flow model for Momentum Theory analysis of a rotor in hovering flight.

Reproduced from Leishman (2017, p. 61)

According to Leishman (2017, pp. 60-61), it can be assumed that the flow through the rotor disk is quasi-steady, one-dimensional, inviscid, and incompressible. The equations of conservation of momentum, mass, and energy can be applied to the control volume being considered for rotor performance analysis.

For the assumption the flow is quasi-steady, the mass flow rate through the boundaries thus must be constant. With a modification to the conservation of mass, Equation (5) demonstrates the one dimensional, incompressible flow assumption. The subscripts indicate the position described by Figure 18. The "0" and "∞" conditions of the flow field are marked. These correspond to the far up field and far downfield locations, respectively

$$\dot{m} = \rho \ A_{\infty} w = \rho \, A_2 \, v_i = \rho \, A \, v_i \tag{5}$$

The conservation of momentum links the relationship between the thrust produced by the rotor and the net time rate-of-change of momentum into and out of the control volume. Simplifying the conversation of momentum in the context of a rotor disk analysis yields the relationship shown in Equation (6): the power used by the rotor disk is proportional to the mass flow rate and velocity.

$$T \, v_i = \frac{1}{2} \dot{m} w^2 \tag{6}$$

The far downfield position within the flow field is defined as the "Vena Contracta," and it is where the velocity of the flow is equal twice that of the induced velocity (defined by Equation (12)). The Vena Contracta position and speed relationships are derived from Equation (6). Equation (7) demonstrates this relationship, where w represents the Vena Contracta velocity. The position of the Vena Contracta, relative to the rotor disk position in the axial direction is defined by Equation (8).

$$w = 2 \, v_i \tag{7}$$

$$r_\infty = \frac{R}{\sqrt{2}} \tag{8}$$

Figure 18 depicts a helicopter and its rotor disk in the hovering condition. When a set of blades is rotating in the hover condition, a finite difference in pressure is produced across the rotor disk. This difference in pressure corresponds to a smooth increase in flow velocity from above to below the rotor disk. In the hover condition, the pressure variation through the rotor disk can be found by applying Bernoulli's Equation along a streamline that begins above the rotor and passes through it to the wake. The rotating rotor disk adds energy to the flow by a inducing a pressure jump across the disk, therefore, Bernoulli's Equation cannot be applied between points in the flow across the disk. However, Leishman explains that the pressure jump across the rotor disk can assumed to be uniform, such that the equations can be applied to all streamlines contained within the control volume (Leishman, 2017, p. 64).

Equation (9) represents the application of Bernoulli's Equation between locations "0" and "1" described by Figure 18. Equation (10) describes the application of Bernoulli's Equation between locations "2" and "∞." Equation (11) is the difference of Equation (10) and (9) and denotes the total pressure jump. This pressure jump is exactly equal to the disk loading, $\frac{T}{A}$, the rotor disk experiences. This is because disk loading represents a pressure – the numerator has units of newtons and the denominator has units of m^2. The resulting quotient is a N/m^2 and explains why the aforementioned terms are equal to each other.

$$p_0 = p_\infty = p_1 + \frac{1}{2}\,\rho\,{v_i}^2 \tag{9}$$

$$p_2 + \frac{1}{2}\,\rho\,{v_i}^2 = p_\infty + \frac{1}{2}\,\rho\,w^2 \tag{10}$$

$$\Delta p = \; p_2 - p_1 = \frac{T}{A} \tag{11}$$

The velocity of the flow as a result of this pressure jump – the induced velocity – is defined by Equation (12). The induced velocity is a function of the thrust force produced by the rotor disk, the local density of the air, and the area of the rotor disk.

$$v_i = \sqrt{\frac{T}{2\,\rho\,A}} \tag{12}$$

When analyzing a rotorcraft, it is convenient to define the area swept out by the rotating blades as the "disk area." Equation (13) defines the disk area, A, as a function of the blade radius, R. Equation (14) defines the rotor solidity – a non-dimensional number representing the fractional ratio of area the blades comprise of in the total disk area. N_b represents the number of rotor blades and c represents the chord. Solidity can also be parameterized as a function of chord length if the blade planform is not constant along the span. The three mathematical definitions shown in Equation (14), from left to right, correspond to the general solidity definition, the definition for when the blade is rectangular, and the definition for when the blade has a root cutout that must be accounted for.

$$A = \; \pi\,R^2 \tag{13}$$

$$\sigma = \frac{Blade\ Area}{Disk\ Area} = \frac{N_b\,c\,R}{\pi\,R^2} = \frac{N_b\,c}{\pi\,R} = \frac{N_b\,c\,\left(R_{tip} - R_{root}\right)}{\pi\,R^2} \tag{14}$$

The thrust that the rotor disk produces as a result of its rotating motion can be defined by Equation (15). The thrust is a function of the local density, the disk area, the blade tip velocity, and the coefficient of thrust (which will be further described in the manner which it is derived in the following sub-chapter).

Moreover, the thrust can also be defined as a function of the mass flow rate and the Vena Contracta velocity or alternatively as a function of the induced velocity. Equation (16) – a manipulated version of Equation (15) – yields an implicit mathematical definition of the coefficient of thrust as a function of thrust. The blade tip speed can be decomposed into the rotational speed of the blade times the tip radius.

$$T = \rho A {V_{tip}}^2 C_T = 2 \rho A {v_i}^2 = \dot{m} w \tag{15}$$

$$C_T = \frac{T}{\rho A {V_{tip}}^2} = \frac{T}{\rho A \Omega^2 R^2} \tag{16}$$

Corresponding to the amount of thrust generated by the rotor disk is the amount of power and torque needed for producing such forces. Induced power is a function of the thrust force generated by the rotor disk and the resulting induced velocity. Equation (17) details the relationship for power. Note the similarity between Equations (15) and (17) – the only difference being the power of the exponent on the velocity term.

$$P = T v_i = 2 \rho A {v_i}^3 = \frac{T^{3/2}}{\sqrt{2 \rho A}} \tag{17}$$

Equation (18) is a manipulation of Equation (17) solved for the coefficient of power, C_P. Additionally, the coefficient of power can be defined as a function of coefficient of thrust, which is demonstrated in Equation (18).

$$C_P = \frac{P}{\rho\, A\, {V_{tip}}^3} = \frac{P}{\rho\, A\, \Omega^3\, R^3} = \frac{{C_T}^{3/2}}{\sqrt{2}} \tag{18}$$

Assuming no losses within the system, the ideal powered required, and thus the ideal coefficient of power required to operate is given by Equation (19). In the ideal case, C_P is a direct function of C_T.

$$C_{P_{ideal}} = \frac{{C_T}^{3/2}}{\sqrt{2}} \tag{19}$$

The real power required, and thus also the real coefficient of power required, is comprised of two components: the induced power and the profile power. Induced power is defined as the amount of power needed to operate the rotor disk to generate a given amount of thrust. The profile power is a term that represents the additional power needed to overcome the friction forces caused by the viscous fluid medium the rotor is moving through. Together, the induced and profile power sum to the total power required for operation for a given state.

Equation (20) details the induced power required, which is similar to Equation (19), but is scaled by the induced power correction factor, k. The induced power correction factor is usually determined with physical experimentation or flight testing. Its value comprises a slew of non-ideal physical effects, like non-uniform inflow, wake swirl, finite number of blades, tip losses, less than ideal wake contraction, and more. Equation (21) is the coefficient of profile power, and is a function of the rotor solidity and drag coefficient of the rotor blade. At this point in the discussion of the Momentum Theory analysis, a modification must be made due to the non-trivial effect the rotor disk has on the flow. Because of the presence of the rotor disk, a drag force is imparted as a

result of its position within the flow field. Going forward, the modified Momentum Theory will assume that the presence of an object in the flow domain will induce losses and non-ideal effects.

Equation (21) assumes that the section coefficient of drag is constant and is independent of Re and M (which according to Leishman (2017, p. 69) is a realistic first assumption).

$$C_{P_{induced}} = \frac{k\, C_T{}^{3/2}}{\sqrt{2}} \tag{20}$$

$$C_{P_0} = \frac{\sigma C_{d_0}}{8} \tag{21}$$

Equation (22) represents the sum of Equations (20) and (21). The coefficient of power will be defined as Equation (22) onward.

$$C_P = C_{P_i} + C_{P_0} = \frac{k\, C_T{}^{3/2}}{\sqrt{2}} + \frac{\sigma C_{d_0}}{8} \tag{22}$$

The torque, Q, required to meet the corresponding thrust and power requirements is given by Equation (23). Note the distinct similarity between Equation (18) and (24) – the only difference being the exponent power on the rotational velocity term, Ω. The torque required and power required differ only by an additional Ω, however, the coefficients of torque and power are exactly equal. Going forward, coefficient of torque and coefficient of power will be used interchangeably to denote the same mathematical quantity. Equation (23) defines the torque required as a function of density, disk area, blade tip velocity, and coefficient of torque. Equation (24) is a manipulation of Equation

(23) solving for the coefficient of torque. Equation (25) states that the coefficient of torque and power are mathematically identical and equivalent.

$$Q = \rho A {V_{tip}}^2 R C_Q \tag{23}$$

$$C_Q = \frac{Q}{\rho A {V_{tip}}^2 R} = \frac{Q}{\rho A \Omega^2 R^3} \tag{24}$$

$$C_Q = C_P \tag{25}$$

Within the helicopter design and analysis field, Figure of Merit is known to be the quantity used for analyzing a rotor's performance efficiency. Figure of Merit, denoted onward as FM, is the ratio of ideal power required to hover to the actual power required to hover. FM, by definition, is always less than one. One may "sanity check" their result for FM by knowing that any value calculated that is greater than one must be reanalyzed, as it is physically impossible for such a situation to occur. Equations (26) and (27) define FM in words and mathematically, respectively.

$$FM = \frac{ideal\ power\ required\ to\ hover}{actual\ power\ required\ to\ hover} < 1 \tag{26}$$

$$FM = \frac{C_{P_{ideal}}}{C_{P_i} + C_{P_0}} = \frac{\frac{{C_T}^{3/2}}{\sqrt{2}}}{\frac{k\,{C_T}^{3/2}}{\sqrt{2}} + \frac{\sigma C_{d_0}}{8}} \tag{27}$$

3.3 Blade Element Theory Analysis in Hover and Axial Flight

This section focuses on the derivation and mathematical models needed for analyzing a rotor disk by parameterizing the rotor blade into discretized sections along

the length of the span for analysis. The Blade Element Theory is relied on as the basis of the following derivation of equations (Leishman, 2017, pp. 117-120,125-127,130,140-144).

Figure 19 depicts how the resulting velocity over a rotor at any blade element position along the span can be decomposed into its normal to and out-of-plane velocities. Equation (28) defines the tangential velocity as the rotational velocity times the position with respect to the rotational axis. Equation (29) defines the perpendicular velocity as the sum of the climb velocity and the induced velocity. For the purposes of this Thesis' analysis, and the prescribed situation being that of hover, V_c is set equal to zero going forward and will be treated mathematically as such.

$$U_T = \Omega y \tag{28}$$

$$U_p = V_c + v_i \tag{29}$$

The resulting velocity is defined by Equation (30) as being the square root of the sum of the squares of each velocity component.

$$U = \sqrt{{U_T}^2 + {U_P}^2} \tag{30}$$

The resultant velocity encountered produces an effectively different relative flow angle with respect to the blade because of the out of plane velocity component. This difference can be realized by its vector angle and is defined in Equation (31). The relative inflow angle, ϕ, is the induced angle of attack the blade element perceives as a result of the inflow. Equation (31) denotes the mathematical definition of ϕ, and the result when assuming the small angle approximation.

$$\phi = \tan^{-1}\left(\frac{U_P}{U_T}\right) \approx \frac{U_P}{U_T}\ for\ small\ angles \tag{31}$$

The blade element's true or effective angle of attack can be defined by Equation (32). The effective angle of attack, α, is a sum of the blade pitch angle, the angle corresponding to zero lift for the blade section, and the inflow angle.

$$\alpha = \theta - \alpha_0 - \phi \tag{32}$$

Going forward, θ will represent $\theta - \alpha_0$ for brevity's sake.

Moreover, the coefficient of lift per blade section can be defined by the blade section's lift curve slope, C_{l_α} and the effective angle of attack, α. Equation (33) denotes this relationship.

$$C_l = C_{l_\alpha}(\theta - \phi) \tag{33}$$

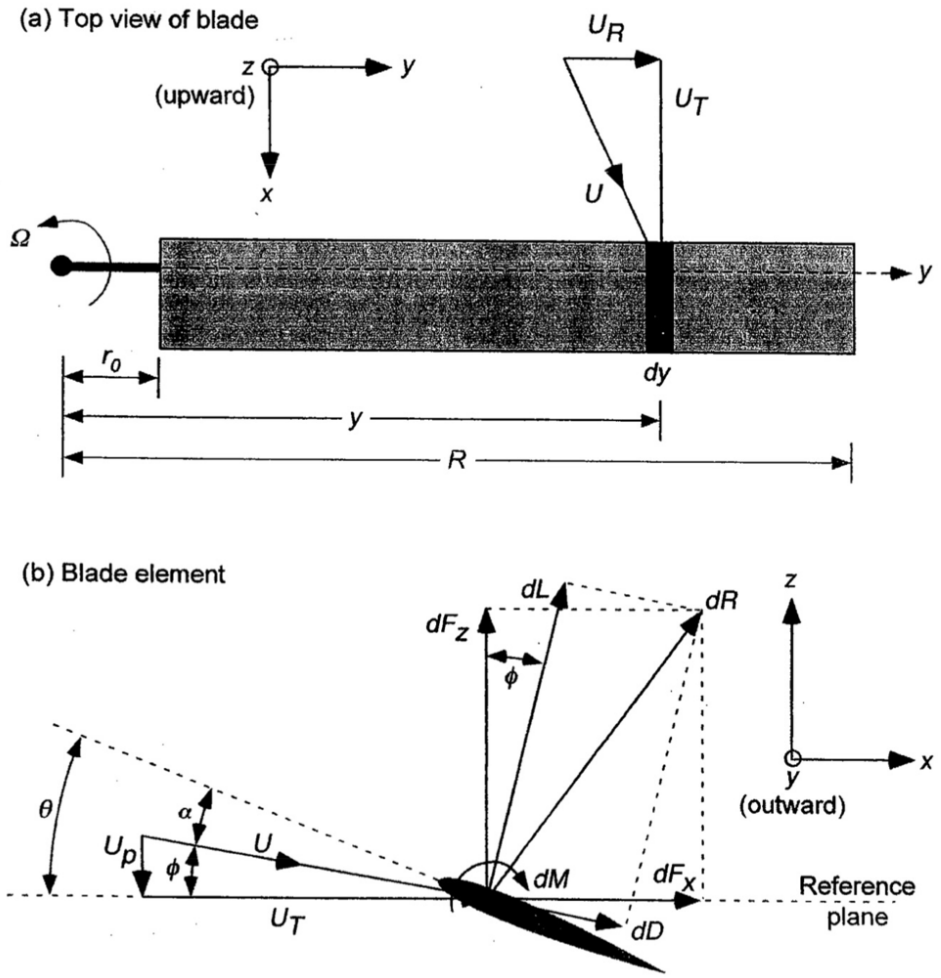

Figure 19: Physical realization of the aerodynamic environment and velocities present for a blade element. Part A is a top view of a single rotating blade. Part B is an orthogonal blade element view. Reproduced from Leishman (2017, p. 116)

Relying on the reader's general knowledge about the field of aerodynamics and Figure 19 above for refence, Equations (33)-(39) define the differential lift, drag, normal, horizontal, and thrust forces along with differential torque and power per blade element.

$$dL = \frac{1}{2}\,\rho\, c\, U^2\, C_l\, dy \tag{34}$$

$$dD = \frac{1}{2}\,\rho\, c\, U^2\, C_d\, dy \tag{35}$$

$$dF_x = dL \sin\phi + dD \cos\phi \tag{36}$$

$$dT = N_b\, dF_z \tag{37}$$

$$dQ = N_b\, dF_x\, y \tag{38}$$

$$dP = N_b\, dF_x\, \Omega\, y \tag{39}$$

Equations (40) - (42) represent the component summation of the differential thrust, torque, and power as a function of the number of rotor blades, the induced angle of attack, the radial position, and the rotational velocity of the rotor.

$$dT = N_b\, (dL \cos\phi - dD \sin\phi) \tag{40}$$

$$dQ = N_b\, (dL \sin\phi + dD \cos\phi)\, y \tag{41}$$

$$dP = N_b\, (dL \sin\phi + dD \cos\phi)\, \Omega\, y \tag{42}$$

Reproduced from Leishman (2017, p. 118), the following numerated assumptions are relevant to the state of the helicopter in hover or axial flight and the axisymmetric nature of the aerodynamic environment. These assumptions are only applicable to the rotors and do not consider the effects the helicopter body and structure. The air loads experienced by the rotor disk are independent of blade azimuth angle in the hover and axial case.

1. "The out-of-plane velocity, U_P, is much smaller than the in-plane velocity, U_T, so that $U = \sqrt{{U_T}^2 + {U_P}^2} \approx U_T$. This is a valid approximation except near the blade root, but the aerodynamic forces are small here anyway.

2. The induced [flow] angle, ϕ, is small, so that $\phi = {U_P}/{U_T}$. Also, $\sin\phi = \phi$ and $\cos\phi = 1$.
3. The drag [force] is at least one order of magnitude less than the lift, so that the contribution of $dD \sin\phi$ (or $dD\ \phi$) is negligible."

When these aforementioned simplifications are applied to the equations presented, the resulting differential thrust, torque, and power are:

$$dT = N_b\, dL \tag{43}$$

$$dQ = N_b\, (dL\, \phi + dD)\, y \tag{44}$$

$$dP = N_b\, (dL\, \phi + dD)\, \Omega\, y \tag{45}$$

It is advantageous to define some quantities non-dimensionally as to reduce the number of working variables per equation. Lengths are divided by rotor radius, R, and velocities are divided by blade tip speed, ΩR. Equation (46) defines a non-dimensional position, r, as a ratio of arbitrary distance y from the rotor rotational axis to the total rotor radius, R. Equation (47) defines r an alternative way.

$$r = \frac{y}{R} \tag{46}$$

$$\frac{U}{\Omega R} = \frac{\Omega y}{\Omega R} = \frac{y}{R} = r \tag{47}$$

As a result of this non-dimensionalization, the differential thrust, torque, and power can be redefined in terms of its respective differential coefficient. Equations (48) - (50) demonstrate this.

$$dC_T = \frac{dT}{\rho\, A\, \Omega^2 R^2} \tag{48}$$

$$dC_Q = \frac{dQ}{\rho\, A\, \Omega^2 R^3} \tag{49}$$

$$dC_P = \frac{dP}{\rho\, A\, \Omega^3 R^3} \tag{50}$$

The inflow ratio, λ, is defined by Equation (51). λ is a ratio of the axial velocities to the blade rotational velocity at any arbitrary rotor span location. λ is also a function of the induced inflow angle along the span and the non-dimensional radial position. Equation (51) can be manipulated for the induced inflow angle, and is demonstrated in Equation (52).

$$\lambda = \frac{V_c + v_i}{\Omega\, y} = \frac{V_c + v_i}{\Omega\, y}\left(\frac{\Omega\, y}{\Omega\, R}\right) = \frac{U_P}{U_T}\left(\frac{y}{R}\right) = \phi\, r \tag{51}$$

$$\phi = \frac{\lambda}{r} \tag{52}$$

Using the preceding two equations, the differential coefficient terms described by Equations (48) - (50) can be redefined. Equations (53) - (56) demonstrate these modifications. Equation (54) is but a reduced, simplified result of Equation (53) representing the differential thrust coefficient for a rectangular rotor blade. The same is true for that of Equations (55) and (56), respectively.

$$\begin{aligned} dC_T = \frac{N_b\, dL}{\rho\, A\, \Omega^2 R^2} &= \frac{N_b\left(\frac{1}{2}\rho\, c\, U^2\, C_l\, dy\right)}{\rho\,(\pi R^2)\Omega^2 R^2} \\ &= \frac{1}{2}\left(\frac{N_b\, c}{\pi\, R}\right) C_l \left(\frac{y}{R}\right)^2 d\left(\frac{y}{R}\right) \end{aligned} \tag{53}$$

$$dC_T = \frac{1}{2}\sigma\, C_l\, r^2\, dr \tag{54}$$

$$\begin{aligned} dC_P \equiv dC_Q &= \frac{dQ}{\rho\, A\, \Omega^2 R^3} = \frac{N_b\, (dL\, \phi + dD)\, y}{\rho\, (\pi R^2)\Omega^2 R^3} \\ &= \frac{1}{2}\left(\frac{N_b\, c}{\pi\, R}\right)\, (\phi\, C_l + C_d)\, r^3\, dr \end{aligned} \tag{55}$$

$$dC_P \equiv dC_Q = \frac{1}{2}\sigma\, (\phi\, C_l + C_d)\, r^3\, dr \tag{56}$$

Equations (54) and (56) represent the resulting differential thrust and power coefficients as a function of differential non-dimensional radial position. These two equations can be integrated over the length of the span of the rotor blade to yield a total coefficient value. The bounds of the integrals correspond to that of the blade geometry being analyzed. The blade root cutout (also known as the blade hub cutout) is denoted by the lower bound $r = 0$ limit of integration.[4] The blade tip radius is denoted by $r = 1$ limit of integration. Equation (57) is the integral calculation required for determining coefficient of thrust. C_T is a function of rotor solidity, local effective angle of attack, and local lift curve slope.

$$\begin{aligned} C_T &= \frac{1}{2}\sigma \int_{r=0}^{r=1} C_l\, r^2\, dr = \frac{1}{2}\sigma \int_{r=0}^{r=1} C_{l_\alpha}(\theta - \phi)\, r^2\, dr \\ &= \frac{1}{2}\sigma \int_{r=0}^{r=1} C_{l_\alpha}(\theta\, r^2 - \lambda\, r)\, dr \end{aligned} \tag{57}$$

The coefficient of power can be discerned in a similar manner. However, first, the differential coefficient of power must be decomposed into its components (similarly to

[4] Note that the root cut out position is not equal to zero in dimensional coordinate space with respect to the rotation axis. The root hub cut out is a finite length from the rotor rotational axis. For the integral evaluated, it is relevant to integrate only over the length of the blade span (i.e. from root hub to blade tip) and not from the rotational axis to the blade tip.

what was performed in Equation (22)). Equation (58) is defined as such. Equation (59) is a condensed, simplified version of Equation (58).

$$dC_P = \frac{1}{2}\sigma\,\phi\,C_l\,r^3 dr + \frac{1}{2}\sigma\,C_d\,r^3\,dr = dC_{P_i} + dC_{P_0} \tag{58}$$

$$dC_P = \lambda\,dC_T + dC_{P_0} \tag{59}$$

Equation (60) defines the integral and its limits of integration for evaluating C_P. Note that Equation (60) relies on the same assumption used for Equation (21). An additional assumption is made regarding that of the inflow: it must be uniformly distributed across the blade span for Equation (60) to be valid (which is true when the rotor blade has an ideal distribution of twist).

$$C_P = \int_{r=0}^{r=1} \lambda\,dC_T + \int_{r=0}^{r=1} \frac{1}{2}\sigma\,C_d\,r^3\,dr = \lambda\,C_T + \frac{\sigma C_{d_0}}{8} \tag{60}$$

3.4 Blade Element Momentum Theory (with a Numerical Solution Approach)

Similar to the previous sub-chapter's derivation of equations related to that of an analysis of a rotor disk, the BEMT approach combines the basic principles of Momentum Theory with BET. This approach relies on equating the lifting momentum theory and circulation theory. Moreover, BEMT allows for the inflow ratio to be calculated as a function of the position along the span of the rotor.

Figure 20 depicts the rotor disk as an infinite amount of infinitesimal rings (or annuluses) that allow for analysis of the flow state and resulting differential performance per annulus. For each annulus, the physicals laws relating to conservation can be applied

and realized. At each radial position, y, from the rotational axis, the annulus has a width, dy. The resulting differential annulus area is defined by Equation (61).

$$dA = 2\,\pi\,y\,dy \tag{61}$$

Assuming the flow is only two-dimensional through the rotor disk (i.e. no velocity vector has a component that points along the direction collinear with the span of the rotor), the differential amount of thrust, dT, can be calculated using simple momentum theory. Therefore, it can be assumed that no blade section has an influence on any adjacent blade section when analyzing the section for its performance contributions. This assumption is valid everywhere except for near the blade tips, where vorticity is non-negligible and must be accounted for.

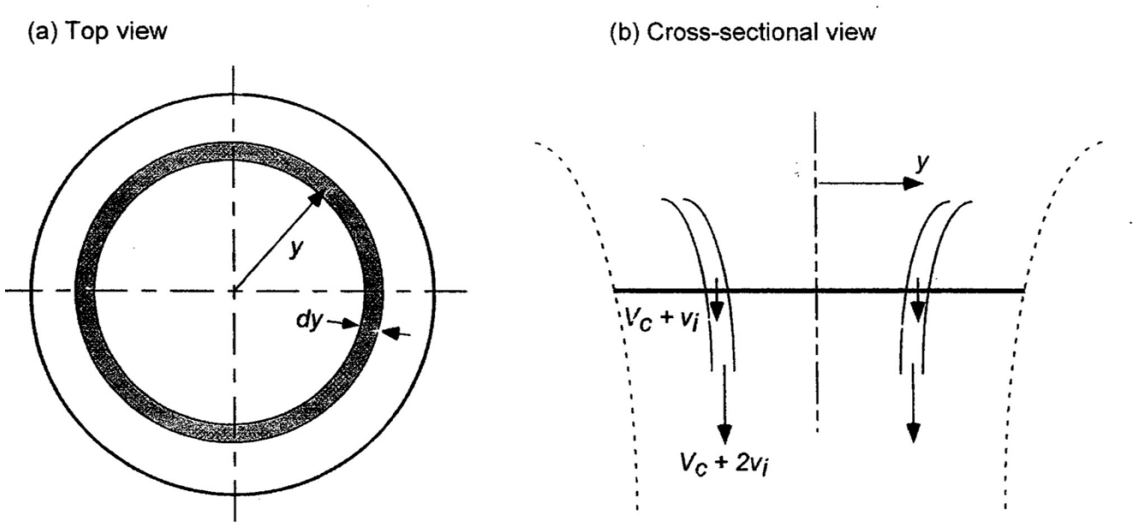

Figure 20: Depiction of the annulus of a rotor disk from two views, (a) is the top view of the annulus and (b) is the cross sectional view. Reproduced from Leishman (2017, p. 125)

Using simple momentum theory, the differential mass flow rate, $d\dot{m}$, and differential thrust, dT, can be defined. Equations (62) and (63) do so, respectively.

$$d\dot{m} = \rho\, dA\, (V_c + v_i) = 2\,\pi\,\rho(V_c + v_i)\, y\, dy \tag{62}$$

$$dT = 2\,\rho\,(V_c + v_i)\, v_i\, dA = 4\,\pi\,\rho\,(V_c + v_i)\, v_i\, y\, dy \tag{63}$$

Equation (64) is known as the Froude-Finsterwalder equation (Leishman, 2017, p. 126) and represents the differential coefficient of thrust as a function of the differential thrust determined in Equation (63). Equation (63) is most useful to work with when it is non-dimensionalized, which is demonstrated below by Equation (64). The differential coefficient of thrust on any annulus is represented simply in Equation (65).

$$\begin{aligned} dC_T = \frac{dT}{\rho(\pi\, R^2)(\Omega^2 R^2)} &= \frac{2\,\rho\, {v_i}^2 dA}{\rho(\pi\, R^2)(\Omega^2 R^2)} \\ &= 4\,\frac{(V_c + v_i)}{\Omega\, R}\left(\frac{v_i}{\Omega\, R}\right)\left(\frac{y}{R}\right) d\left(\frac{y}{R}\right) = 4\,\lambda^2\, r\, dr \end{aligned} \tag{64}$$

$$dC_T = 4\,\lambda^2\, r\, dr \tag{65}$$

The differential coefficient of induced power contribution per annulus can be defined by Equation (66), which is equal to Equation (65) multiplied by λ.

$$dC_{P_i} = 4\,\lambda^3\, r\, dr \tag{66}$$

The resulting total coefficients of thrust and induced power can be defined by Equation (67) and (68), respectively. Similar to the previous integrals presented, the limits of integration correspond to 0 and 1.

$$C_T = \int_{r=0}^{r=1} dC_T = \int_{r=0}^{r=1} 4\,\lambda^2\, r\, dr \tag{67}$$

$$C_{P_i} = \int_{r=0}^{r=1} \lambda \, dC_T = \int_{r=0}^{r=1} 4 \, \lambda^3 \, r \, dr \tag{68}$$

BEMT allows for the inflow at each radial station to be defined analytically by equating the theory of circulation with the hybrid blade element-momentum theory approach previously discussed. When equating Equation (54) from the BET analysis with Equation (65) of the BEMT, Equation (69) can be yielded.

$$\frac{\sigma C_{l_\alpha}}{2}(\theta \, r^2 - \lambda \, r) = 4 \, \lambda^2 \, r \tag{69}$$

When Equation (69) is manipulated into a quadratic form and solved for inflow as a function of its' quadratic roots, Equation (70) is yielded. Equation (70) defines the inflow as a function of the radial position and local geometric blade pitch.

$$\lambda(r) = \lambda_i(r) = \frac{\sigma \, C_{l_\alpha}(r)}{16}\left(\sqrt{1 + \frac{32}{\sigma \, C_{l_\alpha}(r)}\theta(r) \, r} - 1\right) \tag{70}$$

Mentioned earlier was the significance of vorticity at the blade tip that negates the validity of the previous assumptions made. Because of the large swirl produced by the blade tips, there is a resulting loss of thrust produced by the outermost sections of the blade. Additionally, there is a small amount of losses in thrust produced by the root hub cut out. As a result of these phenomena, Prandtl devised an estimate for approximating the thrust distribution with these losses accounted for (Leishman, 2017, pp. 141-144). Equation (71) defines the multiplier, F, that is used in the modified inflow equation (going forward defined by Equation (75).)

$$F = \left(\frac{2}{\pi}\right) \cos^{-1}(e^{-f}) \tag{71}$$

Prandtl's Loss Function takes in f as an input parameter. The input f for both the tip and the root are defined by equations (72) and (73), respectively. Both equations for f are functions of the radial position, number of rotor blades, and the inflow angle.

$$f_{tip} = \frac{N_b}{2}\left(\frac{1-r}{r\phi}\right) \tag{72}$$

$$f_{root} = \frac{N_b}{2}\left(\frac{r}{(1-r)\,\phi}\right) \tag{73}$$

The resulting F multiplier used in Equation (75) is the multiplication of the output of Equation (71) evaluated for both the root and tip f equations. Equation (74) denotes this mathematically. Equation (75) demonstrates the modified inflow equation with Prandtl's loss function implemented.

$$F = F\left(f_{tip}\right) * F(f_{root}) \tag{74}$$

$$\lambda(r) = \lambda_i(r) = \frac{\sigma\, C_{l_\alpha}(r)}{16\, F}\left(\sqrt{1 + \frac{32\, F}{\sigma\, C_{l_\alpha}(r)}\theta(r)\, r} - 1\right) \tag{75}$$

The output of Prandtl's Loss Function, F, evaluated over the span of a 3 bladed NACA 0012 with a 19% root cut out, 0.656 m radius, and 6 cm chord is depicted by Figure 21. Three cases are plotted: only the root losses, only the tip losses, and both losses as a function of non-radial position.

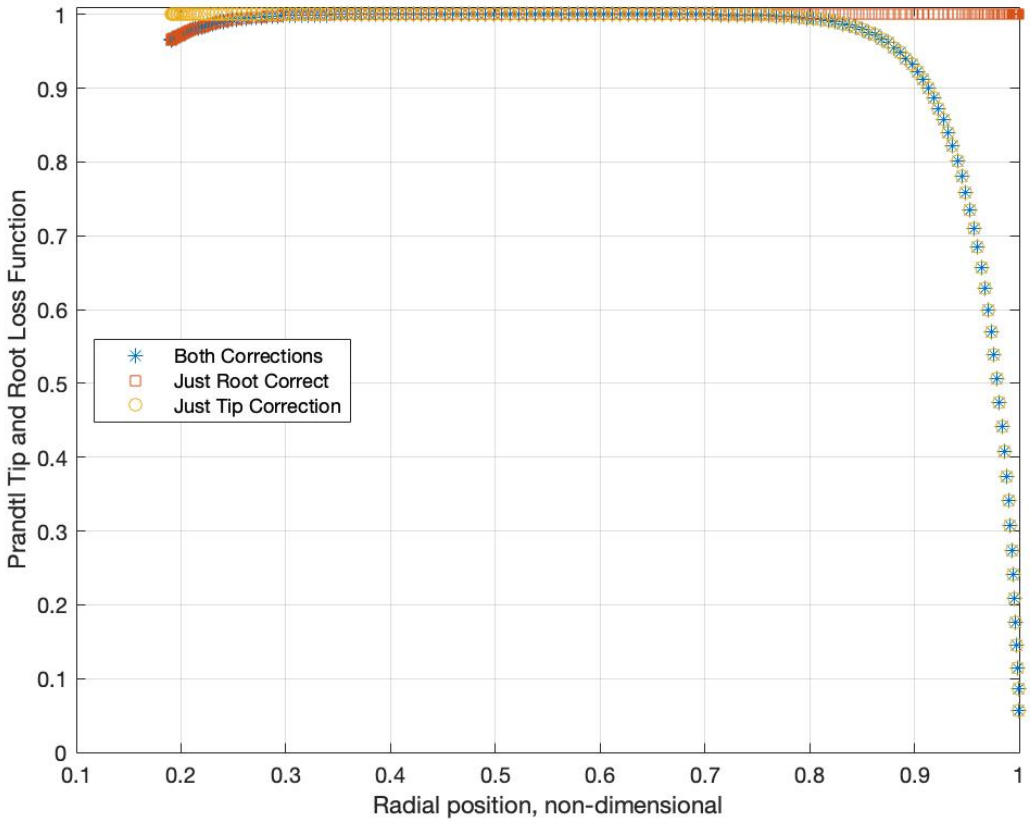

Figure 21: Prandtl's Root and Tip Loss Function output plotted as a function of non-dimensional radial position.

Arguably the most important result of the BEMT is how the model can be implemented numerically with a computer for analysis. When analyzing a rotor disk's performance, and therefore each rotor blade, the blade can be discretized into a finite number of blade elements. The division of blade elements begins at the root hub and ends at the root tip. Equation (76) represents the number of blade elements used. Leishman (2017, p. 130) notes that at least 40 or more blade element sections along the span is desirable for sufficient numerical resolution.

$$N \equiv number\ of\ radial\ stations\ discretized \tag{76}$$

$$n \equiv the\ n^{th}\ radial\ blade\ station\ \ for\ n \leq N \tag{77}$$

Equation (78) is a modified version of Equation (75) denoting how the input parameters for inflow are a function of the blade element being evaluated for, denoted by r_n.

$$\lambda_n = \lambda(r_n) = \frac{\sigma\, C_{l_\alpha}}{16\, F}\left(\sqrt{1 + \frac{32\, F}{\sigma\, C_{l_\alpha}(r_n)}\theta(r_n)\, r_n} - 1\right) \tag{78}$$

Equations (79) is the numerical modification to the differential thrust coefficient. Moreover, similarly to Equation (78), the differential thrust coefficient is evaluated for each blade element.

$$\Delta C_{T_n} = \frac{1}{2}\sigma C_{l_\alpha}(\theta(r_n){r_n}^2 - \lambda(r_n)\, r_n)\, \Delta r \tag{79}$$

Equations (80) and (81) both numerically sum the differential coefficients of thrust and coefficient of power over the finite number of blade elements discretized, respectively.

$$C_T = \sum_{n=1}^{N} \Delta C_{T_n} \tag{80}$$

$$C_Q = C_P = \sum_{n=1}^{N} \Delta C_{T_n}\, \lambda_n \tag{81}$$

Computationally, this is how one may choose to discern the C_T, C_P, and λ for a set of rotating blades. Moreover, if certain performance values are set as design points, then an inverse approach may be sought then what was presented.

Chapter 4. Computational Analysis Methodologies

4.1 Implementation of a Blade Element Momentum Theory Analysis

The development of the BEMT analysis code began with a self-study of Leishman's (2017) text, as described by Chapter 2 and Chapter 3 of this Thesis. The BEMT code was developed with MATLAB over many months and went through multiple revisions when issues related to accuracy, efficacy, and model depth were discovered. A copy of the code developed can be found in Appendix A.

Equations (76) - (81) of Chapter 3 outline a numerical solution modification to the BEMT analysis. This numerical approach was implemented in MATLAB for producing a rotor analysis BEMT performance code. The equations used in this code relied on the entire theory section of Chapter 3 for producing meaningful rotor propulsion performance data.

The BEMT code at first was barebones in terms of its capabilities and accuracy of modeling flow phenomena. Basic BEMT capabilities like determination of the inflow at each radial station, a linear distribution of blade element section width, and evaluation of the performance coefficients were coded. Moreover, the airfoil data being used for analysis was that only of the 75% span location, which is not a correct method of analyzing the 2D sectional performance coefficients at each radial station. However, as more familiarity with the modeling technique progressed with further study of Leishman (2017), Winarto (2004), and McCrink and Gregory (2015), a more complete and accurate BEMT code was developed.

Further iterations of the BEMT code included root and tip corrections to the inflow according to Prandtl's loss factor model (Leishman, 2017, pp. 141-144); interpolation of coefficients of lift and drag data for each blade element location when the effective angle of attack was not exactly present in the airfoil sectional data being used; compressibility corrections on the lift and drag coefficients according to Prandtl-Glaurt's model (J Gordon Leishman, 2017, pp. 150-151); and a sinusoidal distribution of blade elements along the span such that more blade elements were concentrated towards the root and tip.[5]

XFLR5 was used for producing airfoil performance data over a sweep of angles of attack and for a given Re and Mach number. Using the "multi-threaded batch analysis" feature, a wide range of Re and Mach number airfoil performance data could be generated with low computational analysis cost. The root and tip Re were calculated using the MATLAB code. Then, sectional performance data steps of 5,000 in Re from the lowest to the highest Re for a sweep of angles of attack at a Mach number of 0.05 were exported from XFLR5. The amount of sectional performance data sets needed proportionally scales with the number of blade elements used. For each data set used, parsing of the relevant data and formatting was needed for compatibility with and import to MATLAB.

Building further upon the model, a MATLAB function was written for selecting the correct 2D sectional airfoil data to use for each blade element analyzed. The function

[5] A sinusoidal distribution was used for the blade element section width such that a focus of the flow physics surrounding the root and tip could be honed in on. The least amount of change occurs within the middle section of the blade span, thus, it was not as necessary to concentrate as many of the blade elements there.

took in as an input the blade section's Re and returned the correct set of XFLR5 data to use for discerning the lift and drag coefficients for the blade element's effective angle of attack. Depending on what Re was being evaluated for, the relevant Re range of performance data was returned for analysis.

The BEMT code developed was verified for its accuracy by attempting to reproduce the same output data when the same rotor disk input data was used from a reputable source. Chapter 3 of Leishman's (2017) text has many figures related to the output of a BEMT model for different variables at a given coefficient of torque and rotor solidity. Upon first analysis, this was not proven to be a useful means of comparison, as the BEMT code developed needed to take in rotor disk parameters, geometric blade pitch sweep, and RPM sweep as inputs – and no information from Leishman's figures were provided with regards to that. Upon further analysis of the material, a publication from Knight and Hefner (1937) was used as a data source for comparison within Leishman's figures. Leishman then used Knight and Hefner's rotor disk specifications as the inputs to his BEMT model and the figures he produced in his text.

In May 2020, a publication from NASA Ames (Harris, 2020) reproduced Knight and Hefner's data in a more accessible and readable manner (compared to the typewriter written version of the report from 1937). From Harris's report, specifics related to the rotor disk and operating conditions were discerned for use in this Thesis' BEMT code for output data comparison. The figures presented in Leishman's text for the BEMT output correspond to a 5-bladed NACA 0015 rotor disk with a 60 in. diameter, a 2.0 in chord length, a blade aspect ratio of 15, a hub diameter of 3.0 in, a root cutout of 16.7% of the

tip radius, approximately 8 degrees geometric blade pitch, and a rotational speed of approximately 1000 RPM. With these inputs set for this project's BEMT code, a C_T equal to 0.0078 and a rotor solidity of 0.1061 were produced as an output. The conditions evaluated for in Leishman's text are stated as C_T equal to 0.008 and rotor solidity equal to 0.1. It was inferred that Leishman rounded his values when stating his parameters in the production of his text's figures.

A thorough comparison of Leishman's BEMT data to this project's was performed in order to asses this project's BEMT code accuracy. Easily readable data from Leishman's figures were extracted (those that correspond to defined grid points, and not those that needed to be estimated) and were compared with this project's BEMT code in Microsoft Excel. A comparison of a selected amount of data used in the percent difference calculations are shown in Table 2.

4.2 Two-dimensional ANSYS Fluent CFD Analysis of the 7% Span Location of an Optimized ULRE Rotor

The CFD portion of this research project began with a self-study of how to operate ANSYS Fluent. Using Cornell University's online 2D airfoil CFD analysis tutorial (Weidner, n.d.), an understanding of the breadth, effort, and complexity in producing accurate and robust CFD results was learned. Many parameters, settings, and operator generated data impact the quality of the CFD results. Though a solution may be converged to, it may not be the true answer or result desired.

Weidner's (n.d.) tutorial taught how to analyze the performance of a NACA 0012 airfoil at a fixed angle of attack and velocity in standard atmospheric conditions. The CFD analysis resulted in producing plots and contours of different flow field characteristics. The tutorial provided a beginners experience to CFD and the elementary knowledge of how to use Fluent was extrapolated to analyzing a new condition.

Before the 7% span location of the MSH hexacopter rotor could be analyzed in Fluent for discerning its performance characteristics, the MSH hexacopter rotor geometry had to be reproduced. Using an online plot digitizer, each defined blade section (i.e. Figure 11-Figure 14) were recreated so that its X-Y shape coordinates could be used for analysis. Moreover, the same procedure was done for Figure 16 so that the rotor blade's planform geometry could be recreated. The data from the plot digitizer was non-dimensional coordinates of chord length and thickness, corresponding to X and Y points, respectively. Using Microsoft Excel, the output X-Y data from the digitizer was imported for plotting. Next, the blade sections and blade planform were dimensionalized using information from Johnson et al.'s (2020) publication regarding the MSH hexacopter rotor specifications. Figure 22 - Figure 26 demonstrate the reproduced blade geometries for the each defined span locations. Figure 27 shows the rotor planform and where each defined blade section is along the span. The spanwise variation of chord can easily be seen in Figure 27, which was not a view shown in Johnson et al. (2020). Note that the length scales along the X and Y axes are not equally proportional, and that the geometries presented are not to scale but are shown for demonstrative purposes.

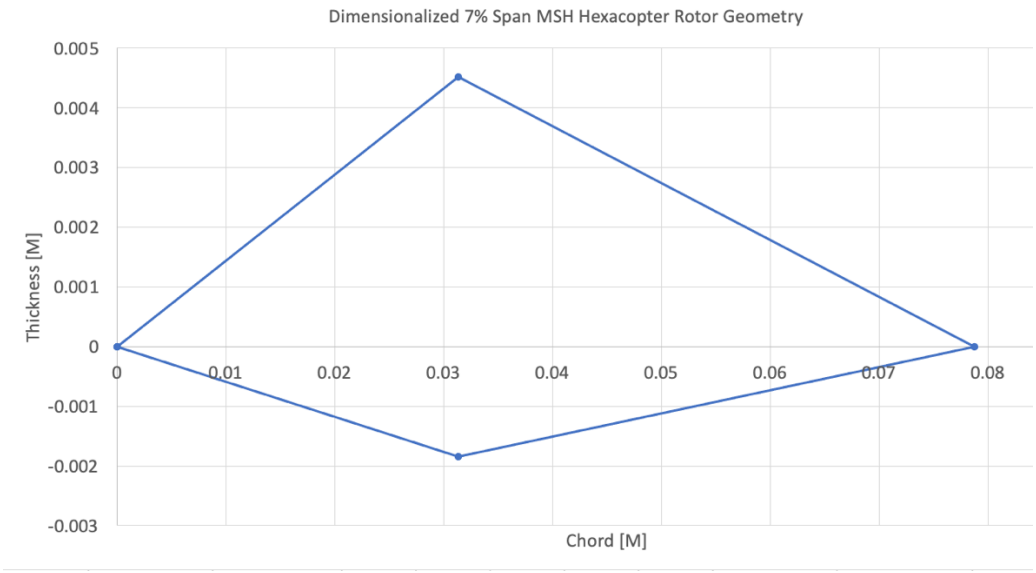

Figure 22: Dimensionalized 7% Span MSH Hexacopter Rotor Geometry

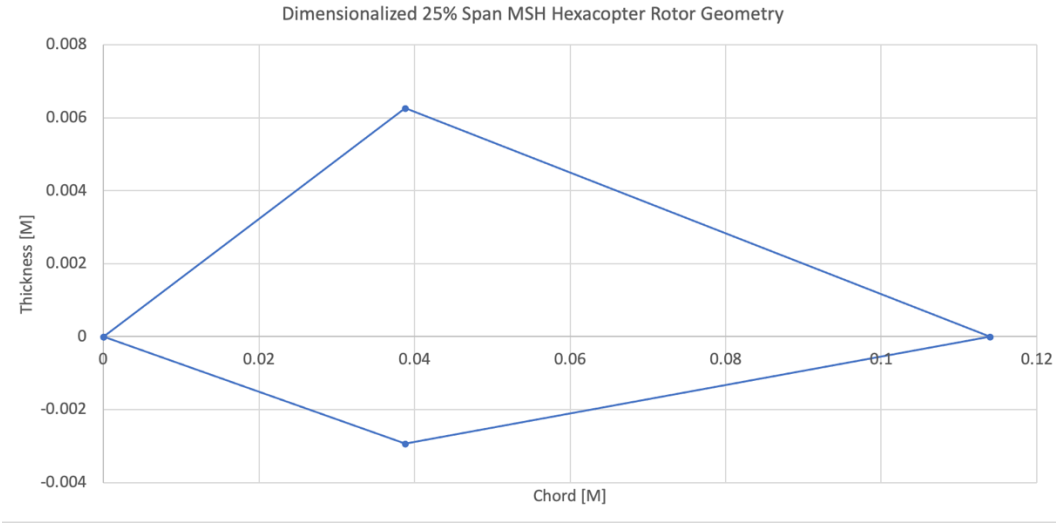

Figure 23: Dimensionalized 25% Span MSH Hexacopter Rotor Geometry

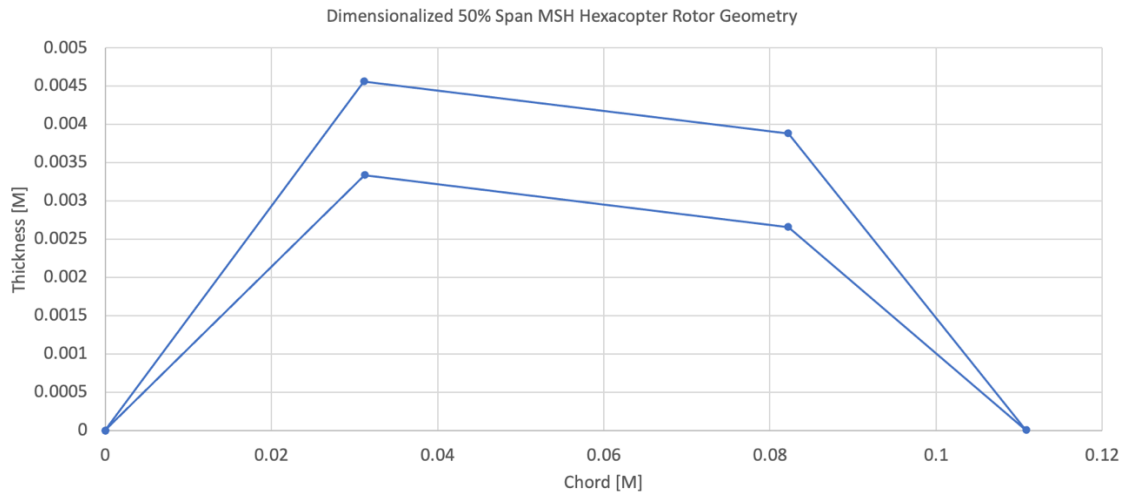

Figure 24: Dimensionalized 50% Span MSH Hexacopter Rotor Geometry

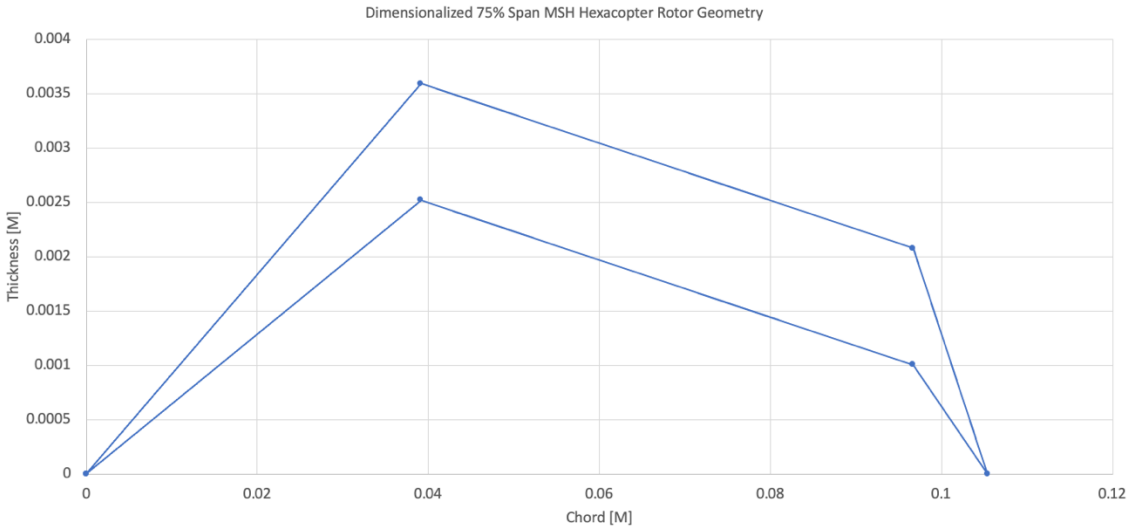

Figure 25: Dimensionalized 75% Span MSH Hexacopter Rotor Geometry

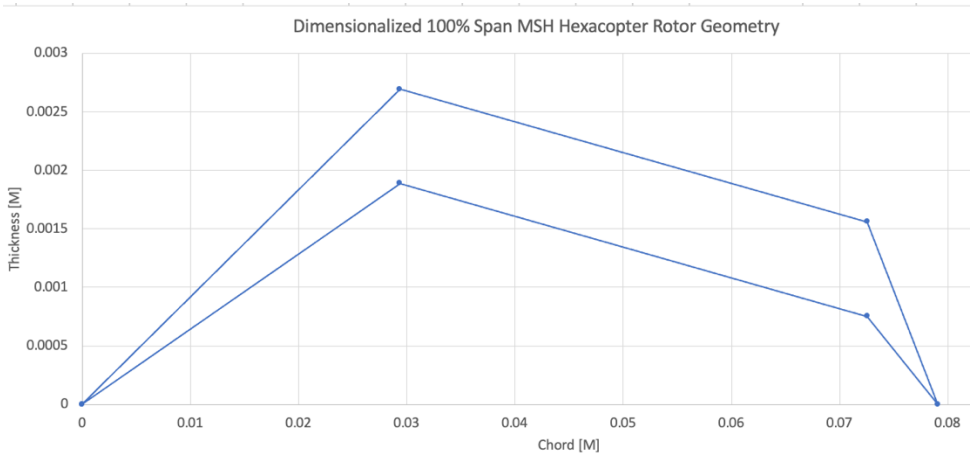

Figure 26: Dimensionalized 100% Span MSH Hexacopter Rotor Geometry

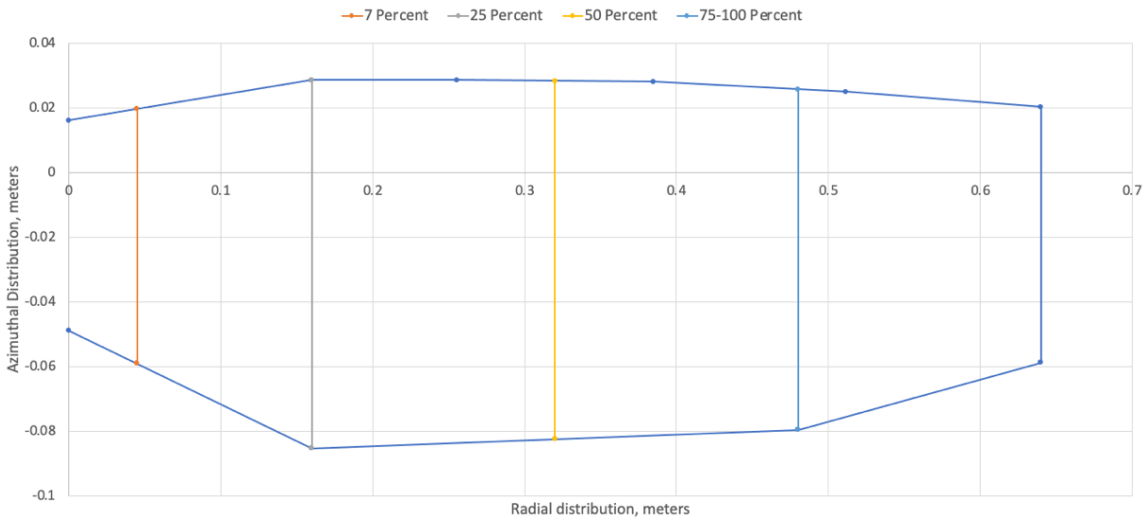

Figure 27: MSH Hexacopter Rotor Planform, Tip Radius = 0.64m

One method for analyzing a blade geometry in Fluent is with a model of the respective geometry designed with SolidWorks. For 2D Fluent flow analysis, the SolidWorks design had to be in the X-Y plane and generated as a planar surface. This process was performed on all of the defined span location blade geometries, but only the

7% span location was imported to Fluent's geometry design and modification tool, Design Modeler.

Next, a local coordinate system for the 7% span location geometry was created and the origin was placed in line with the airfoil's max thickness location and the chord line. The max thickness corresponded to approximately the 0.032m chord location. This location was specifically chosen so that the Y axis would be the separating line between the front half and back half of the airfoil's quasi-symmetric polygonal shape. The boundary and geometry of the C-Mesh (which was produced in the next step using the ANSYS Meshing tool) was created around the airfoil's origin. The C-Mesh boundary was designed to be 50 chord lengths in all directions from the airfoil's origin. Moreover, the flow domain was split into four regions for face meshing purposes. Figure 28 and Figure 29 show the local splitting of the flow domain through the aforementioned blade position and total flow domain, respectively. The horizontal line intersected the chord line through the leading and trailing edges.

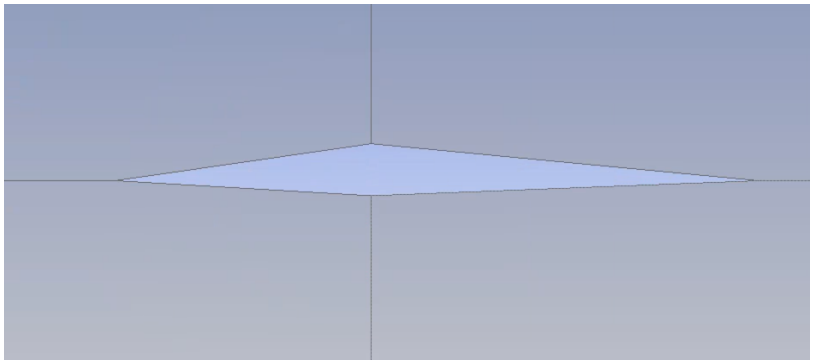

Figure 28: Local splitting of the flow domain around the airfoils sharp linear change in shape

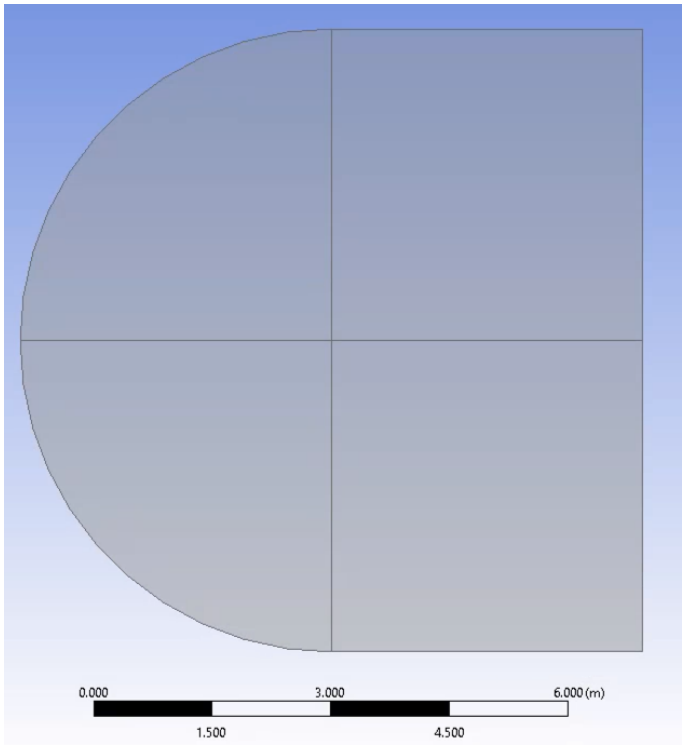

Figure 29: C-Mesh structure flow domain to be meshed and analyzed using Fluent

Next, the flow domain geometry was imported into ANSYS's native meshing tool. The front half linear sections of the blade geometry and the curved sections of the flow domain had an edge sizing applied to their sections so that a structured mesh were to be produced within the flow domain. The same edge sizing tool was used along the back half of the airfoil's linear sections. Moreover, an edge sizing and bias were applied to the flow domain's boundaries. The edge sizing bias allowed for concentration of quadrilateral cells to be focused near flow areas of interest. Specifically, these biases concentrated cells closest to the airfoil and the flow field downstream of the airfoil where the greatest interest in the flow physics was. Figure 30 shows the entire flow domain mesh. A large portion of the mesh appears totally black from this view because of the

refined nature of the mesh in those sections (i.e. the grid cell size is relatively too small from this point of view to see anything but the black cell boundaries.) Figure 31 shows the mesh local to the airfoil. Notice how the quadrilateral cells closest to the airfoil are smaller and grow larger as a function of distance from the airfoil boundary. This mesh quality is desired such that the flow physics can be more finely calculated closest to the airfoil, the boundary layer region, and the downstream flow field. The resulting mesh used had 148,200 quadrilateral cells and 149,182 nodes.

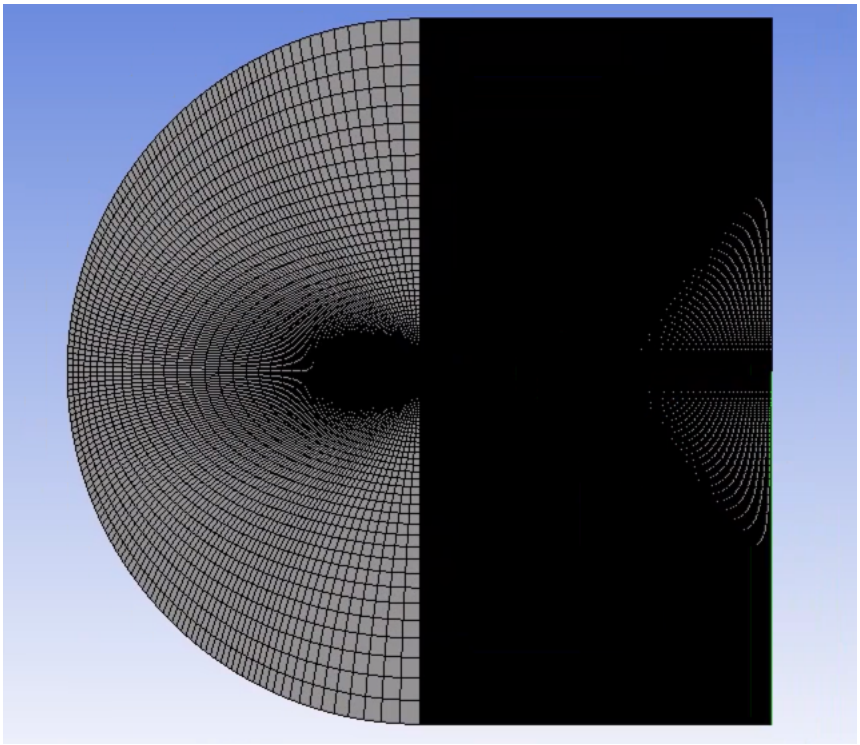

Figure 30: Structured mesh of the entire flow domain

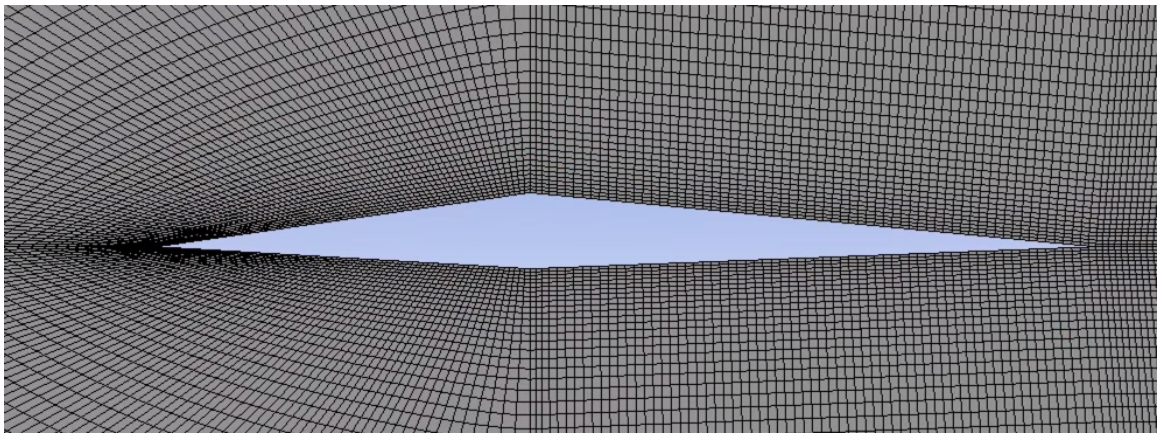

Figure 31: Mesh local to the airfoil

Due to the short natured timeline of this project and the time needed for producing Fluent results for multiple angle of attack conditions, the mesh shown was considered to be of sufficient quality once a structured nature was achieved with edge sizing and a bias of cell sizes towards regions of importance. Chapter 7 discusses what changes would be made to the mesh if there was enough time for ensuring higher mesh quality.

Next, the mesh was imported to ANSYS Fluent and the CFD analysis setup begun. The CFD analysis was performed assuming a steady state analysis, a constant flow domain density of 0.017 kg/m^3 and an operating pressure of 655 pascals. According to the literature, (Koning, Romander, and Johnson, 2020; Koning, Johnson, and Grip, 2019; Koning, Johnson, and Allan, 2018), the flow field in ULRE conditions like that experienced by a rotor on Mars is laminar. Thus, a laminar flow model was selected for the CFD analysis. Moreover, to match the Martian atmospheric conditions, the fluid used in the analysis was carbon dioxide. The density used in the analysis was the aforementioned density and a fluid dynamic viscosity of $1.13 * 10^{-5}$.

The flow conditions were manually set to be that of Re = 15,000. This Re corresponded to a flow inlet velocity of 126.6 m/s and a Mach number of 0.22. The 7% span blade geometry was analyzed at the following angles of attack: -2°, 0°, 2°, 4°, 6°, 8°, and 10°. 10° was selected as the upper limit of angle of attack analysis, as this is in the typical range of airfoil stall angles. For each angle of attack, the inlet velocity was decomposed into its vector components by means of the cosine and sine of the angle of attack.

The flow solution method was set to be least squares cell based gradient spatial discretization. Moreover, the flow was set to be of first order upwind. The solution convergence criteria was set such that absolute residual error would be assessed for each solution iteration for the x-velocity, y-velocity, and continuity until a value of less than $1*10^{-6}$ was met. Lastly, after the solution was initialized using the "hybrid initialization," the solver was set to run for a maximum of 3000 iterations with an automatic determination of the time step method.

Chapter 5. BEMT Code and ANSYS Fluent Computational Results

5.1 BEMT Comparison and Efficacy Verification Data

Table 2 represents the average percent error for each of the plots used for comparison between the BEMT model developed and that published by Leishman. The absolute average percent difference was relatively small. The five plots compared are fundamental relationships used in developing a BEMT model, and thus they were selected based on their important with respect to model efficacy and the data available.

Table 2: Percent Error Comparison of Leishman's BEMT Data and the Developed BEMT Code Data

Figure #	Depiction of	Average Percent Error between Leishman's Data and this BEMT's Data
Figure 32	λ vs. r	-7.65%
Figure 33	C_T vs C_P	2.11%
Figure 34	C_P vs. α	-7.77%
Figure 35	$\frac{dC_T}{dr}$ vs. r	-2.19% [6]
Figure 36	$C_l$vs. r	-6.45%

[6]Figure 35's data had a large outlier removed from the average percent error calculation. If it were kept in, the average percent error would be 12.36%. This large data discrepancy could be attributed to the difference in 2D performance sectional data used, as Leishman did not publish where he obtained his data from and by what means. However, the exact reason for the data point outlier is currently unknown.

Figure 32 - Figure 36 represented the differences in BEMT model produced and Leishman's data when evaluated for the same input conditions. A legend in the top left side of each plot denotes which data set is which.

Figure 32 shows the relationship between the local induced inflow and the rotor's non-dimensional radial position. Leishman did not publish a plot demonstrating the effect of Prandtl's Loss Function on the induced inflow, thus, that correction was removed for this plot. As demonstrated by the figure, the induced inflow increases in a linear-like manner from root to tip.

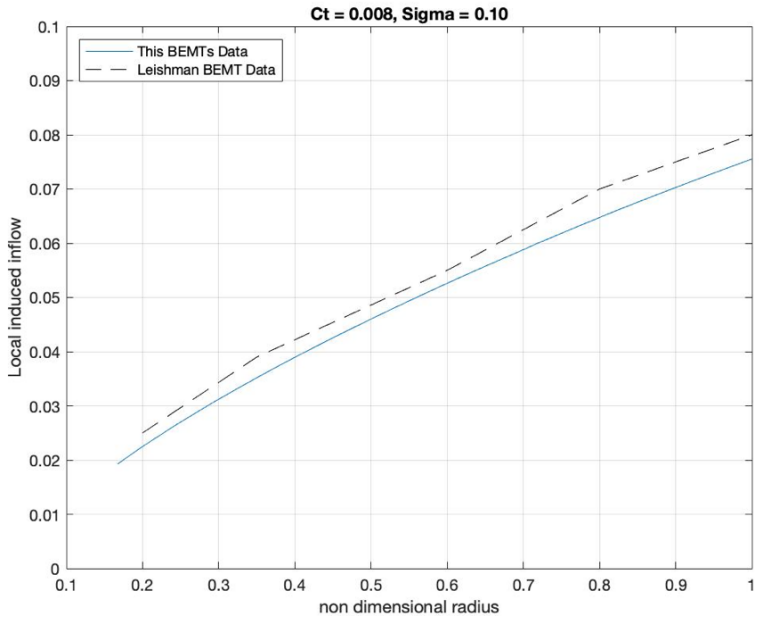

Figure 32: BEMT data comparison between this project's and Leishman's data; showing λ vs. r

Figure 33 demonstrates the relationship between coefficient of thrust as a function of coefficient of power. A quadratic-like relationship is shown between the two values, which is validated by the nature of Leishman's data.

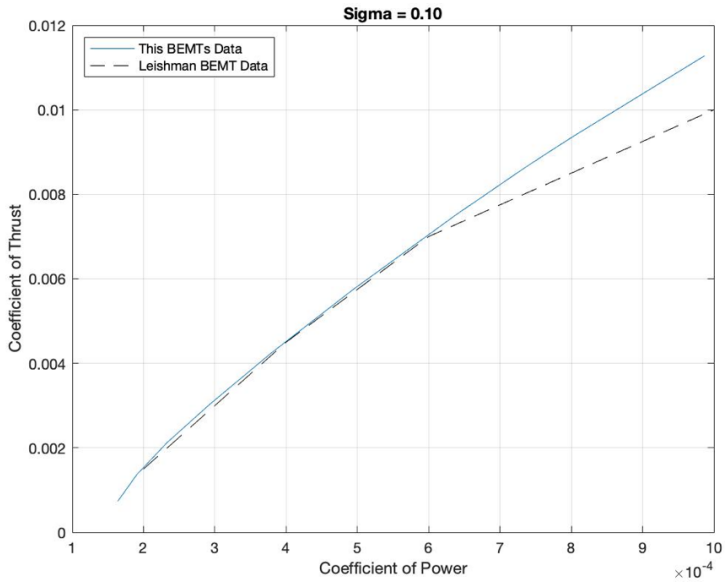

Figure 33: BEMT data comparison between this project's and Leishman's data; showing C_T vs. C_P

Figure 34 shows the relationship between coefficient of power and geometric blade pitch. The coefficient's value increases in a quadratic sense as blade pitch increases. This result is expected as C_P is a function on both C_T and C_d. As the blade pitch increases, the coefficient of thrust and coefficient of drag increases. Thus, there combined affect results in the relationship shown.

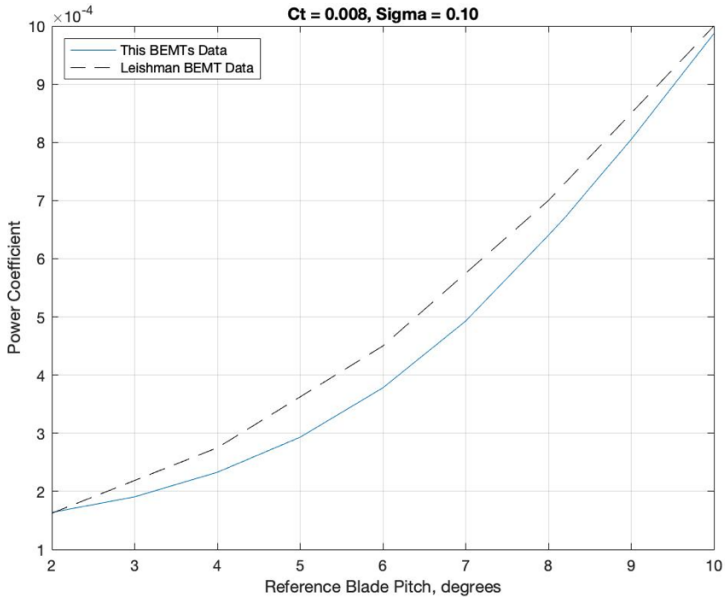

Figure 34: BEMT data comparison between this project's and Leishman's data; showing C_P vs. α

Figure 35 shows the local thrust gradient as a function of non-dimensional radial position. The data trend show was expected, as it is known that the most amount of thrust is produced in the outer portion of the rotor blade. Moreover, the figure demonstrates the effects of Prandtl's Loss Function, as the thrust gradient is driven towards zero at the root and tip.

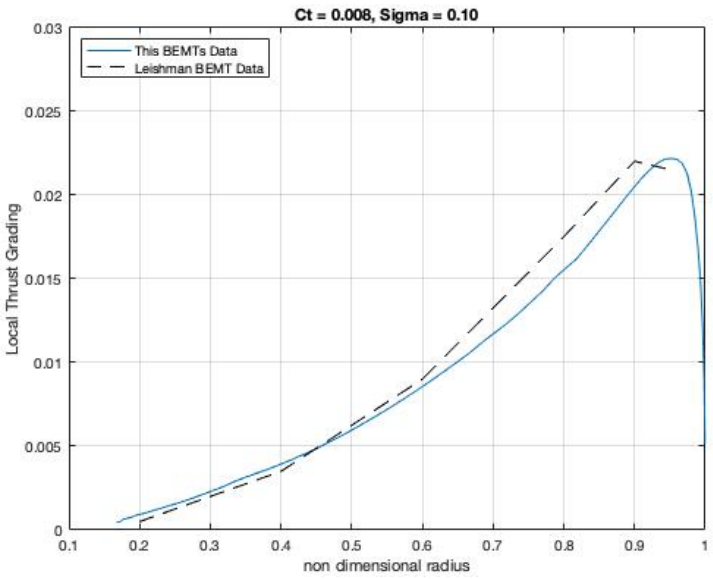

Figure 35: BEMT data comparison between this project's and Leishman's data; showing $\frac{dC_T}{dr}$ vs. r

Figure 36 demonstrates the relationship between the local lift coefficient and the non-dimensional radial position. Similarly to Figure 35, it is expected that the coefficient of lift increases along the rotor blade's span. Leishman did not publish a plot demonstrating the effect of Prandtl's Loss Function on the lift coefficient, thus, that correction was removed for this plot's data verification purpose.

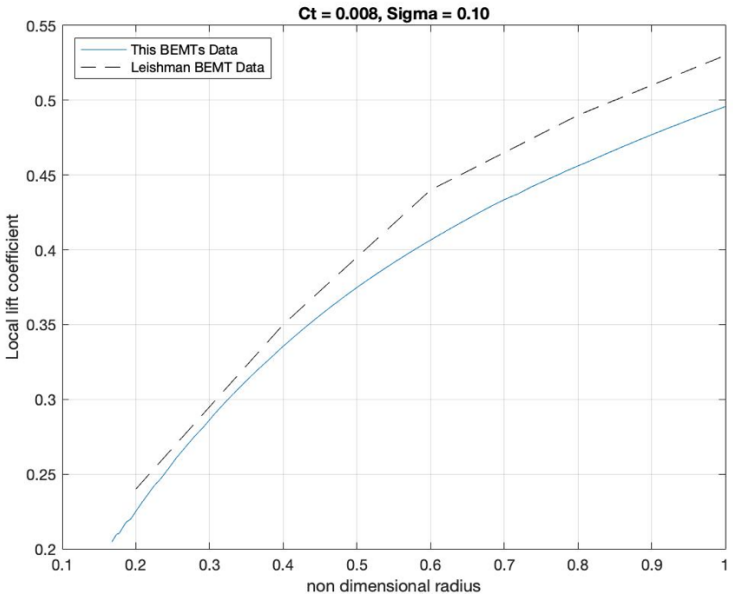

Figure 36: BEMT data comparison between this project's and Leishman's data; showing C_l vs. r

5.2 BEMT Results for a Rotor in Martian Flight Conditions Evaluated for Re = 10,000 and Re = 100,000

To demonstrate an application of the BEMT model in Martian flight conditions, an analysis was performed for $Re_{75\%\ span}$ corresponding to 10,000 and 100,000. The results presented are for showing the impact Re has on rotor performance. There are a few caveats with the results produced. The first is that the blade geometry selected for the analysis was a NACA 0012 – which is not a geometry optimized for these Re ranges and flight conditions. However, it was used as a model input because of its ease of generating data – especially with XFLR5. Second, previously discussed was the accuracy of XFLR5

when Re < 20,000 – which is the case here. Therefore, the data for the Re = 10,000 case cannot be relied on accurately.

To reiterate, the plots shown in Figure 37 - Figure 40 are purely for demonstrating the effect Re has on performance, and should not be used for any other type of analysis. As the figures show, performance decreases as Re decreases.

Figure 37 and Figure 38 show the thrust produced as a function of geometric blade pitch. The amount of thrust generated between the two cases is significantly different – by at least an order of magnitude.

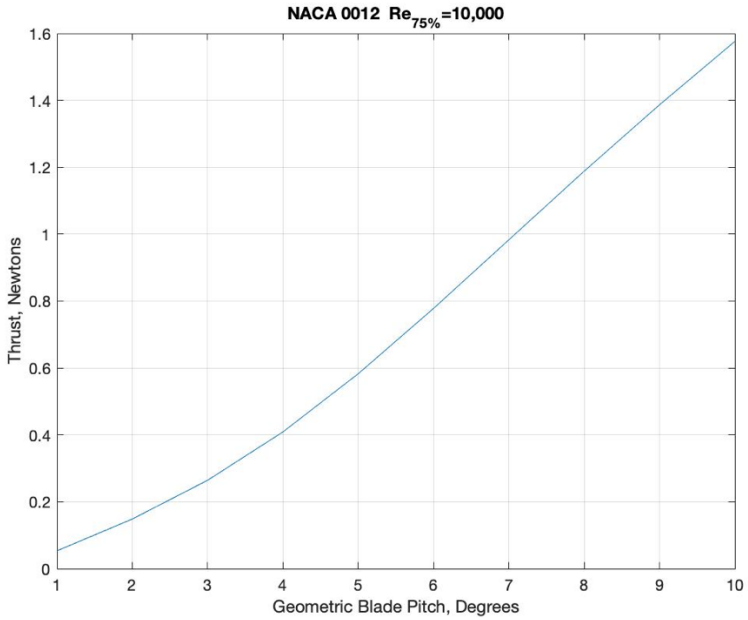

Figure 37: Thrust as a function of blade pitch for $Re_{75\%}$ = 10,000 in Martian atmospheric conditions

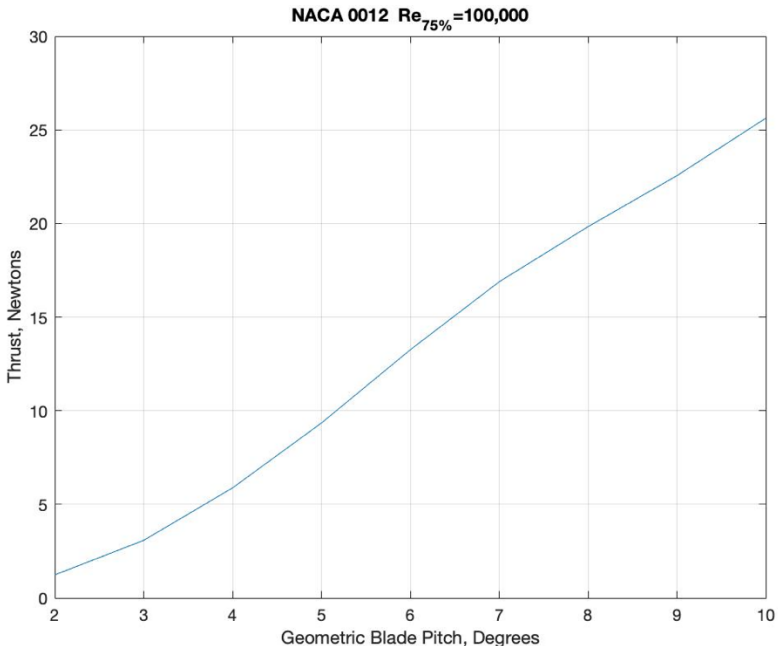

Figure 38: Thrust as a function of blade pitch for $Re_{75\%}$ = 100,000 in Martian atmospheric conditions

Figure 39 and Figure 40 demonstrate the power required to operate as a function of geometric blade pitch. There is approximately a difference of two magnitudes of order between the two Re cases. The power required to operate at higher angle of attack is a result of an increased coefficient of thrust. Thus as, coefficient of thrust increases, so does coefficient of power

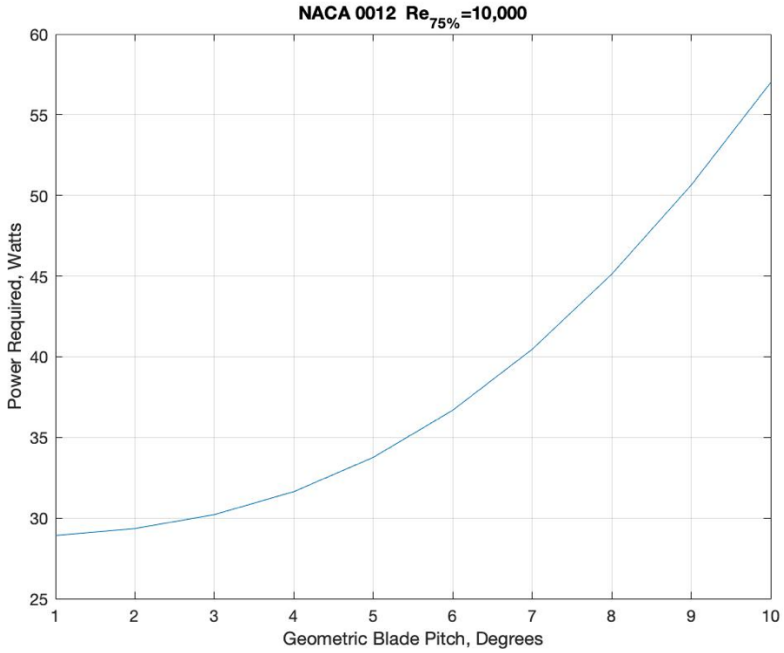

Figure 39: Power as a function of blade pitch for $Re_{75\%}$ = 10,000 in Martian atmospheric conditions

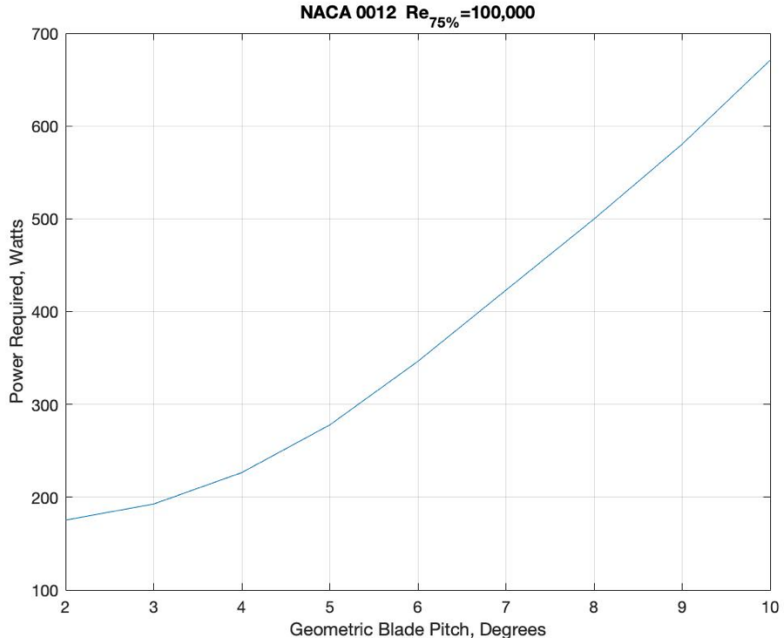

Figure 40: Power as a function of blade pitch for $Re_{75\%}$ = 100,000 in Martian atmospheric conditions

5.3 ANSYS Fluent Results of the 7% Span Location of a ULRE Optimized Rotor

The following results are for the aforementioned flow condition described by Chapter 4.2 for the 7% span location of the MSH Hexacopter rotor. For the reader's ease, the conditions are repeated in summary: Re = 15,000; M = 0.22; density = 0.017 kg/m^3; and pressure = 655 pa.

Table 3 shows the performance characteristics of the 7% span location of the ULRE optimized rotor. Figure 42 - Figure 45 are common airfoil performance representations for the airfoil analyzed.

Table 3: 7% Span Location Performance Characteristics of the MSH Hexacopter Blade

Geometric Angle of Attack (Degrees)	Coefficient of Lift	Coefficient of Drag
-2	-0.00759	0.002910
0	0.00498	0.002733
2	0.0170	0.002924
4	0.0263	0.003505
6	0.0328	0.004525
8	0.0378	0.006377
10	0.0352	0.008546

Figure 42 shows the airfoil's relationship between lift coefficient and blade pitch. For comparison, the thin airfoil lifting line theory's relationship between lift coefficient and blade pitch is also shown. To remind the reader, that relationship is $C_l = 2\pi\alpha$, where α is in radians. A comparison between thin airfoil theory and the MSH hexacopter rotor

geometry for the 7% span section was shown to denote the performance differences due the vastly different airfoil geometry.

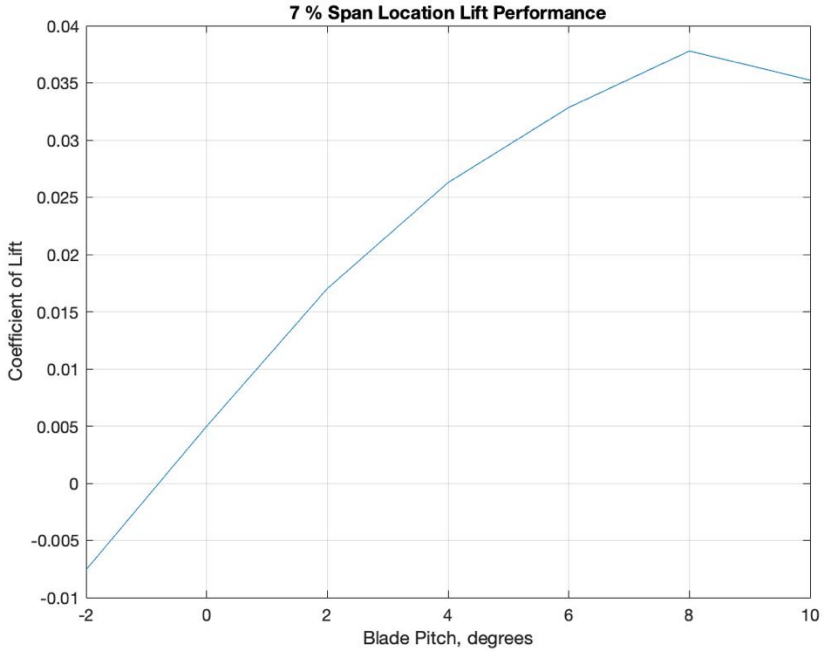

Figure 41: MSH Hexacopter 7% Span Location Cl vs. α

Figure 43 shows the relationship between lift coefficient and drag coefficient, also commonly referred to as the drag polar. A "C" like nature is expected for this type of plot. However, because the angle of attacks evaluated for were not equally done for the positive and negative range, the full "C" is not shown.

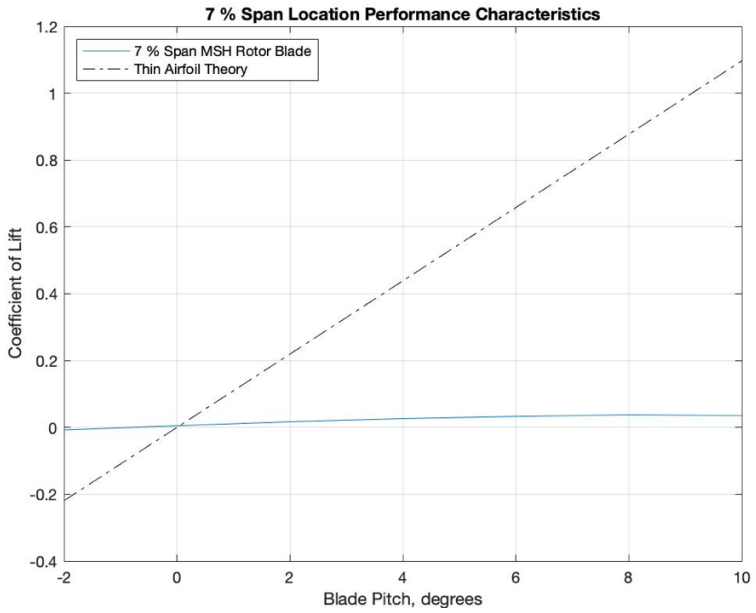

Figure 42: MSH Hexacopter 7% Span Location Cl vs. α. Thin Airfoil Lifting Line theory's relationship between Cl and α is shown for comparison.

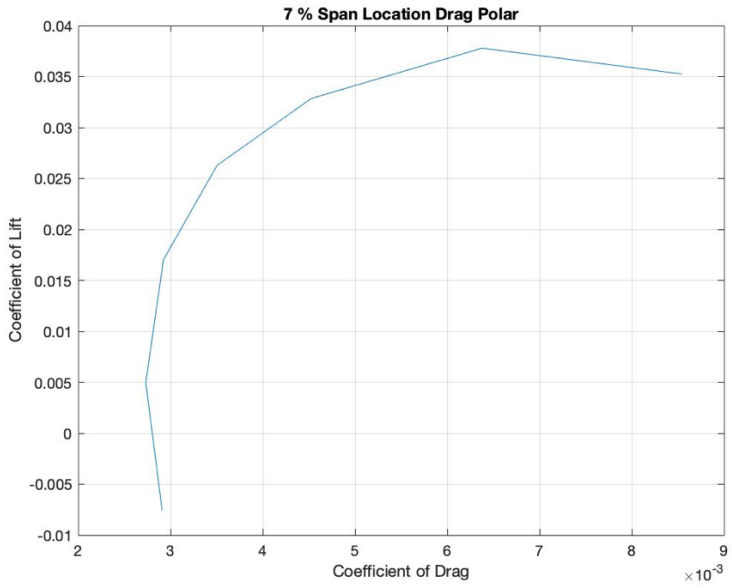

Figure 43: MSH Hexacopter 7% Span Location Drag Polar (Cl vs. Cd)

Figure 44 is the airfoil's lift to drag ratio as a function of blade pitch. This plot denotes a maximum Cl/Cd ratio occurring at four degrees of blade pitch.

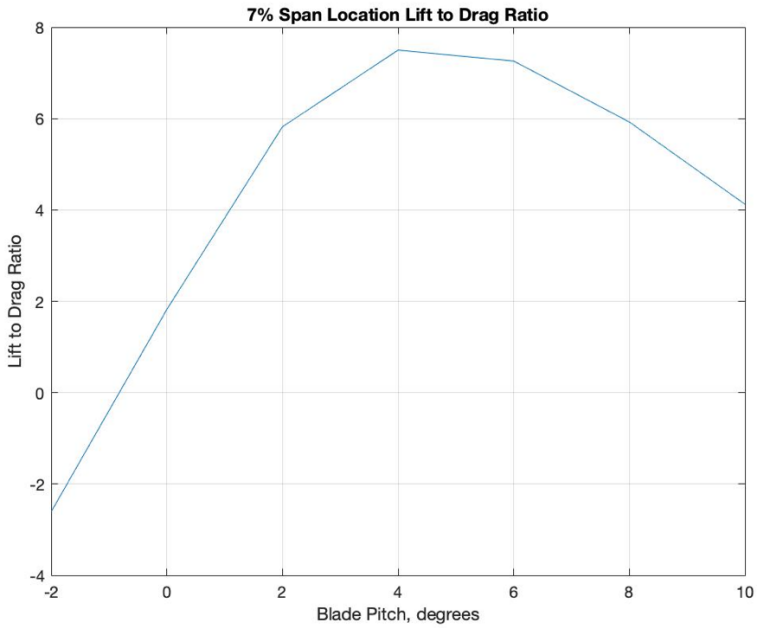

Figure 44: MSH Hexacopter 7% Span Location L/D vs α

Figure 45 is the coefficient of pressure evaluated at each non-dimensional x/c position along the top and bottom surface of the airfoil for two representative angles of attack. Shown on the plot are the Cp curves for the maximum Cl/Cd cases (i.e. four degrees) and the stall condition (i.e. 10 degrees). Both the top and bottom surfaces of the airfoil for each angle of attack are marked.

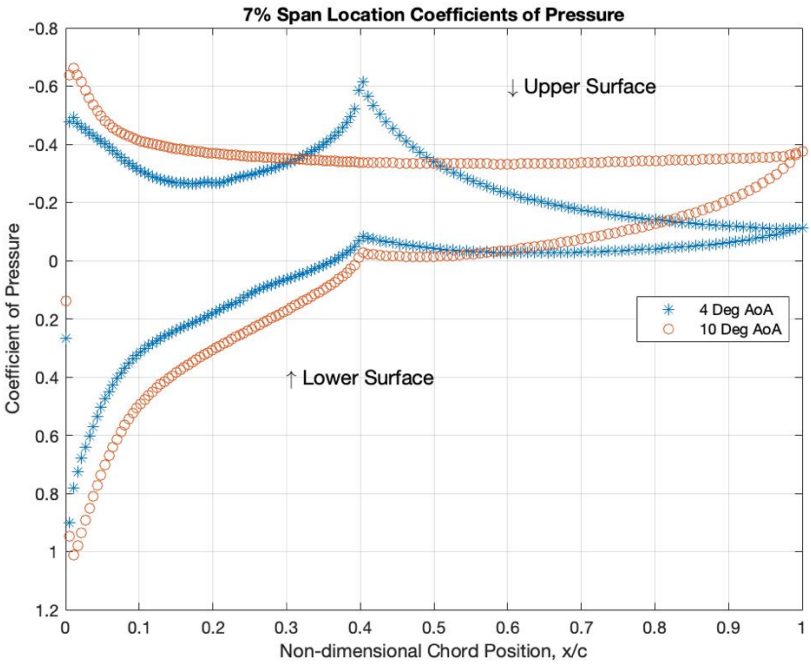

Figure 45: MSH Hexacopter 7% Span Coefficient of Pressure vs Chord for max Cl/Cd (4°) and stall (10°) angles of attack.

Figure 46 - Figure 50 show the static pressure contour, velocity magnitude contour, X-velocity magnitude contour, flow path line velocity magnitude, and flow path line X-velocity magnitude for the four degree angle of attack case, respectively. Figure 51 - Figure 55 are the same list of plots but for the 10 degree angle of attack case.

The four and 10 degree angle of attack cases are shown below because of their importance with respect to performance. The four degrees angle of attack figure set represent the maximum lift to drag ratio situation. The 10 degree angle of attack figure set represent the next angle analyzed after passing the maximum lift coefficient (and therefore the stall condition). The actual stall angle may be anywhere between eight and 10 degrees. The same analyses and plots were produced and analyzed for all of the

aforementioned angles of attack, however, only the four and 10 degree situation is included in this Thesis..

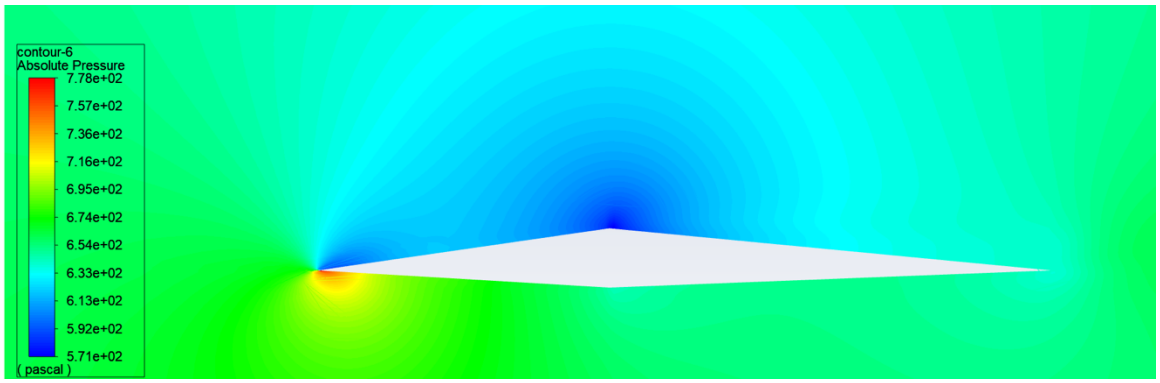

Figure 46: 4° angle of attack absolute pressure contour, pascals

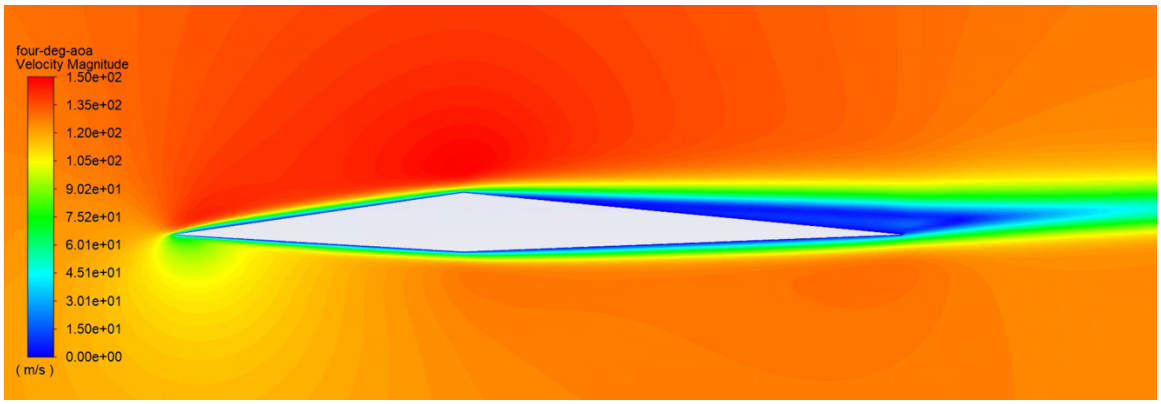

Figure 47: 4° angle of attack flow velocity magnitude, m/s

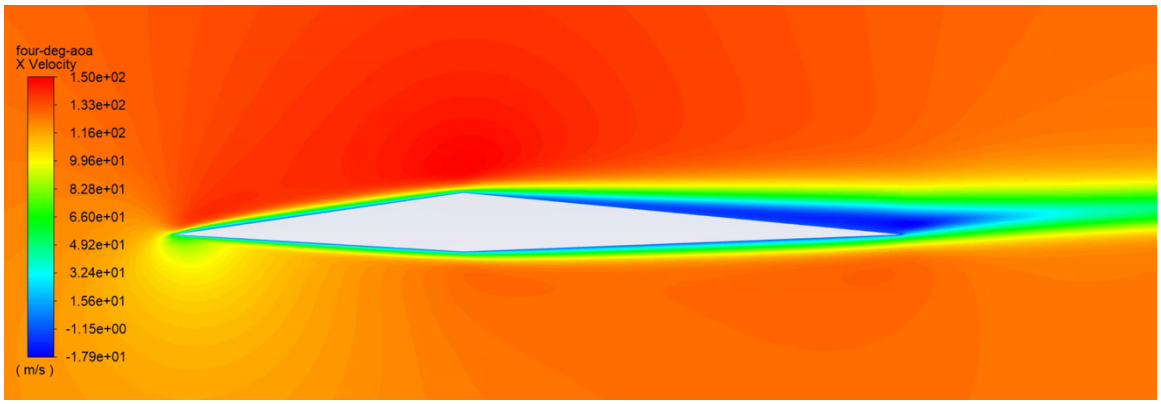

Figure 48: 4° angle of attack flow X-velocity magnitude, m/s

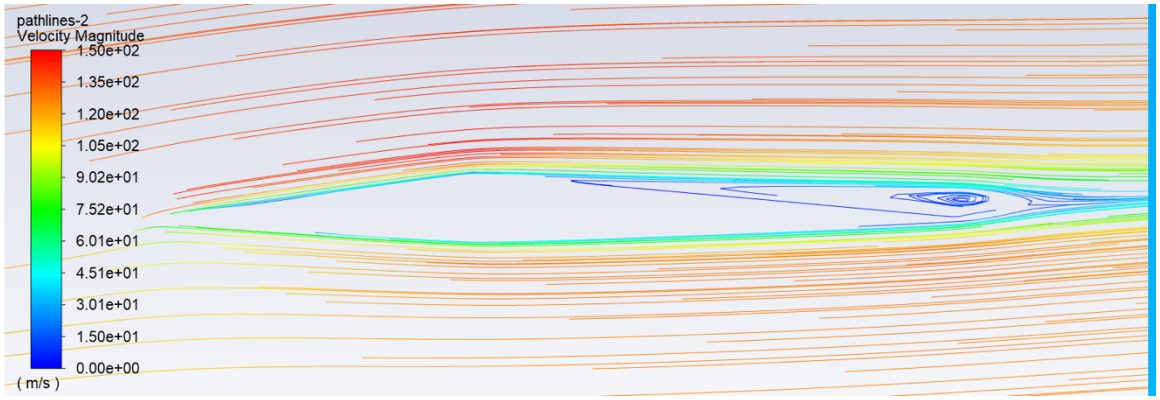

Figure 49: 4° angle of attack flow path line velocity magnitude, m/s

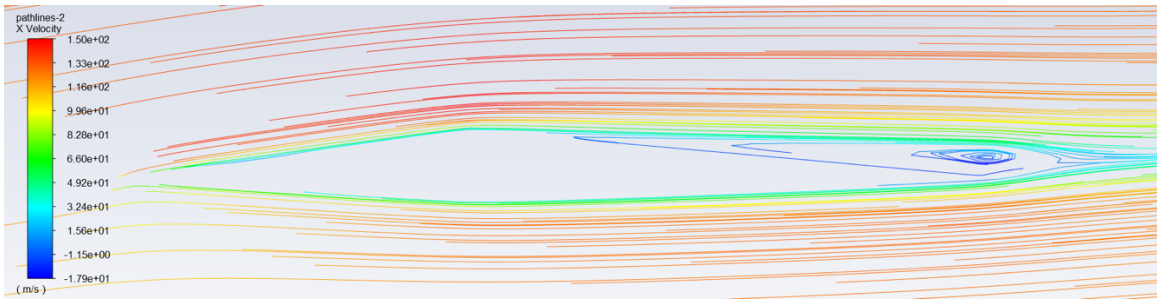

Figure 50: 4° angle of attack flow path line X-velocity magnitude, m/s

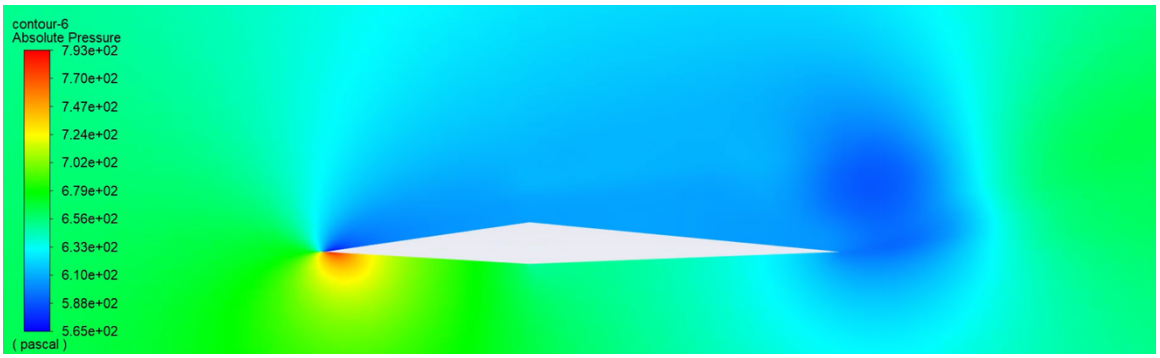

Figure 51: 10° angle of attack absolute pressure contour, pascals

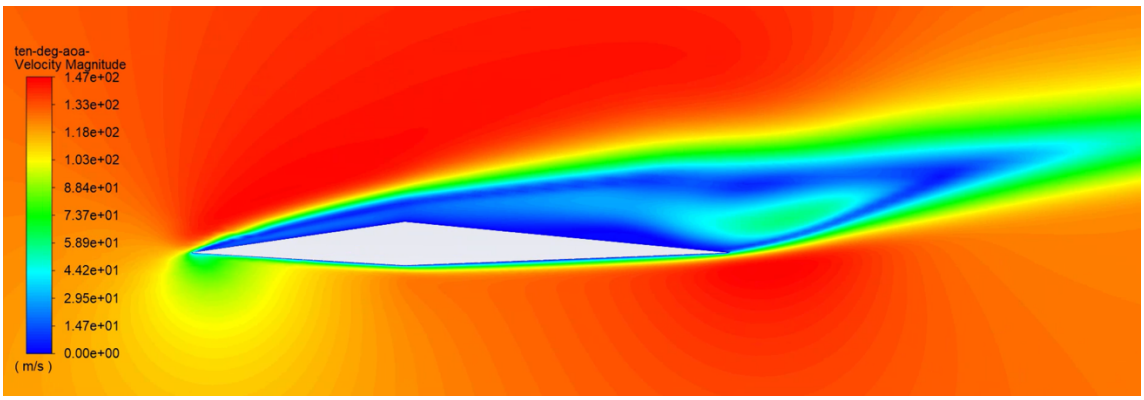

Figure 52: 10° angle of attack velocity magnitude, m/s

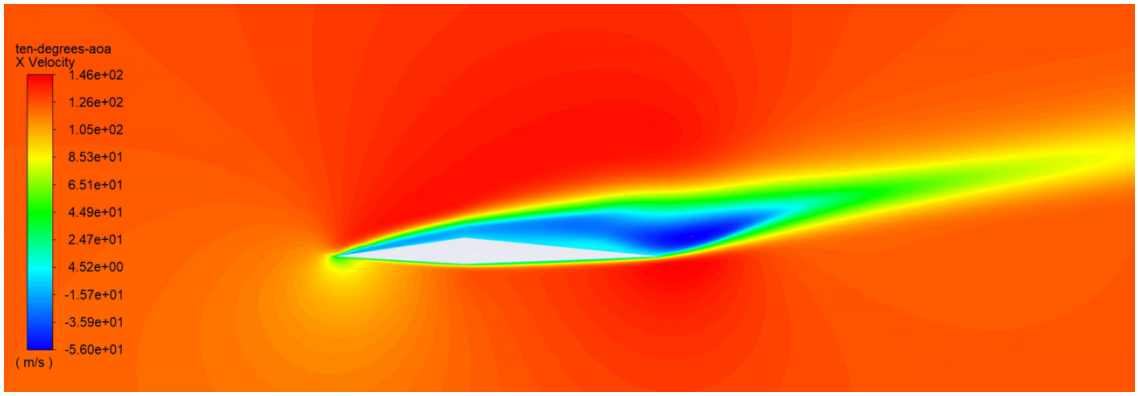

Figure 53: 10° angle of attack X-velocity magnitude, m/s

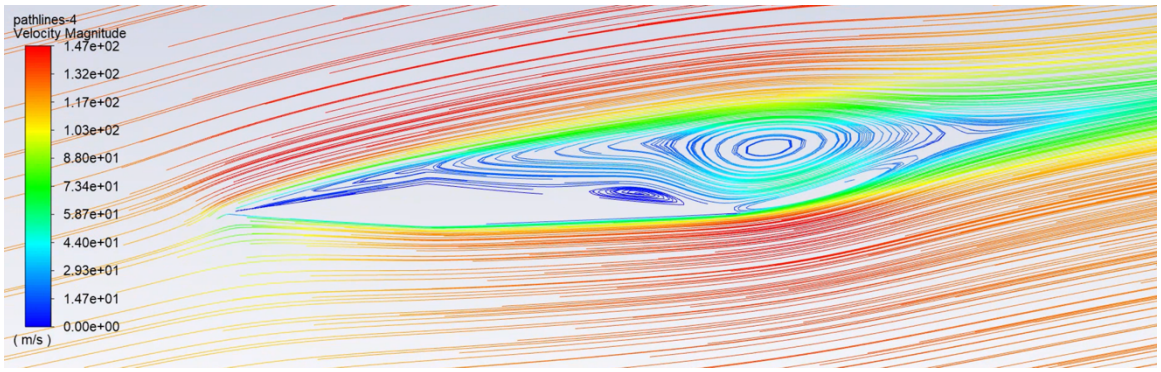

Figure 54: 10° angle of attack flow path line velocity magnitude, m/s

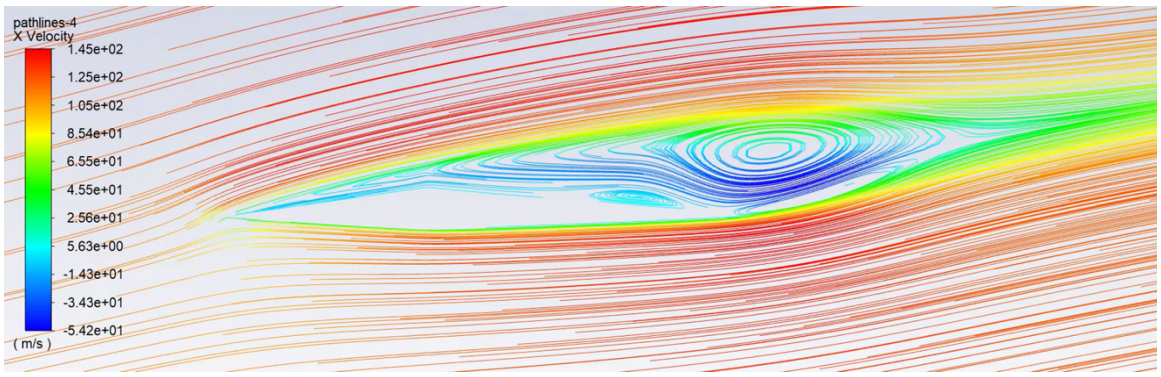

Figure 55: 10° angle of attack flow path line X-velocity magnitude, m/s

Chapter 6. Discussion and Analysis of Results

6.1 Discussion of the BEMT Data Comparison

The BEMT data sets presented in Chapter 5.1 show close matching between Leishman's data and that of the model produced. From the data points analyzed, the average percent error for each plot compared was calculated and is shown in Table 2. The absolute maximum average percent error was 7.77 % for the comparison between coefficient of power vs. blade pitch for the BEMT analysis conditions. The absolute minimum average percent difference was 2.11 % for the coefficient of thrust vs. coefficient of power comparison.

There are two known differences between Leishman's data and this model's data that have an unknown amounts of impact on the results produced. McCrink and Gregory (2015) discuss how important the quality of the 2D sectional airfoil performance data is for obtaining the most accurate BEMT output data possible. Therefore, the input data used in the BEMT model for evaluating each 2D airfoil section's performance is critical to the efficacy of the model's output. Leishman did not publish from what source or by what means he produced his 2D airfoil BEMT input data. Because one of the inputs to Leishman's model is unknown – and is of the most significance in the analysis of the data produced – it cannot be determined as to how significant this difference is in comparing the data produced. This source of difference could be attributed to the reason why the data does not match even more closely. However, due to the average percent error

difference being low in magnitude, the data trends and closely follows that of Leishman (2017), and the ranges plotted over being exactly the same, the BEMT model was considered of high enough accuracy and efficacy.

An additional difference in the data results produced can be attributed to the BEMT model's treatment of the 2D sectional airfoil performance data. The BEMT model produced evaluates the Re at each blade section, but when the performance data is retrieved using a MATLAB function for outputting the correct data set to use, the data set retrieved is that within the closest +/- 2,500 Reynolds number defined data set. This is not how a most accurate BEMT model should work. When the minimum and maximum rotor Re were calculated and imported to XFLR5 for sectional performance data generation, a step size of Re was needed as an input to the multi-threaded batch analysis. A step size of 5,000 was chosen and thus corresponded to the 37 data sets that were produced over the min-to-max Re range evaluated for.

The number of 2D airfoil performance data sets that are used with a BEMT model scales proportionally with the number of blade sections evaluated over. The BEMT model produced uses 70 blade elements, and therefore 70 unique data sets would be needed for most accurate analysis. However, only 37 data sets were used due to time limitations of this research project's timeline. Each data set needs to be exported from XFLR5, parsed and formatted so that it is easily compatible for import into MATLAB. Thus, performing this data preparation on 70 data sets is expensive in terms of time. The next iteration of the BEMT model will include a sufficient number of 2D airfoil data tables.

Figure 32 shows the relationship between local induced inflow and non-dimensional radial position. As the radial position increases, the local induced inflow increases because the local induced velocity is increasing. (Note that for this figure, Prandtl's loss factor model is not implemented as Leishman did not have a plot of such.) When the small angle approximation is assumed, the inflow value at each radial position can be divided by its respective non-dimensional radial position's value to yield the induced flow angle of attack in radians. As the inflow increases, the induced angle of attack increases. When Prandtl's loss factor model is implemented in the inflow calculation, the inflow increases exponentially in the last 15-20% of the span. The sharp increase in inflow causes a proportional increase in induced angle of attack, which lowers the effective angle of attack and drives the thrust production nearest to the rotor tip region to zero.

Figure 33 shows the relationship between thrust coefficient and power coefficient. The thrust produced and power required for a given rotor situation is related through an additional velocity term in the equation's evaluation (refer to Equations (15) and (18) for reference). Power is proportional to velocity cubed and thrust is proportional to velocity squared. Moreover, a component of the coefficient of power is calculated using the derivative of thrust coefficient with respect to radial position. Therefore, the relationship of power and thrust is dependent on each other in two ways. When these two factors are considered, it is a reasonable result to see that there is a quadratic-like proportionality between thrust and power. Figure 33 denotes this quadratic-like relationship.

Figure 34 shows the relationship between power coefficient and blade pitch. A component of the power coefficient is a function of the local drag coefficient of each blade section. Thus, as blade pitch increases, so does drag coefficient. The drag increases because the blade section's profile geometry increased, and thus corresponded to an increase in profile drag. The quadratic-like relationship between power coefficient and blade pitch is expected as the drag increases quadratically as the blade pitch increases.

Figure 35 shows the thrust gradient along the rotor's span. In other words, the plot shows to what extent each portion of the blade's span location contributes to the overall thrust force produced. The thrust is expected to be most heavily concentrated towards the outer 50% of the rotor as the velocity – and thus dynamic pressure – is the largest. An increase in dynamic pressures corresponds to an increase in lift (or in this rotorcraft case, thrust). Moreover, as the Re and Mach number increases along the rotor span, the lift coefficient is positively impacted. Higher Re is known to help increase performance of airfoils. Moreover, the compressibility effects at Mach numbers greater than 0.3 affect the lift coefficient positively. These two factors contribute to the higher production of lift (or rather thrust) in the outer section of the rotor span.

Figure 35 shows the thrust gradient with both Prandtl's tip loss and root loss factor implemented. The loss factors are present on the calculation of inflow, however, because the inflow at each radial station affects the effective blade angle of attack (and therefore the coefficient of lift), the shape and magnitude of the thrust gradient is affected. Figure 21 shows the impact the Prandtl loss factor has on both the root and tip regions. The tip region of the rotor is most significantly impacted (compared to that of the

root). This impact is most noticeable in the $0.9 < r < 1$ region of the thrust gradient as the differential thrust coefficient is driven to zero at the tip. Physically, it makes sense that no thrust is produced at the tip because there is no physical body in which the lifting force can be applied to as the rotor blade is finite. Moreover, the aspect ratio of the blade also plays a significant role in the production of thrust and its distribution along the span.

Figure 36 shows the relationship between local coefficient of lift and non-dimensional radial position. (Note that for this figure, Prandtl's loss factor model is not implemented as Leishman did not have a plot of such.) Previously discussed, the inflow at each radial station impacts the effective blade angle of attack. When Prandtl's loss factor model is implemented, the angle of attack the blade section perceives is driven towards zero, which corresponds to very low lift coefficients (and sometimes even a lift coefficient of zero). However, because that model is not implemented in the data shown in Figure 36, the lift coefficient increases in a quadratic-like nature from rotor root to tip because the inflow increases in the same manner.

6.2 Discussion of the BEMT Reynolds Number Dependent Performance Comparison

The BEMT analysis performed in Chapter 5.2 demonstrates how significantly Reynolds number affects rotor performance. The thrust generated and power required plots presented in Figure 37 - Figure 40 show that decreasing Re leads to degraded performance. There is at minimum a difference of at least an order of magnitude between the thrust generated and power required for the comparison situations. The representative

situation shown demonstrates how significantly the ULRE domain affects performance and why a need for further researching this area is needed.

6.3 Discussion of the ANSYS Fluent CFD Results

Due to the nature of this Thesis' timeline, only the 7% span section was analyzed with ANSYS Fluent. The original project timeline intended to analyze all of the blade section geometries at all of the angles of attack aforementioned. However, the amount of time needed for learning ANSYS Fluent was severely underestimated, and unfortunately only the 7% span was analyzed even though the geometries and Solidworks models for each of the other sections were designed. Moreover, when it was realized that only one blade section was going to be able to be analyzed with the constrained timeline, the 75-100% section could have been chosen for analysis compared to the 7% section, as that geometry was of most relevance with respect to aerodynamic performance and research interest. The 7% span location of the MSH hexacopter rotor blade was designed for structural rigidity and not aerodynamic efficiency. A spar of sufficient strength is needed to connect the rotor hub and rotor blade, thus the thickness of the 7% span section is much greater than any of the other defined blade section geometries. A polygonal-like linear section based airfoil was shown to not perform well in ULRE conditions. In retrospect, the 75-100% span geometry should have been chosen for analysis and it is expected to be perform significantly better compared to the 7% span location.

Table 3 shows the 7% span location performance characteristics for a sweep of angles of attack. Similar to conventional airfoil performance, the lift and drag coefficients increase with increasing angle of attack. Moreover, lift coefficient is usually an order of magnitude greater than drag coefficient, which is shown in these results, too.

Near eight degrees is when a reduction in lift coefficient is observed. This reduction in performance is inferred to be a result of dynamic airfoil stall. The percent difference in drag coefficient between eight and 10 degrees is over 25%. Assuming eight degrees is the critical angle of attack (i.e. the stall angle), the increase in drag is due to flow separation and a reduction of pressure around the airfoil. This is most prevalently shown by Figure 45, which plots the coefficients of pressure along the chord length for the top and bottom airfoil surface for each angle of attack.

Figure 41 plots the coefficient of lift as a function of angle of attack. It is seen that the lift coefficient increases in a linear-like manner with angle of attack. However, the average slope of this linear-like line is very small in magnitude. The lift coefficient relationship with blade pitch according to thin airfoil theory is shown in Figure 42 for comparison. This aforementioned relationship is $C_l = 2\pi\alpha$, where α is in radians. Although most of the MSH hexacopter rotor blade is flat plate like, the 7% span location is very thick relative to a flat plate geometry and does not have a geometry that satisfies using thin airfoil theory due to its sharp, polygonal nature. Thus, it was not expected or proven to behave in a similar manner in accordance to thin airfoil theory.

Figure 43 shows the airfoil section's drag polar. The shape of the drag polar is consistent with that which was expected for airfoils. When lift coefficient is plotted with

respect to drag coefficient, it is expected that a curve that depicts a “C” is produced. Figure 43 shows this relationship correctly. However, because the angle of attack sweep was not equally assessed for the negative angle of attack range, the full “C” shape of the drag polar was not produced by the data.

Figure 44 shows the lift to drag ratio as a function of angle of attack. From this plot, it can be shown that the max L/D condition occurs for an angle of attack of four degrees. However, because this airfoil section is that of the most inboard position on the MSH hexacopter rotor, its contribution to the thrust produced is essentially negligible and its max L/D contribution is not significant.

Figure 45 shows the coefficient of pressure for both the top and bottom sides of the airfoil at the angles of attack that correspond to the maximum Cl/Cd and stall conditions. Unlike conventional airfoils that have the coefficient of pressure plot demonstrate a continuous pressure distribution, the airfoil analyzed shows a pressure discontinuity. Moreover, the Cp curves for the angles of attack do not “meet” at a common point along the leading edge like conventional airfoils do (where the flow stagnates). Due to the sharp nature of the airfoil leading edge, the flow separation point significantly impacts the coefficient of pressure value along the leading edge.

Figure 46 shows the absolute pressure contour of the four degrees angle of attack flow analysis. The top side of the airfoil is the “suction side,” which corresponds to low pressure. The bottom side of the airfoil is the “pressure surface,” which corresponds to high pressure. Together, this pressure imbalance is what creates a net force on the airfoil section and thus a lifting force (or rather thrust force in the context of rotorcraft).

Moreover, the same analysis can be said for that of Figure 51, which is the absolute pressure distribution for the 10 degree angle of attack flow analysis. However, this absolute pressure distribution is much different for this case. The low pressure region extends from the leading edge to the trailing edge. The four degree angle of attack situation only had a low pressure region corresponding to approximately the first linear section of the top side of the airfoil. Figure 51's large low pressure region corresponds to a much greater boundary layer thickness with slow moving flow, and even reverse flow at some points. The stagnation point on polygonal, sharp leading edge airfoils is not on the nose, but on the lower surface near the leading edge. It is evident from the velocity magnitude contours and path line magnitude plots that this is true.

Figure 47 shows the velocity magnitude contour for the four degree angle of attack flow analysis. It can be seen more clearly from this figure where the fixed separation point is**.** The sharp leading edge of the airfoil initiates flow separation at this fixed location – which is a phenomena that is widely different compared to convention airfoils whose separation point can vary in space.

The fixed separation point at the leading edge causes the laminar flow to trip early along the airfoil's surface and result in the flow being subcritical (as a reminder to the reader, subcritical is defined as being if the streamline shape of the boundary layer is laminar for a range of angles of attack). The separated shear layers then gain momentum from the free stream flow and would lead to transition. However, because a laminar flow model is assumed, and justified by the literature, transition to turbulence doesn't occur. Moreover, turbulent flow reattachment does not occur after laminar separation, as shown

by Figure 47. This is because the laminar boundary layer in the ULRE domain is not significantly affected by minute disturbances and their resulting amplification through the flow field. The slow moving and reverse flow region in the 10 degree angle of attack case is significantly closer to the airfoil's leading edge compared to that of the four degree angle of attack case.

Looking closely upon the airfoil's top side towards the trailing edge boundary layer region in Figure 48, it can be seen that there is a region of low x-velocity, zero x-velocity, and negative x-velocity flow which corresponds to a high adverse pressure gradient. The low and reverse velocity flow region begins after the max thickness location point. This phenomena can be more easily analyzed with Figure 49 and Figure 50 which show the flow path line velocity and path line x-velocity magnitude, respectively. The path lines show that the flow is curling up upon itself and forming vortices, which is a phenomena that can, too, occur in unsteady laminar flow.

Taking a close look at both Figure 47 and Figure 48, the flow closest to the airfoil has a very thin region of flow corresponding to approximately zero velocity. This aspect of the flow analysis is expected as a viscous airfoil boundary was assumed within the CFD settings. The flow touching the airfoil must have zero velocity due to viscous forces.

Figure 52 and Figure 53 show the velocity magnitude and X-velocity magnitude contours for the 10 degree angle of attack case. The boundary layer is shown to be much thicker in this case. Moreover, the region of slow moving and even reverse flow is substantially larger than the four degree angle of attack. This is expected as there isn't a strong adverse pressure gradient present (as demonstrated by Figure 51) and the flow

field indicates that stall has occurred. Figure 54 and Figure 55 demonstrate the path line velocity and path line X-velocity magnitude for the 10 degree angle of attack analysis. A "rolling up" of the path lines is quite evident within the low- and negative-X-velocity regions of the flow field and indicate the presence of vortices.

Chapter 7. Conclusions, Methods of Improvement, Future Work, and Applications of Research

7.1 Conclusions

A significant amount of knowledge was learned as a result of this research Thesis' work. Most notably is that of equations governing rotorcraft flight, its metrics for performance, and BEMT modeling of rotorcraft performance. Moreover, an elementary introduction to CFD helped better discern the complexity of the field and the difficulty in obtaining accurate results. Additionally, a wide amount of exposure to the ultra-low Reynolds number flow regime and optimized rotors and airfoils for this condition was obtained as a result of the literature review portion of this project and experiments performed.

The BEMT code developed was determined to be of sufficient accuracy and efficacy when compared to a reputable external source of data. For the five plots used in the comparison of model's data, the absolute average percent error difference was less than 7.77% at the worst, and 2.11% at best for the data compared. Additionally, the comparison between Re = 100,000 and Re = 10,000 analyses demonstrates how significantly rotor performance degrades as Re decreases.

The 7% span location of the optimized MSH Hexacopter rotor was shown to not be of high aerodynamic performance. The maximum attainable lift coefficient was 0.0378 at eight degrees of blade pitch and the maximum lift to drag ratio was 7.5 for four degrees of blade pitch. Low performance was expected as the 7% span location airfoil

geometry was designed for structural rigidity and support, and not aerodynamic performance.

7.2 Methods of Improvement

Many aspects of this research thesis could be improved upon for more accurate results. To start, the BEMT data comparison could utilize more data points from Leishman's figures. Data points were extracted by hand – which is a method that is prone to human error – and limited the data extraction to only well-defined data points that fit the plot grid. A plot digitizer could produce X-Y data points of each plot used for comparison, and a more accurate percent difference comparison could be performed. Additionally, the BEMT code will be modified for use with the correct amount of data sets for evaluating each blade elements' performance coefficients for the correct Re.

On the ANSYS Fluent CFD portion of this research Thesis, there are numerous improvements that could be made. An alternative approach to producing a structured mesh for a polygonal airfoil will be evaluated. Structured meshes work well for conventional rounded airfoils with a C-mesh architecture. However, using a structured mesh for the polygonal airfoil used was not easily implementable. The current mesh used in the CFD analysis was of unknown quality and could certainly be further refined. Moreover, a mesh independence study could be performed.

Additionally, a CFD analysis for each of the defined rotor span sections could be performed so that performance for each geometry could be determined.

7.3 Future work

Alongside the aforementioned computational analysis work to be performed is a means of physically testing the rotor of interest analyzed in this Thesis. Procuring physical, scaled models of the ROAMX airfoil and MSH rotor geometry could be pursued for experimental testing. Moreover, the physical testing would allow for comparison of computational and experimental data and validation of the model developed. 3D printing would likely be used to manufacture the rotor as its geometry is jagged, unconventional, varies in the spanwise and chordwise direction, and would be difficult to produce with normal manufacturing methods. Wind tunnels and reduced atmospheric pressure testing in a vacuum chamber at The Ohio State University's Aerospace Research Center (ARC) would prove useful in ensuring model validity, accuracy, and efficacy.

Existing hardware at the ARC called "the rotor rig" could be used for recording rotor performance data. However, the hardware currently in place will be reviewed for if they are of sufficient accuracy, range, and resolution needed for this project's analysis. Currently, the rotor rig consists of a brushless DC motor, force and torque load cells, an electronic speed controller, a data acquisition system, a servo motor for changing blade pitch, and a Hall effect sensor for rotational speed feedback. Although the atmospheric conditions used in ARC wind tunnel testing will be that of Earth's, the Re could be matched for Martian atmospheric conditions and prove to be an effective way of producing Earth-based, Martian-atmospheric-analogous results. Accurate and precise

measurement of Re will be a primary area of concern during physical testing and would be verified with highly sensitive atmospheric and wind speed measuring hardware.

Moreover, a systems level design approach (SLDA) will be used for considering how a vertical take-off and landing (VTOL) fixed-winged drone for Mars exploration would affect the propulsion needs of the rotor performance model, without focusing on physically developing such a VTOL drone.

This work would not focus on the development of the vehicle's controls system, sensor packages, or data collection system. However, their affects will be kept in mind throughout the design process. Additionally, the following mission constraints would be kept in mind while researching and producing results: Mars regolith and dust posing issues for optimal vehicle performance; a varying atmospheric density on Mars; changing seasonal affects; dust storms; and the average amount of sunlight received on the surface by the Sun.

7.4 Applications of Research

Some future potential applications of this research project include a swarm of drones for canvasing entire regions of Mars; astronaut operated flight from Mars orbit or the surface; or data sharing with a Mars rover for safer and more effective traversing by means of optimal path planning.

Bibliography

Air and Space (n.d.). *Exploring the Planets | National Air and Space Museum*. [online] airandspace.si.edu. Available at: https://airandspace.si.edu/exhibitions/exploring-the-planets/online/solar-system/mars/ [Accessed 24 Mar. 2021].

Anyoji, M., Nose, K., Ida, S., Numata, D., Nagai, H. and Asai, K. (2010). Low Reynolds Number Airfoil Testing in a Mars Wind Tunnel. *40th Fluid Dynamics Conference and Exhibit*. [online] Available at: https://arc.aiaa.org/doi/abs/10.2514/6.2010-4627 [Accessed 27 Mar. 2021].

Argus, F.J., Ament, G.A. and Koning, W.J.F. (2020). The Influence of Laminar-Turbulent Transition on Rotor Performance at Low Reynolnds. In: . [online] VFS Aeromechanics for Advanced Vertical Flight Technical Meeting. Vertical Flight Society. Available at: https://rotorcraft.arc.nasa.gov/Publications/files/Finbar_Argus_TVF_2020-01-20.pdf

Carmichael, B.H. (1981). Low Reynolds Number Airfoil Survey. , [online] 1. Available at: https://ntrs.nasa.gov/api/citations/19820006186/downloads/19820006186.pdf [Accessed 27 Mar. 2021].

Coustenis, A. (n.d.). *The origin and evolution of Titan's atmosphere*. [online] Paris-Meudon Observatory, France: European Space Agency. Available at: https://sci.esa.int/documents/35171/36506/1567259121123-1-ESLAB12_Day3-Coustenis.pdf

Deperrois, A. (2013). *XFLR5*. [online] Xflr5.tech. Available at: http://www.xflr5.tech/xflr5.htm

Drela, M. (2013). *XFOIL Subsonic Airfoil Development System*. [online] mit.edu. Available at: http://web.mit.edu/drela/Public/web/xfoil/

Harris, F.D. (2020). *Model Rotor Hover Performance at Low Reynolds Numbers*. [online] *NASA Ames Aeromechanics Branch Publications*, Moffet Field, California, USA: NASA Ames, pp.1–61. Available at: https://rotorcraft.arc.nasa.gov/Publications/files/Harris%20CR-20205001147_Final.pdf

Helicopters & Aircrafts (n.d.). Reynolds Number and Mach Number Effects. [online] Helicopters & Aircrafts. Available at: http://heli-air.net/2016/02/13/reynolds-number-and-mach-number-effects/ [Accessed 12 Apr. 2021].

J Gordon Leishman (2017). *Principles of Helicopter Aerodynamics*. 2nd ed. Cambridge, United Kingdom: Cambridge University Press, pp.1–167.

Johnson, W., Withrow-Maser, S., Young, L., Malpica, C., Koning, W., Kuang, W., Fehler, M., Tuano, A., Chan, A., Datta, A., Chi, C., Lumba, R., Escobar, D., Balaram, J., Tzanetos, T. and Fjaer Grip, H. (2020). *Mars Science Helicopter Conceptual Design*. [online] NASA. Available at: https://rotorcraft.arc.nasa.gov/Publications/files/MSH_WJohnson_TM2020rev.pdf

Knight, M. and Hefner, R.A. (1937). Static Thrust Analysis of the Lifting Airscrew. [online] pp.1–61. Available at: http://digital.library.unt.edu/ark:/67531/metadc54408/m2/1/high_res_d/19930081433.pdf

Koffeman, H. (1992). *The Reynolds Number*. [online] Available at: www.aerodrag.com/Articles/ReynoldsNumber.htm

Koning, W. (2021). *Rotor Performance Optimization*. [Email, Microsoft Teams Video Chat].

Koning, W.J., Romander, E.A. and Johnson, W. (2020). Optimization of Low Reynolds Number Airfoils for Martian Rotor Applications Using an Evolutionary Algorithm. *AIAA SciTech 2020 Forum*.

Koning, W.J.F., Johnson, W. and Allan, B.G. (2018). Generation of Mars Helicopter Rotor Model for Comprehensive Analyses. In: . [online] AHS Specialists' Conference on Aeromechanics for Transformative Vertical Flight. American Helicopter Society. Available at: https://ntrs.nasa.gov/api/citations/20180008645/downloads/20180008645.pdf

Koning, W.J.F., Johnson, W. and Grip, H.F. (2019). Improved Mars Helicopter Aerodynamic Rotor Model for Comprehensive Analyses. *AIAA Journal*, 57(9), pp.3969–3979.

Koning, W.J.F., Romander, E.A. and Johnson, W. (2018). Low Reynolds Number Airfoil Evaluation for the Mars Helicopter Rotor. AHS International 74th Annual Forum and Technology Display. American Helicopter Society.

Koning, W.J.F., Romander, E.A. and Johnson, W. (2019). Performance Optimization of Plate Airfoils for Martian Rotor Applications Using a Genetic Algorithm. European Rotorcraft Forum.

McCrink, M. and Gregory, J. (2015). Blade Element Momentum Modeling of Low-Re Small UAS Electric Propulsion Systems. In: *AIAA Applied Aerodynamics Conference*. [online] AIAA. Available at: https://arc.aiaa.org/doi/10.2514/6.2015-3296

McMasters, J.H. and Hendersen, M.L. (1979). Low-Speed Single-Element Airfoil Synthesis. In: *Technical Soaring*. [online] NASA-SSA Third International Symposium on the Science and Technology of Low-Speed and Motorless Flight. Hampton, Virginia, USA: NASA Langley Research Center, pp.1–21. Available at: https://journals.sfu.ca/ts/index.php/ts/article/view/989/943 [Accessed 27 Mar. 2021].

Mueller, T.J. and Reshotko, E. (1985). *Low Reynolds Number Vehicles*. [online] . Available at: https://www.sto.nato.int/publications/AGARD/AGARD-AG-288/AGARD-AG-288.pdf

NASA (2019a). *Driving Distances on Mars and the Moon*. [online] NASA's Mars Exploration Program. Available at: https://mars.nasa.gov/resources/6471/driving-distances-on-mars-and-the-moon/.

NASA (n.d.). *Rover Wheels*. [online] mars.nasa.gov. Available at: https://mars.nasa.gov/mars2020/spacecraft/rover/wheels/

NASA (2019b). *Wheels | Rover – NASA's Mars Exploration Program*. [online] NASA's Mars Exploration Program. Available at: https://mars.nasa.gov/msl/spacecraft/rover/wheels/

NASA (n.d.). *Where is Curiosity? Location Map*. [online] NASA's Mars Exploration Program. Available at: https://mars.nasa.gov/msl/mission/where-is-the-rover/ [Accessed 3 Mar. 2021].

NASA - Mars (2021). *NASA to Host Briefing to Preview First Mars Helicopter Flights*. [online] NASA's Mars Exploration Program. Available at: https://mars.nasa.gov/news/8891/nasa-to-host-briefing-to-preview-first-mars-helicopter-flights/ [Accessed 24 Mar. 2021].

NASA Ingenuity (n.d.). *Mars Helicopter*. [online] NASA. Available at: https://mars.nasa.gov/technology/helicopter/

Segall, M. (n.d.). *NASA Ames ROAMX*. [online] rotorcraft.arc.nasa.gov. Available at: https://rotorcraft.arc.nasa.gov/Research/Programs/roamx.html [Accessed 24 Mar. 2021].

Vyriotes, P. (2012). *PropGen Design and Analysis*. [online] Available at: http://www.propgen.com/martian_aircraft.htm

Weidner, S. (n.d.). *FLUENT Learning Modules - SimCafe - Dashboard*. [online] confluence.cornell.edu. Available at: https://confluence.cornell.edu/display/SIMULATION/FLUENT+Learning+Modules

WennersHerron, A. (2019). *Lasting work: Penn State engineers help NASA go to Titan for mission "Dragonfly" | Penn State University*. [online] news.psu.edu. Available at: https://news.psu.edu/story/589159/2019/09/20/research/lasting-work-penn-state-engineers-help-nasa-go-titan-mission

Williams, M. (2015). *Mars compared to Earth*. [online] phys.org. Available at: https://phys.org/news/2015-12-mars-earth.html

Winarto, H. (2004). *BEMT Algorithm for the Prediction of the Performance of Arbitrary Propellers*. [Research Report] Available at: https://ftp.unpad.ac.id/orari/library/library-non-ict/aero/docs/CoEAL%20report%20BEMT.pdf

Appendix A. BEMT Code Developed with MATLAB

Main BEMT Analysis Code:

```
% Written by Isaac Bensignor
% BEMT analysis code is in support of the Undergraduate Research Thesis
% and the Master's Thesis research work of the BS/MS Program

%% Pre- Analysis Data Set up
% The rotor data shown here is for that of the data used for comparing
to Leishman's plots

%Blade Setup Data
Nb = 5; % Number of blades on the propeller
chord = 0.0508; %Chord length, meters
rTip = 1.524/2; % Distance to the blade tip from the hub, meters
rHubPercentage = 0.167; % Percentage of rotor radius that is the hub
cut out, percent
rHub = rHubPercentage * rTip; %Distance from the axis to the hub,
Meters,
sigmaConst = (Nb * chord * rTip) ./ (pi .* rTip^2); % Rotor solidity,
unitless
diskArea = pi * rTip^2; % Disk area, m^2

% Constant Multipliers
rtd = 180/pi; % radians to degrees conversion
dtr = pi/180; % degrees to radians conversion

% Atmospheric + Planetary data
rho = 1.225; % Assumed density of the atmosphere, kg/m^3
pressure =  101325; %Assumed pressure of the atmosphere, pascals
temperature = 288.15; %Assumed temperature of the atmosphere, Kelvin
gamma = 1.4; % Ratio of specific heats for air, unitless
rGas = 287.057; % Gas constant of air, J/kg*k
soundSpeed = sqrt(gamma * rGas * temperature); %Speed of sound, m/s
viscosity = 1.789e-5; % Pascal * Seconds
gravity = 9.81; %m/s^2

%% Computational Analysis Conditions - AoA and RPM Sweep Setup
RPMSweepVec = [200 400 600 800 1000]; %Sweep of RPM values to evaluate
                                      over
alphaSweepVec = [2 3 4 5 6 7 8 8.2 8.4 8.6 8.8 9 10]; %Sweep of angle
of attack values to evaluate over

% The length of the data used for evaluating the 2d Sectional performance
```

```
% characteristics must be known apriori.
numSec = 70; %all data has 70 rows and the number of blade section
scales with the number of data rows

%The following line creates a sinusoidal distribution of points from -1
to 1. The line after then sets the range of that data to be within root
hub cut out to tip radius range.
sinusoidalDist = sin(linspace(asin(-0.999), asin(0.999), numSec));
nonDimR =  (sinusoidalDist + 1) ./2  .* (1-rHubPercentage) +
rHubPercentage; %

%% BEMT AoA and RPM Sweep
for i = 1: length(alphaSweepVec) %Blade Pitch loop
    for j = 1: length(RPMSweepVec) %RPM loop

        % Pull the corresponding RPM and blade pitch values for each
          nested loop iteration
        alphaBlade = alphaSweepVec(i);
        RPM = RPMSweepVec(j); % RPM, rotations per minute of the rotor
        omega =  RPM * pi/30; %Rad/s, rotation rate of the rotor blade

        %Evaluate the Re and Mach per Blade Section
        %Assume the small angle approximation (i.e. Assume Ut >>Up,
         therefore U=Ut=omega*r)
        seenVelocity = omega .* nonDimR .* rTip;
        machPerBladeSec = seenVelocity./soundSpeed;

        %Calculate and store the tip mach number for each RPM
        tipMach(j) = seenVelocity(end)/soundSpeed;
        REPerBladeSec = rho .* seenVelocity .* chord ./viscosity;

       % For each blade element, determine the correct RE data set to
       % use, the inflow, interpolate the correct sectional performance
       % characteristics to use for the resulting effective angle of
       % attack, apply a compressibility correction to the lift and
       % drag coefficients,and the contribution to the thrust gradient
        for k = 1: numSec
            data2DPerSec{k,1} =
                  WideCorrectAirfoilDataforLeishman(REPerBladeSec(k));
            workingData = data2DPerSec{k,1};
            [deltaAngle indexToUse] = min(abs(workingData(:,1) –
                                                  alphaBlade));
            section2dDataAlphaVec = workingData(:,1);
            section2dDataClVec = workingData(:,2);
            section2dDataCdVec = workingData(:,3);
            perSecAlphaRad(k) = workingData(indexToUse,1) * dtr;
            perSecCl(k) = workingData(indexToUse,2);
            perSecCd(k) = workingData(indexToUse,3);
            perSecCla(k) = perSecCl(k) ./ perSecAlphaRad(k);

            % Calculation of Inflow, the Prandtl loss factor model
            % value,and the error between iterations of the inflow
            % calculation
            [lamda(k), F(k), error(k)] = lam_calc_hover(perSecCla(k),
```

```
                sigmaConst, perSecAlphaRad(k), nonDimR(k), Nb);

    %The following two lines can be used instead of the
    % proceeding one if the operator would like to asses the
    % BEMT model without using Prandtl's root and tip loss
    % factor model

    %  lamdaSecNoPTLF(k) = (sigmaConst .*  perSecCla(k) ./ 16)
                    .* (sqrt(1+(32./(perSecCla(k) .*
                    sigmaConst)) .* perSecAlphaRad(k) .*
                    nonDimR(k))-1);
    % lamda(k) = lamdaSecNoPTLF(k);

    % Determine the inflow angle in radians and calculate the
    % effective angle of attack in radians.Assume the small
    % angle approximation

    inflowAngle(k) = lamda(k) ./ nonDimR(k);
    effectiveSectionalAlphaRad(k) = perSecAlphaRad(k) -
                                    inflowAngle(k);

    %interpolate the data from the respective data set for
    %determining the correct Cl, Cd and Clalpha to use for each
    %blade element. Apply the compressibility correction of the
    %lift curve slope and drag coefficients.
    [interpolatedCl, interpolatedCla, interpolatedCd] =
                geometryPerformanceInterpolationOfBatchData(
                section2dDataClVec,section2dDataCdVec,effective
                SectionalAlphaRad(k),section2dDataAlphaVec.*dtr
                );
    perSecClaMachCorrection(k) = interpolatedCla ./ sqrt(1 -
                                        machPerBladeSec(k).^2);
    perSecCdMachCorrection(k) = interpolatedCd ./ sqrt(1 -
                                        machPerBladeSec(k).^2);

      % Thrust gradient calculation per blade element
    dCTdR(k) = (sigmaConst .* perSecClaMachCorrection(k) ./2)
                .* (perSecAlphaRad(k) .* nonDimR(k).^2 -
                lamda(k) .* nonDimR(k));

end % End of the for loop for calculating blade element data

% Coefficient of Thrust integration using the trapezoidal
% method
CT = trapz(nonDimR,dCTdR);

% Coefficient of Power Integration using the trapezoidal method
CP0 = (sigmaConst/2) * trapz(nonDimR, (perSecCdMachCorrection
      .* nonDimR.^3));
CPI = trapz(nonDimR, dCTdR .* lamda);
CP = CP0 + CPI;
CQ = CP; % By definition Coefficient of Torque is equal to
           Coefficient of Power
```

```
        % Figure of Merit Calculation:
        inducedPowerFactor = CPI / (CT^(3/2)/sqrt(2));
        CPIdeal = CT^(3/2)/sqrt(2);
        CPinducedKappa = inducedPowerFactor * CPIdeal;

        %Outputs:
        FM(i,j) = CPIdeal/(CPinducedKappa + CP0);
        FMCalc(i,j) = (CT^(3/2)/sqrt(2))/CP;
        Thrust(i,j) = CT*rho*diskArea*omega^2*rTip^2;
        Power(i,j) = CP*rho*diskArea*omega^3*rTip^3;
        Vi(i,j) = sqrt(Thrust(i,j)/(2 * rho * diskArea));
    end %End of the RPM sweep loop
end %End of the blade pitch sweep loop
```

Interpolation Function:

```
function [interpolatedClToUse,interpolatedClaToUse,interpolatedCdToUse]
= geometryPerformanceInterpolationOfBatchData(Cl,Cd, realAlpha,alphaFromData)


    dataLength = length(Cl);

    for j = 2: dataLength
        if(realAlpha <= alphaFromData(j))
            if (realAlpha >= alphaFromData(j-1))
                xRange = [alphaFromData(j-1) alphaFromData(j)]';
                yRangeCl = [Cl(j-1) Cl(j)];
                yRangeCd = [Cd(j-1) Cd(j)];
                interpolatedClToUse = interp1(xRange,yRangeCl,
                                      realAlpha, 'linear');
                interpolatedClaToUse = interpolatedClToUse ./
                                      realAlpha;
                interpolatedCdToUse = interp1(xRange,yRangeCd,
                                      realAlpha, 'linear');
            end
        end
    end

end
```

Calculation of Inflow Ratio Function:

```
function [lamda, PTLF, error]  = lam_calc(Cla, sigma, thetaZero, r, Nb)
    lamda = zeros(1,length(r));   %Preallocating  and initialising
                                  % the out vector
    lamdaLast = lamda;
    global PTLF
    i = 1;
    error = 1; %initialize the error value for the first case
```

```
    while (max(error) > 0.0005 & (i < 20))
        PTLF = F(lamda,r,Nb);
        lamda = (sigma .* Cla./(16 .* PTLF)) .* (sqrt(1 +
                (32.*PTLF./(sigma.*Cla)).* thetaZero .* r) - 1);
        error = abs((lamda - lamdaLast) ./ lamda);
        lamdaLast = lamda;

        i = i + 1; % increment the counter

        if i >= 20
            warning('Lamda did not meet convergence criteria');
        end
    end
end

function func = F(lamda, r, Nb)
    phi = lamda ./ r;
    fTip = (Nb./2) .* ((1-r) ./ (r .* phi));
    fRoot = (Nb./2) .* (r./ ( (1-r) .* phi));
    funcRoot = (2/pi).* acos(exp(-fRoot));
    funcTip = (2/pi).* acos(exp(-fTip));
    func = funcRoot .* funcTip;
end
```